

# **HIGH EFFICIENCY THERMOELECTRIC RADIOISOTOPE POWER SYSTEMS**

**Mohamed El-Genk<sup>1</sup>, Hamed Saber<sup>1</sup>, and Thierry Caillat<sup>2</sup>**

<sup>1</sup>Institute for Space and Nuclear Power Studies and Chemical and Nuclear Engineering Dept.,  
The University of New Mexico, Albuquerque, NM 87131, (505) 277 – 0446, [isnps@unm.edu](mailto:isnps@unm.edu)

<sup>2</sup>Jet Propulsion Laboratory, California Institute of Technology, 4800 Oak Grove Drive,  
Pasadena, CA 91109, (818) 35493 - 0407, [thierry.caillat@jpl.nasa.gov](mailto:thierry.caillat@jpl.nasa.gov)

## **Final Report**

**Report Number UNM-ISNPS-1-2004**

Support for the research provided by NASA Cross-Enterprise Development  
Program under Grant No. NAG3-2543 to the University of New Mexico's  
Institute for Space and Nuclear Power Studies, and Grant No. 80-5516 to the  
Jet Propulsion Laboratory

**July 2004**

*PROJECT DATES: 01/29/01 – 6/30/04*

# **HIGH EFFICIENCY THERMOELECTRIC RADIOISOTOPE POWER SYSTEMS**

**Mohamed El-Genk<sup>1</sup>, Hamed Saber<sup>1</sup>, and Thierry Caillat<sup>2</sup>**

<sup>1</sup>Institute for Space and Nuclear Power Studies and Chemical and Nuclear Engineering Dept.,  
The University of New Mexico, Albuquerque, NM 87131, (505) 277 – 0446, [isnps@unm.edu](mailto:isnps@unm.edu)

<sup>2</sup>Jet Propulsion Laboratory, California Institute of Technology, 4800 Oak Grove Drive,  
Pasadena, CA 91109, (818) 35493 - 0407, [thierry.caillat@jpl.nasa.gov](mailto:thierry.caillat@jpl.nasa.gov)

## **Final Report**

**Report Number UNM-ISNPS-1-2004**

Support for the research provided by NASA Cross-Enterprise Development  
Program under Grant No. NAG3-2543 to the University of New Mexico's  
Institute for Space and Nuclear Power Studies, and Grant No. 80-5516 to the  
Jet Propulsion Laboratory

**July 2004**



## Executive Summary

The work performed and whose results presented in this report is a joint effort between the University of New Mexico's Institute for Space and Nuclear Power Studies (ISNPS) and the Jet Propulsion Laboratory (JPL), California Institute of Technology. In addition to the development, design, and fabrication of skutterudites and skutterudites -based segmented uncouples this effort included conducting performance tests of these uncouples for hundreds of hours to verify theoretical predictions of the conversion efficiency. The performance predictions of these uncouples are obtained using 1-D and 3-D models developed for that purpose and for estimating the actual performance and side heat losses in the tests conducted at ISNPS. In addition to the performance tests, the development of the 1-D and 3-D models and the development of Advanced Radioisotope Power systems for Beginning-Of-Life (BOM) power of 108 W<sub>e</sub> are carried out at ISNPS. The materials synthesis and fabrication of the uncouples are carried out at JPL. The research conducted at ISNPS is documented in chapters 2-5 and that conducted at JP, in documented in chapter 5.

An important consideration in the design and optimization of segmented thermoelectric uncouples (STUs) is determining the relative lengths, cross-section areas, and the interfacial temperatures of the segments of the different materials in the n- and p-legs. These variables are determined using a genetic algorithm (GA) in conjunction with one-dimensional analytical model of STUs that is developed in chapter 2. Results indicated that when optimized for maximum conversion efficiency, the interfacial temperatures between various segments in a STU are close to those at the intersections of the Figure-Of-Merit (FOM),  $ZT$ , curves of the thermoelectric materials of the adjacent segments. When optimizing the STUs for maximum electrical power density, however, the interfacial temperatures are different from those at the intersections of the  $ZT$  curves, but close to those at the intersections the characteristic power,  $CP$ , curves of the thermoelectric materials of the adjacent segments ( $CP = T^2Zk$  and has a unit of W/m). Results also showed that the number of the segments in the n- and p-legs of the STUs optimized for maximum power density are generally fewer than when the same uncouples are optimized for maximum efficiency. These results are obtained using the 1-D optimization model of STUs that is detailed in chapter 2.

A three-dimensional model of STUs is developed and incorporated into the ANSYS commercial software (chapter 3). The governing equations are solved, subject to the prescribed

boundary conditions, using the Finite Element Methodology (FEM) techniques and meshing capabilities in ANSYS. The model accounts for the side heat losses, handles different types of boundary conditions, and accounts for the non-homogeneity and the change in physical and thermoelectric properties of the segments materials in the n- and p-legs with temperature. The model predictions are compared with experimental data of two STUs, uni8 and uni12, comprised of n-type  $\text{Bi}_2\text{Te}_{2.95}\text{Se}_{0.05}$  and  $\text{CoSb}_3$ -based alloys and p-type  $\text{Bi}_{0.4}\text{Sb}_{1.6}\text{Te}_3$  and  $\text{CeFe}_{3.5}\text{Co}_{0.5}\text{Sb}_{12}$ -based alloys, and tested at the Jet Propulsion Laboratory (JPL) at hot and cold junction temperatures of  $\sim 305$  K and 885 K, respectively. The calculations helped determine not only the side heat losses in these tests and the performance parameters of the STUs, but also the spatial dissipation of the heat losses from the various sides of and of the 3-D temperature fields in the n- and p-legs. The estimated values of the total side heat losses in uni8 and uni12 are  $3.7 W_{\text{th}}$  and  $1.83 W_{\text{th}}$ , respectively, and of the total contact resistance per leg are 146 and  $690 \mu\Omega\text{-cm}^2$ , respectively. The predicted peak conversion efficiencies in these tests for uni8 and uni12 are 4.55% and 5.65%, respectively, compared to 11.46% and 9.09% attainable with zero side heat losses, for the same total contact resistance per leg.

Conceptual designs of the Advanced Radioisotope Power System (ARPS) with Cascaded Thermoelectric Modules (CTMs) are developed and optimized for maximum efficiency operation for BOM electrical power of  $108 W_e$  (chapter 4). These ARPSs each employs four General Purpose Heat Source (GPHS) bricks generating  $1000 W_{\text{th}}$  at Beginning-Of-Life (BOL) and 32 CTMs. Each CTM consists of a top and a bottom array of thermoelectric unicouples, which are thermally, but not electrically, coupled. The top and bottom arrays of the CTMs are connected in series in two parallel strings with the same nominal voltage of  $> 28$  VDC. The ARPSs nominal efficiency of 10.82% - 10.85% is  $\sim 90\%$  higher than that of State-Of-the-Art (SOA) Radioisotope Thermoelectric Generators (RTGs).

The SiGe unicouples in the top arrays of the CTMs are optimized for a nominal hot junction temperature of 1273 K and a constant cold junction temperature of either 780 K or 980 K, depending on the thermoelectric materials of the unicouples in the bottom array. For a SiGe cold junction temperature of 780 K, the unicouples in the bottom array have p-legs of TAGS-85 and n-legs of 2N-PbTe and operate at constant hot junction temperature of 765 K and nominal cold junction temperature of 476.4 K. When the SiGe cold junction temperature is 980 K, the unicouples in the bottom arrays of CTMs have p-legs of  $\text{CeFe}_{3.5}\text{Co}_{0.5}\text{Sb}_{12}$  or  $\text{CeFe}_{3.5}\text{Co}_{0.5}\text{Sb}_{12}$

and  $\text{Zn}_4\text{Sb}_3$  segments, and n-legs of  $\text{CoSb}_3$  and operate at constant hot junction temperature of 965 K and nominal cold junction temperatures of 446.5 K or 493.5 K, respectively. The specific power of the ARPSs with CTMs vary from 8.2  $\text{W}_e/\text{kg}$  to 8.8  $\text{W}_e/\text{kg}$ , which is 71% to 83% higher, respectively, than that of SOA-RTGs, and with  $\sim 43\%$  less  $^{238}\text{PuO}_2$  fuel.

Three performance tests of skutterudites and skutterudites-based segmented thermoelectric unicouples are performed in the test facility at ISNPS for hundreds of hours at average hot and cold junction temperatures of  $\sim 973$  K and 300 K, respectively, to verify theoretical predictions (chapter 5). The first two tests (MAR-03 and JUN-03) involved non-segmented skutterudites unicouples of slightly different dimension, but of same materials for the n- ( $\text{CoSb}_3$ ) and p- ( $\text{CeFe}_{3.5}\text{Co}_{0.5}\text{Sb}_{12}$ ) legs. The test duration is 450 hours for MAR-03 and 1200 hours for JUN-03. The third test (JUL-03) is of a skutterudites-based segmented uncouple in which the p-leg has two segments of  $\text{CeFe}_{3.5}\text{Co}_{0.5}\text{Sb}_{12}$  and  $\text{Bi}_{0.4}\text{Sb}_{1.6}\text{Te}_3$  and the n-leg has two segments of  $\text{CoSb}_3$  and  $\text{Bi}_2\text{Te}_{2.95}\text{Se}_{0.05}$ . The segments in the n- and p-legs have different lengths and cross-sectional areas. The JUL-03 test duration is 645 hours.

All three unicouples for the performance tests are fabricated at JPL and instrumented, assembled, and tested in the vacuum facility at ISNPS in argon at  $\sim 0.051$  to  $0.068$  MPa to suppress the sublimation of antimony (Sb) from the legs near the hot shoe. Detailed measurements of the open circuit voltage, voltage across the n- and p-legs, the voltage-current (V-I) characteristics, and the hot and cold shoe temperatures are performed in all tests. In JUL-03, additional measurements of the interfacial temperatures and the voltage across the segments in the n- and p-legs are obtained as functions of test duration. Estimates Beginning-Of-Life (BOL) conversion efficiencies of 10.7% for Skutterudites and 13.5% for skutterudites-based segmented unicouples are within 10% of the theoretical predictions assuming zero side heat losses. Estimates of these losses in the tests are  $2.3 \text{ W}_{\text{th}}$  in MAR-03 to  $9.3 \text{ W}_{\text{th}}$  in JUL-03, thus the actual conversion efficiencies in the unicouples in the tests are  $\sim 40\text{-}50\%$  lower. Because the cross sectional areas of the legs of JUL-03 are much larger than of both MAR-03 and JUN-03, the measured BOL peak electrical power per uncouple is  $1.295 \text{ W}_e$  versus  $0.671 \text{ W}_e$  for the latter.

At JPL, a process was developed to fabricate skutterudites and skutterudites-based segmented legs with low electrical contact resistance at the legs interfaces. Limited in-gradient life testing has been conducted on coupons and the results showed promising

integrity. Antimony (Sb) sublimation has been identified as the main short-term potential degradation mechanism. A thin metallic film coating technique was developed and showed very encouraging results towards suppressing Sb sublimation, at least over the short term testing scope of this task. Life testing is currently being investigated under a Code S task to further study the potential of these unicouples for ARPS applications. A number of skutterudites and skutterudites-based segmented legs without Sb sublimation suppression coating were fabricated at JPL and delivered to UNM. At UNM these legs were assembled into unicouples, instrumented and placed on test in Argon (Ar) cover gas for hundreds of hours. The results of these performance tests are detailed in chapter 5.

## TABLE OF CONTENTS

Executive Summary.....	ii
List of figures.....	iv
List of Tables.....	viii
Nomenclature.....	ix
<b>1 Introduction .....</b>	<b>1</b>
<b>2 One Dimensional Analytical Optmization Model of Segmented Thermoelectrics</b>	
Unicouples (UNM-ISNPS) .....	3
2.1 Introduction .....	3
2.2 Model Development .....	6
2.2.1 Conversion Efficiency .....	8
2.2.2 Electric Power and Power Density .....	10
2.2.3 Genetic Algorithms for Performance Optimization of STU Performance .....	11
2.2.4 GA for Maximizing Conversion Efficiency and PD of STU .....	12
2.3 Comparison with the Model of Swanson et al. (1961) .....	12
2.4 Prediction Verification of the Present STU Model .....	15
2.5 Results and Discussions.....	17
2.5.1 STUs Performance.....	17
2.5.2 Effect of Contact Resistance.....	21
2.5.3 Interfacial Temperatures.....	21
2.6 Summary and Conclusions .....	28
<b>3 A Three-Dimensional, Performance Model of Segmented Thermoelectric</b>	
Unicouples (UNM-ISNPS) .....	29
3.1 Introduction .....	29
3.2 Model Description .....	31
3.2.1 Governing Equation.....	35
3.2.2 Element Vectors and Matrices.....	37
3.2.3 Heat Flux Boundary Condition.....	41
3.2.4 Convection/Radiation Boundary Condition .....	43
3.2.5 Global Vector and Matrices and Method of Solution.....	45
3.3 Incorporation of the STU Model in ANSYS Software.....	46
3.4 Verification of Model Predictions .....	47
3.5 Comparison with Test Data .....	47
3.6 Calculated Temperature Fields.....	53
3.7 Effect of Sublimation Suppression Coating on Temperature Field.....	54

3.8	Summary .....	62
4	Cascaded Thermoelectric Modules-Advanced Radioisotope Power Systems (CTM-ARPSs) (UNM-ISNPS) .....	64
4.1	Introduction .....	64
4.2	Cascaded Thermoelectric Converters .....	66
4.3	Thermoelectric Arrays .....	68
4.4	Electrical Connections of CTM Arrays .....	70
4.5	Performance Results .....	75
4.6	Nominal Electric Power and Efficiency .....	76
4.7	Specific Power and Power Density Comparisons .....	78
4.8	Mass and Specific Power Estimates for CTM-ARPSs .....	79
4.9	Summary .....	82
5	Performance Tests of Skutterudites-based Segmented and non-Segmented Thermoelectric Unicouples (UNM-ISNPS) .....	84
5.1	Introduction .....	84
5.2	Experiment Setup .....	88
5.3	Tests Histories .....	90
5.4	Results and Discussion .....	92
5.5	V-I Characteristics .....	93
5.6	Open Circuit Voltage .....	95
5.7	Analysis of Performance Data .....	97
5.8	Estimates of Contact and Thermoelectric Resistances .....	98
5.9	Estimates of BOL Side Heat Losses .....	100
5.10	Peak Conversion Efficiency and Load Electric Power .....	100
5.11	Summary .....	103
6	Unicouple Development (jpl) .....	106
6.1	Thermoelectric Materials .....	106
6.2	Segmented Legs Fabrication .....	107
6.3	Segmented Legs Characterization .....	109
6.4	Sublimation Characterization .....	112
6.5	Development of Coatings Materials Techniques Results .....	113
6.6	Summary .....	117
	References .....	118

## List of figures

Figure 2-1 Thermoelectric Figure-of-Merit (FOM) Versus Temperature for Various Materials.....	6
Figure 2-2 A Schematic and Notations of Various Segments of p-/n-Legs of a STU.....	7
Figure 2-3 Optimized STUs for Maximum Efficiency. ....	16
Figure 2-4 Optimized STUs for Maximum Power Density. ....	18
Figure 2-5 Calculated Conversion Efficiency for the STUs.....	20
Figure 2-6 Predicted Performance Characteristics for the STUs.....	22
Figure 2-7 Calculated Interface Temperatures for the STUs.....	23
Figure 2-8 Calculated Interface Temperatures and $\eta_{max}$ . ....	24
Figure 2-9 Characteristic Power of Different TE Materials. ....	25
Figure 2-10 Calculated Interface Temperatures and $PD_{max}$ .....	27
Figure 3-1 Flow Diagram of Evaluating Side Heat Losses from STUs in Performance Tests. ....	32
Figure 3-2 A Schematic of a STU.....	33
Figure 3-3 A Schematic of Three-Dimensional Tetrahedral Element. ....	36
Figure 3-4 A Flow Diagram for Incorporating the 3-D Model of STU into ANSYS.....	48
Figure 3-5 A Schematic of the uni8 and uni12 Compositions and Dimensions. ....	49
Figure 3-6 Comparisons of Predictions of 3-D and 1-D Models, Assuming Zero Side Heat Losses for uni12. ....	50
Figure 3-7 Comparisons of 3-D and 1-D Models with Test Data for uni8. ....	51
Figure 3-8 Comparisons of 3-D STU Model and 1-D Models with Test Data for uni12. ....	52
Figure 3-9 Calculated Temperature Field in a Slice in the n- and p-Legs of uin8 at $x=12.12$ mm. ....	54
Figure 3-10 Calculated Temperature Field and Side Heat Losses in a Slice Parallel to y-z Plane in $P_2$ and $N_1$ Segments at $x=12.12$ mm in uni8.....	55
Figure 3-11 Temperature Field at a Slice in n-leg of uni8 at $x = 0.2$ mm.....	56
Figure 3-12 Temperature Field at a Slice in n-leg of uni8 at $x = 2.5$ mm (Middle of Ti Coating).....	57

Figure 3-13 Temperature Field at a Slice in n-Leg of uni8 at x = 5.0 mm (End of Ti Coating).....	58
Figure 3-14 Temperature Field at a Slice in n-Leg of uni8 at x = 5.5 mm (0.5 mm Below Ti Coating).....	59
Figure 3-15 Temperature Field at a Slice in n-Leg of uni8 at x = 13.663 mm (Middle of N <sub>2</sub> ). ....	60
Figure 4-1 Arrangement of CTMs Around GPHS Brick in ARPSs.....	67
Figure 4-2 Schematics of the Cascaded Thermoelectric (CTE) Unicouples for ARPSs.....	68
Figure 4-3 Arrangements of Unicouples in Top and Bottom Arrays of CTM with the CTE Configuration in Figure 4-2a.....	71
Figure 4-4 Circuit Diagram for Connecting the 32 CTMs in the Present CTM-ARPSs. .	72
Figure 4-5 Building Blocks of CTMs in the Present CTM-ARPSs.....	73
Figure 4-6 Performance Results of the Present CTM-ARPSs.....	74
Figure 4-7 Comparisons of Power Density and Specific Power of Thermoelectric Materials.....	77
Figure 4-8 Pictorial Views of the Present CTM-ARPSs and a SOA-RTG.....	80
Figure 5-1 FOM for Different TE Materials. ....	85
Figure 5-2 STE Converter for T <sub>c</sub> = 300 K.....	86
Figure 5-3 Segmented and Non-segmented Skutterudites-Based Unicouples in Performance Tests Performed at the University of New Mexico. ....	87
Figure 5-4 Schematics of MAR-03 and JUL-03 Unicouples Tested at the UNM-ISNPS Facility. ....	89
Figure 5-5 Detailed of the Assembled Unicouples in the Tests Performed in the UNM-ISNPS Test Facility. ....	90
Figure 5-6 Testing Histories for MAR-03 and JUL-03 Unicouples.....	91
Figure 5-7 Measured V-I Characteristics for Skutterudites (MAR-03) and STE (JUL-03) Unicouples. ....	94
Figure 5-8 Measured Changes in Open Circuit Voltages for MAR-03 and JUN-03 Skutterudites and JUL-03 STE Unicouples. ....	96
Figure 5-9 MAR-03 Measured and Calculated Performance.....	101
Figure 5-10 JUL-03 Measured and Calculated Performance. ....	102



Figure 6-1 Illustration of Segmented Unicouple Utilizing $\text{Bi}_2\text{Te}_3$ -based Segments at the Low Temperature Ends and Skutterudite Materials for the Upper Temperature Segments.....	106
Figure 6-2 ZT Values as a Function of Temperature for Unicouple Thermoelectric Materials.....	107
Figure 6-3 N- and p-type Segmented Legs After Hot-Pressing. ....	108
Figure 6-4 Photograph on n-type Skutterudite Leg (with Metal Contact on Both Ends) in the Electrical Contact Resistance Test Jig. ....	109
Figure 6-5 Results of In-gradient Contact Resistance Measurement for a $\text{Ti}/\text{CoSb}_3/\text{Ti}/\text{n-Bi}_2\text{Te}_{2.95}\text{Se}_{0.05}$ Segmented Leg. The Electrical Contact Resistance at the Various Interfaces is Below $5\ \mu\Omega\cdot\text{cm}^2$ . ....	110
Figure 6-6 Results of In-gradient Contact Resistance Measurement for a $\text{Ti}/\text{Pd}/\text{Ce}_{0.85}\text{Fe}_{3.5}\text{Co}_{0.5}\text{Sb}_{12}/\text{Pd}/\text{Ti}/\text{Bi}_{0.4}\text{Sb}_{1.6}\text{Te}_3$ Segmented leg. The Electrical Contact Resistance at the Various Interfaces is Below $5\ \mu\Omega\cdot\text{cm}^2$ and Shows Negligible Changes with time ( 116 Hours of Testing).....	111
Figure 6-7 Results of In-gradient Contact Resistance Measurement for a $\text{Ti}/\text{CoSb}_3/\text{Ti}$ Skutterudite Leg. The Electrical Contact Resistance at the Various Interfaces is Below $5\ \mu\Omega\cdot\text{cm}^2$ . The Sample Was Tested for a Maximum of 2760 Hours. ....	111
Figure 6-8 Results of In-gradient Open Circuit Voltage Measurements for n- and p-Legs. (p: DGF182 ; n: DGC99). The Experimental Results Are Compared to Theoretical Predictions Based on the Measured Seebeck Coefficient Values of the Materials. The Agreement Between Theoretical and Experimental Data is within 5%. ....	112
Figure 6-9 SEM Photograph of Section of an n-Leg After 3 Months of Testing at 975K. The “Necking” as a Result of Sb Sublimation Is Seen. Bond Integrity However Seems to be Preserved.....	113
Figure 6-10 Photograph of n-Leg with Upper Section Encapsulated with 10 $\mu\text{m}$ Thick Ti Foil. ....	114
Figure 6-11 Mass Loss as a Function of Time for n- and p- Ti-Coated and Uncoated Samples Annealed at 975K.....	114

Figure 6-12 Cross-Sectional Views of Ti-Coated n-Leg in the Coated Region That Was Exposed to High Temperatures. The Images Clearly Reveal the Sb Suppression in the Coated Region While the Sublimation Layers Are Seen Past the Coated Section. ....	115
Figure 6-13 Mass Loss as a Function of Temperature for Uncoated n-Type Skutterudite Samples. ....	116
Figure 6-14 Mass Loss as a Function of Temperature for 25 $\mu\text{m}$ Mo Coated n-Type Skutterudite Sample. ....	116

## List of Tables

Table 2-1 Comparison of the Present Model and That of Swanson et al. (1961) .....	13
Table 2-2 Predictions Comparison of the Present Model and That of Swanson et al. (1961).....	14
Table 2-3 Comparison of Present Model with Experimental Data of SiGe Unicouples*.	15
Table 4-1 Dimensions and Operation Parameters for CTEs and CTMsfor the ARPSs.	69
Table 4-2 Mass and Performance Comparisons of CTM-ARPSs with SOA-RTG. ....	75
Table 5-1 Estimates of BOL Performance Parameters for MAR-03 Sutterudites JUL-03 STE Unicouples Tested.....	100

## Nomenclature

$a_{1-4}$	coefficients ( $\text{m}^3$ )
$A$	cross-section area ( $\text{m}^2$ )
$b_{1-4}$	coefficients ( $\text{m}^2$ )
$[C]$	damping or mass matrix ( $\text{J K}^{-1}$ )
$C_1$	coefficient (K)
$c_{1-4}$	coefficients ( $\text{m}^2$ )
$C_{2,3,4}$	coefficients ( $\text{K m}^{-1}$ )
$C_p$	specific heat ( $\text{J kg}^{-1} \text{K}^{-1}$ )
$d_{1-4}$	coefficients ( $\text{m}^2$ )
$E$	open circuit voltage (V)
$f$	dimensionless factor
$\{F\}$	forcing vector (W)
$\{FJ\}$	contribution to forcing vector due to Joule heating (W)
$\{FL\}$	contribution to forcing vector due to heat losses (W)
$\{FQ\}$	contribution to forcing vector due to heat flux boundary condition (W)
$h$	heat transfer coefficient ( $\text{W m}^{-2} \text{K}^{-1}$ )
$I$	electrical current (A)
$J$	electrical current density ( $\text{A m}^{-2}$ )
$k$	thermal conductivity ( $\text{W m}^{-1} \text{K}^{-1}$ )
$[K]$	conductivity matrix ( $\text{W K}^{-1}$ )
$[KF]$	contribution to conductivity matrix due Fourier effect ( $\text{W K}^{-1}$ )
$[KL]$	contribution to conductivity matrix due heat losses ( $\text{W K}^{-1}$ )
$[KT]$	contribution to conductivity matrix due Thomson heating ( $\text{W K}^{-1}$ )
$\lambda$	segment length (m)
$L$	total length of the STU
$m'$	ratio of load to internal resistances
$n$	directional cosine

$N$	number of segments in p-leg
$N_E$	total number of tetrahedral elements in the meshed STU
$N_x, N_y, N_z$	coefficients ( $\text{m}^2$ )
$M$	number of segments in n-leg
$P_e$	electrical power (W)
$PD$	electrical power density ( $\text{W m}^{-2}$ )
$q$	heat flux ( $\text{W m}^{-2}$ )
$Q$	Thermal power (W)
$q'''$	volumetric heat generation ( $\text{W m}^{-3}$ )
$r$	contact resistance per interface ( $\Omega\text{-m}^2$ )
$R$	electrical resistance ( $\Omega$ )
$R'$	electrical resistance ( $\bar{\rho} \lambda$ ) ( $\Omega\text{-m}^2$ )
$t$	time (s)
$T$	temperature (K)
$\{T\}$	temperature vector (K)
$\{\dot{T}\}$	vector of derivative of temperature with respect to time ( $\text{K s}^{-1}$ )
$V$	voltage (V)
$V^e$	volume of tetrahedral element ( $\text{m}^3$ )
$x$	coordinate measured from heat source - $P_1$ and heat source- $N_1$ segments interfaces (m)
$y$	coordinate in lateral direction (m)
$z$	coordinate normal to lateral direction (m)
$Z$	Figure-of-Merit (FOM) ( $\text{K}^{-1}$ )
$ZT$	dimensionless Figure-of-Merit

### ***Greek Symbols***

$\alpha$	Seebeck coefficient ( $\text{V K}^{-1}$ )
$\alpha'$	effective Seebeck coefficient of STU ( $\text{V K}^{-1}$ )
$\eta$	conversion efficiency (%)
$\eta_{\text{Carnot}}$	Carnot efficiency ( $1 - T_c / T_h$ )
$\Theta$	dimensionless temperature

$\rho$	electrical receptivity ( $\Omega \text{ m}$ )
$\pi$	Peltier coefficient (V)
$\Psi$	dimensionless factor
$\Psi_{1-4}$	dimensionless nodal basis function of tetrahedral element
$\beta_n, \beta_p$	coefficients ( $\text{V K}^{-1}$ )
$\beta'_n, \beta'_p$	coefficients ( $\text{V K}^{-1}$ )
$\gamma_{i1-i3}$	coefficients ( $\text{m}^3$ )
$\Gamma$	portion form STU surface
$v$	test function
$\omega$	density ( $\text{kg m}^{-3}$ )
$\tau$	Thomson coefficient ( $\text{V K}^{-1}$ )
$\Omega^e$	domain of tetrahedral element

### ***Superscripts***

-	average
$\sim$	corresponding to maximum electrical power
e	element
G	global
s	interface number between segments
.	derivative with respect to time
$\wedge$	specified

### ***Subscripts***

c	cold side
cont	contact
conv	convective
e	electric
eff	effective
h	hot side
i	index refers to p- and n- legs
in	supplied to the hot junction from heat source
int	internal

j	index refer to segment number in p- and n- legs
J	Joule
L	electrical load
Loss	losses
max	maximum
n	n-leg, normal to the surface
opt	optimum
p	p-leg
rad	radiation
x	x-direction
y	y-direction
z	z-direction
rej	rejected to the heat sink from the cold junction
th	thermal
$\tau$	Thomson

### ***Abbreviations***

ARPS	Advanced Radioisotope Power System
BOL	Beginning-Of-Life
BOM	Beginning-Of-Mission
CTC	Cascaded Thermoelectric Conversion
CTE	Cascaded Thermoelectric
CTM	Cascaded Thermoelectric Module
EOM	End-Of-Mission
FPSE	Free-Piston Stirling Engine
FOM	Figure-Of-Merit
GA	Genetic Algorithms
GPHS	General Purpose Heat Source
ISNPS	Institute for Space and Nuclear Power Studies
JPL	Jet Population Laboratory
PD	Power Density
RTG	Radioisotope Thermoelectric Generator

SOA	State-of-the Art
SPS	Space Power System
SSC	Sublimation Suppression Coating
STE	Segmented Thermoelectric
ST-RPS	Segmented Thermoelectric Radioisotope Power System
STU	Segmented Thermoelectric Unicouple



# 1 INTRODUCTION

This final report is comprised of five technical sections, in addition to the introduction, which provide details on the work accomplished by the University of New Mexico's Institute for Space and Nuclear Power Studies (ISNPS) and the Jet Propulsion Laboratory (JPL) on the development, design, fabrication, and performance testing of novel, skutterudites and skutterudites-based segmented thermoelectric uncouples for potential use in Advanced Radioisotope Power Systems (ARPSs) in NASA's future missions. This work is funded under NASA Grant No. NAG3-2543 to ISNPS and NASA Grant No. 80-5516 to JPL. The opinions expressed in this article are solely those of the authors and have neither been endorsed by nor reflect an official position of NASA.

Detailed performance optimization is conducted and mass estimates are obtained of ARPSs with Cascaded Thermoelectric Modules (CTMs) for Beginning-Of-Mission electrical power of 108 W<sub>e</sub>. The CTMs consist of a top array of SiGe unicouples and a bottom array of either skutterudites, skutterudites-based segmented, or 2N-PbTe / TAGS85 unicouples. Results showed that the former two are quite superior and with them these ARPSs could operate with a net efficiency in excess of 11%, reducing the amount of <sup>238</sup>PuO<sub>2</sub> fuel by ~ 42%; more details on these ARPS are provided in chapter 4.

Chapter 5 presents the performance test results of a number of skutterudites and skutterudites-based segmented unicouples that are performed under Argon gas pressure to suppress the sublimation of the volatile antimony from the n- and p-legs near the hot shoe. These tests are performed in the test facility at the University of New Mexico's Institute for Space and Nuclear Power Studies for hundreds of hours. The test unicouples are fabricated at JPL and assembled and instrumented for the performance tests at ISNPS. These tests are performed at average hot and cold junction temperatures of ~ 973 and 300 K, respectively. The results of the performance tests detailed in chapter 4 are used to confirm theoretical predictions for the conversion efficiency of skutterudites and skutterudites-based segmented unicouples obtained using both 1-D and 3-D models.

These models are developed and benchmarked at ISNPS. The 1-D model assumes zero side heat losses, which are difficult to attain in the laboratory tests, but is likely in ARPSs in which the unicouples are well insulated. This model is coupled to Genetic Algorithm to optimize the

lengths and the cross-sectional areas of the segments of the different thermoelectric materials in the n- and p-legs of the segmented uncouples for either maximum efficiency or maximum electric power density. When used with the measured contacted resistances in the tests, the 3-D model calculates the side heat losses and the actual conversion efficiency in the tests. Model predictions of the performance parameters of the uncouples tested at ISNPS and detailed in chapter 4, confirmed that a peak conversion efficiency of  $\sim 13.8\%$  for skutterudites-based segmented uncouples is possible. Details on the development of these models and their performance predictions are presented in chapters 2 and 3.

Chapter 6 presents the details on the progress made on the materials synthesis and fabrication of the skutterudites and skutterudites -based thermoelectric uncouples at the Jet Propulsion Laboratory (JPL).

## 2 ONE DIMENSIONAL ANALYTICAL OPTMIZATION MODEL OF SEGMENTED THERMOELECTRICS UNICOUPLES (UNM-ISNPS)

An important consideration in the design and optimization of segmented thermoelectric unicouples (STUs) is determining the relative lengths and the cross-section areas, and the interfacial temperatures of the segments of the different materials in the n- and p-legs. These variables are determined using a Genetic Algorithm (GA) in conjunction with a one-dimensional analytical model of STE converters developed in this chapter. Results indicated that when maximizing the efficiency, the interfacial temperatures between various segments are close to those at the intersections of the  $ZT$  curves of the thermoelectric materials of the adjacent segments. When maximizing the electrical power density, however, the interfacial temperatures are different from those at the intersections of the  $ZT$  curves, but close to the temperatures at the intersections the characteristic power,  $CP$ , curves developed in this chapter for various thermoelectric materials of the segments ( $CP = T^2 Zk$  and has a unit of W/m). Results also show that the number of the segments in the n- and p-legs of the converters optimized for maximum power density are generally fewer than when the same converters are optimized for maximum efficiency.

### 2.1 Introduction

Thermoelectric devices for static energy conversion of thermal power to electricity are being considered in many applications. In the last four decades, PbTe / TAGS-85 and SiGe unicouples have been used on board of more than 44 spacecrafts, mostly for planetary exploration missions, with the thermal power supplied by radioisotope heat sources. These Radioisotope Thermoelectric Generators (RTGs) provided 2.7 to 290  $W_e$  and performed markedly well in 5 - 10 year space missions, or even longer, in which the radioactive decay thermal power of the source decreases by less than 10%. SiGe thermoelectric unicouples had also been used in the Systems for Auxiliary Nuclear Power (SANP)-10A to convert the heat generated by fission in a liquid NaK cooled, thermal spectrum nuclear reactor to electricity at hot and cold junction temperatures of 712 K and 579 K, respectively (Angelo and Buden 1985). In the SP-100 Space Reactor Power System (SRPS) designed to generate 15 to 1000  $kW_e$  for 7-10 year space missions (Marriort and Fujita 1994) SiGe power conversion assemblies have also been

considered for operating at hot and cold junction temperatures of 1270 K and 790 K, respectively. For hot junction temperatures of 573-873 K thermoelectric energy conversion devices are being used or considered for waste heat recovery in light and heavy-duty trucks and fuel-efficient vehicles to satisfy the federal standards for lower emission (Hendricks and Lustbader 2002). Milliwatts radioisotope thermoelectric sensors with BiTe converters are being used in bio-medical applications such as pacemakers, for nerve and muscle stimulation, and in environmental monitoring equipment for terrestrial applications and planetary exploration. Thermoelectric coolers are widely used in industrial and medical applications, such as the cooling of CPU chips and microprocessors, environmental sensors, laser diodes, infrared detectors, electronic devices, and computer chips manufacturing, and in recreational refrigerators.

For thermoelectric devices, which are inherently redundant with many years of reliable operation, the conversion efficiency is proportional to the temperature difference between the hot and cold junctions and the Figure-Of-Merit (FOM) of the thermoelectric materials of n- and p-legs (Figure 2-1). Thus, for given junction temperatures, the higher is the FOM the higher the conversion efficiency. Unfortunately, no single thermoelectric material could be used for a wide range of cold and hot junction temperatures to operate at a high efficiency because each material possesses high FOM within a certain temperature range (Figure 2-1). However, when segments of compatible materials are used in the n- and p- legs, such that each segment operates in the most promising temperature range for the material of the segment, high segmented thermoelectric converter efficiency could be realized (El-Genk and Saber 2003, El-Genk et al. 2002 and Caillat et al. 1997). The number and the selection of the materials of the various segments in the n- and p-legs depend on the values of the hot and cold junction temperatures; the number of segments in each leg generally increases as the hot and cold junction temperatures increase and decrease, respectively.

The materials of the segments should be chemically compatible with minimal interfacial electrical and thermal resistances and an effective barrier to limit or eliminate mass diffusion across the interfaces. The TE materials of the segments in the n- and p-legs should preferably have similar Coefficients of Thermal Expansion (CTE) to minimize stresses during operation and ensure long operation life. Potential candidate materials for use in STUs can easily be identified in Figure 2-1, except SiGe that is incompatible with the skutterudites  $\text{CeFe}_{3.5}\text{Co}_{0.5}\text{Sb}_{12}$  and  $\text{CoSb}_3$

(Caillat et al. 1999 and Caillat et al. 2000). Because of such incompatibility, SiGe could only be used in an upper stage that is cascaded with 2N-PbTe/TAGS-85, skutterudites, or skutterudites-based segmented thermoelectric bottom stage to attain high conversion efficiency, while operating at a hot junction temperature of 1273 K, cold junction temperature as low as 350 – 450 K and a conversion efficiency that as high as 12% (El-Genk 2002 and El-Genk and Saber 2004). In these Cascaded Thermoelectric devices, the upper and the lower stage are thermally, but not electrically, coupled and the hot junction temperature of the bottom stage depends on the properties and vapor pressure of the TE material used. For example, with a skutterudites TE bottom stage the hot junction temperature is limited to 973 K and for PbTe / TAGS-85 it should not exceed 700 K for long service life.

In this chapter, a 1-D, thermoelectric analytical model has been developed for optimizing the performance of the STUs in conjunction with Genetic Algorithm (GA). The TE model assumes zero side heat losses, but accounts for the change of the material properties with temperature. The STU in the present model can have up to five segments in each leg (see Figure 2-2). In order to obtain a closed form analytical solution of the energy equations for the various segments, the strongly temperature-dependent thermoelectric properties are linearized using a volume averaging approach. The model also calculates the lengths of the various segments in the n- and p-legs and the values of the temperatures at segments interfaces for either maximum power density or maximum efficiency operation. The latter is possible through the application of GA in conjunction with the present STU, 1-D model.

Given the total length of the STU legs, cross-section area of p-leg, values of the hot and cold junction temperatures, the model, together with GA, calculates interfacial temperatures between various segments in the n- and p-legs, the lengths of the segments, the cross-section area of n-leg, and  $m'_{opt}$  (the ratio of the load resistance and the total internal resistance at peak efficiency). The calculations of the voltage-current characteristics, conversion efficiency, electrical power output, and the input and rejected thermal powers as functions of the electrical current of the external load demand, are carried out for either maximizing the conversion efficiency or the electrical power density of the STU.

Specifying either the interfacial temperatures or the lengths of the various segments in the input to the model, however, implies that number of the segments in the n- and p-legs are the same when optimizing the STU's performance for maximum efficiency or maximum electrical

power density. The validity of such an assumption is examined in this chapter using a genetic algorithm (GA), used in conjunction with 1-D model of the STUs, to search for the correct values of the interfacial temperatures as well as the lengths of the various segments of thermoelectric materials in the n- and p-legs, for optimizing the performance for maximum conversion efficiency and for maximum electrical power density. Thus, for a given total length,  $L$ , cross-section area of p-leg,  $A_p$ , and hot junction temperature,  $T_h$ , and cold junction temperature,  $T_c$ , the cross-section of the n-leg,  $A_n$ , the ratio of load resistance to the total internal resistance of STU,  $m'$ , and the interfacial temperatures,  $T_i^{(s)}$ , the number and lengths of various segments in the n- and p-legs,  $\lambda_{i,j}$  (Figure 2-2) are optimized for either maximum conversion efficiency or maximum electrical power density.

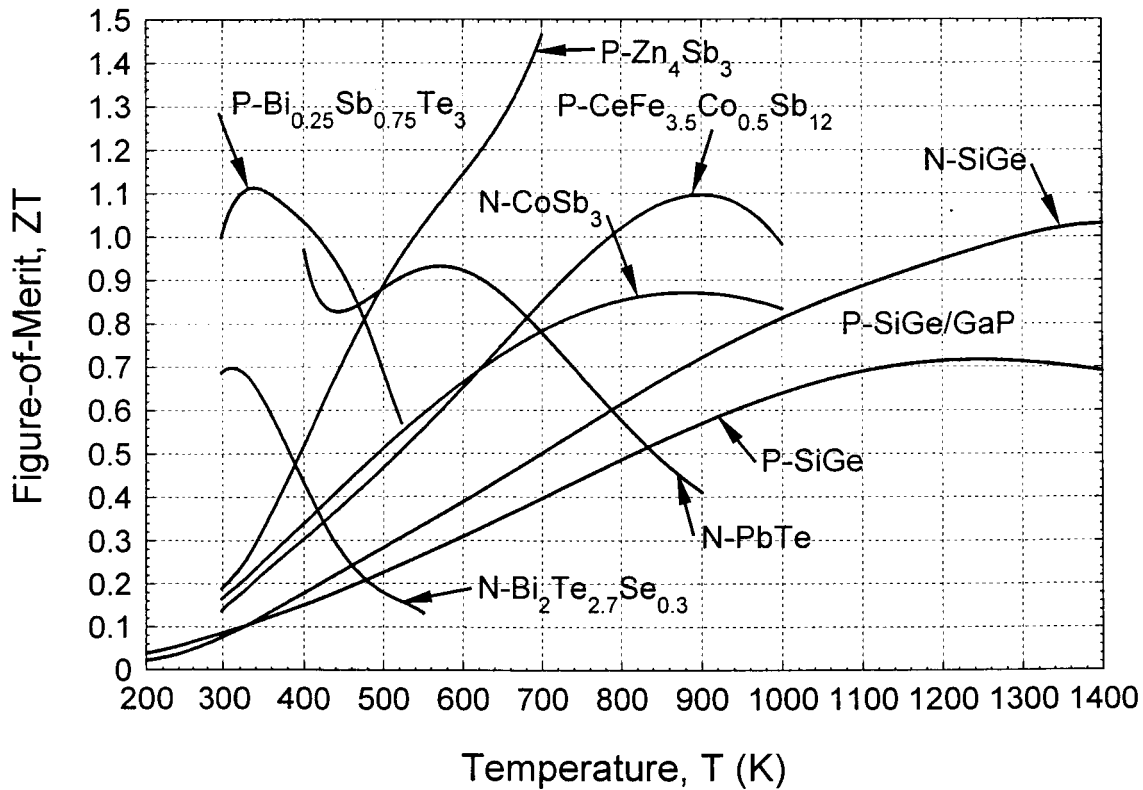


Figure 2-1 Thermoelectric Figure-of-Merit (FOM) Versus Temperature for Various Materials.

## 2.2 Model Development

Figure 2-2 presents a schematic and notations of the various segments in the p/n-legs of a STU. The n- and p-legs, extending from  $x = 0$  to  $x = L$ , are heated and cooled at constant

junction temperatures,  $T_h$  and  $T_c$ , respectively. The present model assumes that the legs are perfectly insulated on the sides and have constant, but different cross-sectional areas. The thermal conductivity, electrical resistivity, and the Seebeck and Thomson coefficients of the thermoelectric materials in the various segments of the STU are assumed homogenous, but different and temperature dependent.

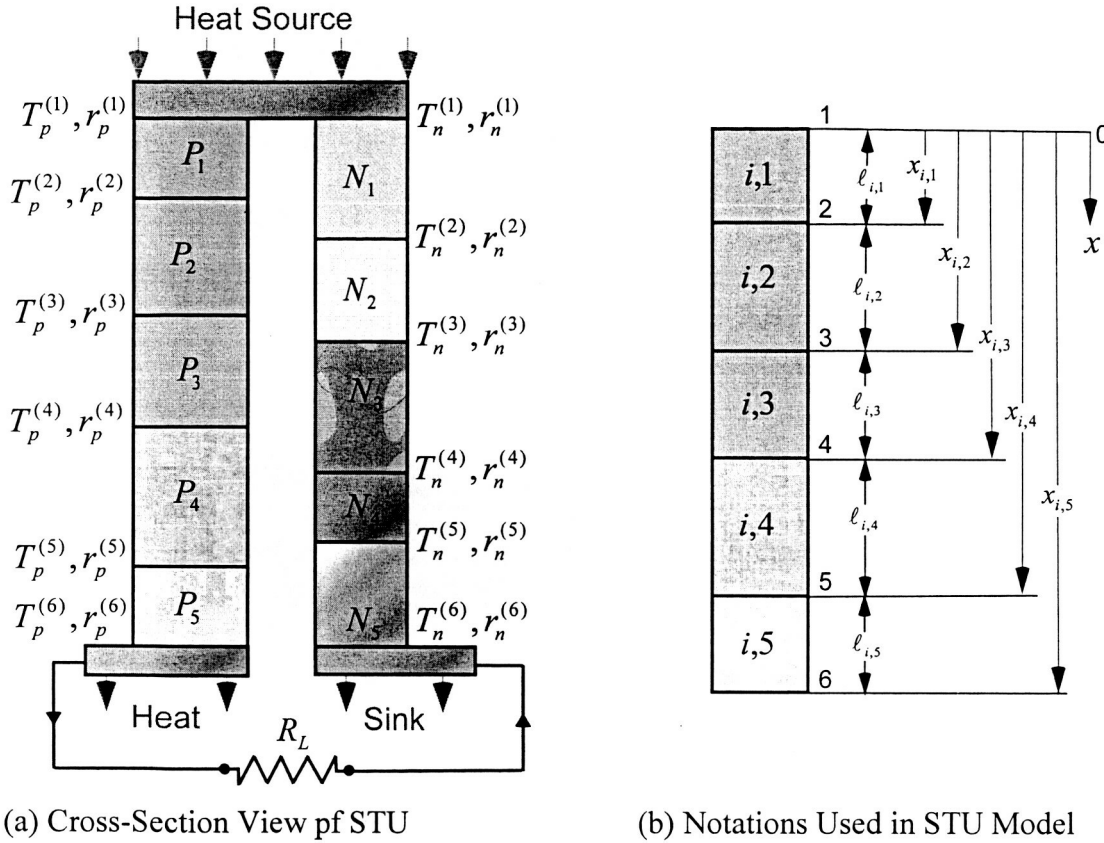


Figure 2-2 A Schematic and Notations of Various Segments of p-/n-Legs of a STU.

The steady-state heat conduction equation in the “ $i, j$ ” segment of the STU is:

$$\bar{k}_{i,j} \left( d^2 T_{i,j} / dx^2 \right) + q_{\tau_{i,j}}''' + q_{J_{i,j}}''' = 0. \quad (2-1)$$

In this equation, and in Figure 2-2, the subscript  $i$  indicates the type of the leg ( $i = n$  and  $p$  for the n- and p-legs, respectively) and the subscript  $j$  in Eq. (2-1) indicates the order of the segments ( $j = 1, 2, \dots, N$ , in the p-leg and  $j = 1, 2, \dots, M$  in the n-leg), starting at the hot junction ( $x = 0$ ). For the segment “ $i, j$ ”, the following relations define how the average thermal conductivity and the Joule,  $q_{J_{i,j}}$ , and volumetric Thomson,  $q_{\tau_{i,j}}$ , heating terms in Eq. (2-1) are evaluated:

$$\bar{k}_{i,j} = (1/\lambda_{i,j}) \int_{\lambda_{i,j}} k_{i,j}(T_{i,j}(x)) dx. \quad (2-2a)$$

$$q''_{\tau,i,j} = - \left( J_i / \lambda_{i,j} \right) \int_{\lambda_{i,j}} T_{i,j}(x) (d\alpha_{i,j} / dT_{i,j}) (dT_{i,j} / dx) dx, \text{ and} \quad (2-2b)$$

$$q''_{J,i,j} = \left( J_i^2 / \lambda_{i,j} \right) \int_{\lambda_{i,j}} \rho_{i,j}(T_{i,j}(x)) dx. \quad (2-2c)$$

Equation (2-1) is solved analytically subject to the following boundary conditions:

$$T_{i,j}(x = x_{i,j-1}) = T_i^{(j)}, \quad T_{i,j}(x = x_{i,j}) = T_i^{(j+1)}, \quad (2-3a)$$

$$q_{i,j}^{(j)}(x = x_{i,j-1}) = q_{i,j-1}^{(j)}(x = x_{i,j-1}) + J_i^2 r_i^{(j)} + J_i (\pi_{i,j-1}(T_i^{(j)}) - \pi_{i,j}(T_i^{(j)})), \text{ and} \quad (2-3b)$$

$$q_{i,j+1}^{(j+1)}(x = x_{i,j}) = q_{i,j}^{(j+1)}(x = x_{i,j}) + J_i^2 r_i^{(j+1)} + J_i (\pi_{i,j}(T_i^{(j+1)}) - \pi_{i,j+1}(T_i^{(j+1)})). \quad (2-3c)$$

According to Eq. (2-3a),

$$T_{i,1}(x = 0) = T_i^{(1)} = T_h \text{ at heat source } (x = 0) \text{ and}, \quad (2-4a)$$

$$T_{p,N}(x = L) = T_p^{(N+1)} = T_c, \text{ and } T_{n,M}(x = L) = T_n^{(M+1)} = T_c \text{ at heat sink } (x = L). \quad (2-4b)$$

The obtained axial temperature and heat flux distributions in the segment “ $i, j$ ” where  $x_{i,j-1} \leq x \leq x_{i,j}$ , are given, respectively, as follows:

$$T_{i,j}(x) = T_i^{(j)} - (T_i^{(j)} - T_i^{(j+1)}) \left( \frac{(x - x_{i,j-1})}{\lambda_{i,j}} \right) + \frac{(q''_{\tau,i,j} + q''_{J,i,j}) \lambda_{i,j}^2}{2 \bar{k}_{i,j}} \left[ \left( \frac{x - x_{i,j-1}}{\lambda_{i,j}} \right) - \left( \frac{x - x_{i,j-1}}{\lambda_{i,j}} \right)^2 \right], \quad (2-5)$$

and

$$q_{i,j}(x) = \bar{k}_{i,j} (T_i^{(j)} - T_i^{(j+1)}) / \lambda_{i,j} + (q''_{\tau,i,j} + q''_{J,i,j}) ((x - x_{i,j-1}) - 0.5 \lambda_{i,j}). \quad (2-6)$$

In the following sections, the expressions used to calculate the conversion efficiency and the electric power output as well as the I-V characteristics of the STU are presented and discussed.

### 2.2.1 Conversion Efficiency

The conversion efficiency,  $\eta$ , of the STU is defined as the ratio of the electrical power generated,  $P_e$ , to the thermal power supplied at the hot junction ( $x = 0$ ) of the STU from the heat source,  $Q_{in}$  as:



$$\eta = (P_e / Q_{in}) = ((\alpha' (T_h - T_c))^2 / (R_L ((R_{int} / R_L) + 1)^2)) / Q_{in} \quad (2-7a)$$

The open circuit voltage is given as:

$$E = \alpha' (T_h - T_c). \quad (2-7b)$$

The coefficients in Eqs. (2-7a) and (2-7b) are given as:

$$\alpha' = \left( \sum_{j=1}^N \bar{\alpha}_{p,j} \Delta T_{p,j} + \sum_{j=1}^M |\bar{\alpha}_{n,j}| \Delta T_{n,j} \right) / (T_h - T_c), \quad (2-8a)$$

$$\bar{\alpha}_{i,j} = \frac{1}{\lambda_{i,j}} \int_{\lambda_{i,j}} \alpha_{i,j}(T_i(x)) dx, \quad \Delta T_{i,j} = (T_i^{(j)} - T_i^{(j+1)}), \quad (2-8b)$$

$$R_{int} = \frac{1}{A_p} \sum_{j=1}^N \bar{\rho}_{p,j} \lambda_{p,j} + \frac{1}{A_n} \sum_{j=1}^M \bar{\rho}_{n,j} \lambda_{n,j} + R_{cont}, \quad \bar{\rho}_{i,j} = \frac{1}{\lambda_{i,j}} \int_{\lambda_{i,j}} \rho_{i,j}(T_{i,j}(x)) dx, \text{ and} \quad (2-8c)$$

$$R_{cont} = \sum_{j=1}^{N+1} \frac{r_p^{(j)}}{A_p} + \sum_{j=1}^{M+1} \frac{r_n^{(j)}}{A_n}. \quad (2-8d)$$

The input thermal power removed from the heat source at the hot junction of the STU ( $x = 0$ ),  $Q_{in}$ , is:

$$Q_{in} = (A_p \bar{k}_{p,1} / \lambda_{p,1}) (T_h - T_p^{(2)}) + (A_n \bar{k}_{n,1} / \lambda_{n,1}) (T_h - T_n^{(2)}) - 0.5 I^2 (\bar{\rho}_{p,1} \lambda_{p,1} / A_p) \\ - 0.5 I^2 (\bar{\rho}_{n,1} \lambda_{n,1} / A_n) - 0.5 I T_h \beta_p - 0.5 I T_h \beta_n + I T_h \alpha_{pn}(T_h), \quad (2-9a)$$

where,

$$\beta_p = (T_p^{(2)} / T_h) (\bar{\alpha}_{p,1} - \alpha_{p,1}(T_p^{(2)})) + (\alpha_{p,1}(T_h) - \bar{\alpha}_{p,1}), \text{ and} \quad (2-9b)$$

$$\beta_n = (T_n^{(2)} / T_h) (\alpha_{n,1}(T_n^{(2)}) - \bar{\alpha}_{n,1}) + (\bar{\alpha}_{n,1} - \alpha_{n,1}(T_h)).$$

The rejected thermal power from the STU to the heat sink at  $x = L$ ,  $Q_{rej}$ , is:

$$Q_{rej} = (A_p \bar{k}_{p,N} / \lambda_{p,N}) (T_p^{(N)} - T_c) + (A_n \bar{k}_{n,M} / \lambda_{n,M}) (T_n^{(M)} - T_c) + 0.5 I^2 (\bar{\rho}_{p,N} \lambda_{p,N} / A_p) \\ + 0.5 I^2 (\bar{\rho}_{n,M} \lambda_{n,M} / A_n) + 0.5 I T_p^{(N)} \beta'_p + 0.5 I T_n^{(M)} \beta'_n + I T_c \alpha_{pn}(T_c), \quad (2-10a)$$

where,

$$\beta'_p = (T_c / T_p^{(N)}) (\bar{\alpha}_{p,N} - \alpha_{p,N}(T_c)) + (\alpha_{p,N}(T_p^{(N)}) - \bar{\alpha}_{p,N}), \text{ and} \quad (2-10b)$$

$$\beta'_n = (T_c / T_n^{(M)}) (\alpha_{n,M}(T_c) - \bar{\alpha}_{n,M}) + (\bar{\alpha}_{n,M} - \alpha_{n,M}(T_n^{(M)})).$$

The expression for the conversion efficiency in Eq. (2-7) is rewritten in terms of  $ZT_h$ , as:

$$\eta = \left( (1 + m')^2 (\eta_{Carnot} Z T_h m')^{-1} - 0.5 f (m')^{-1} + (1 + m') \hat{\alpha} (\eta_{Carnot} m' \alpha')^{-1} \right)^{-1}, \quad (2-11)$$

where,

$$m' = R_L / R_{int}, \quad K_{p,1} = \bar{k}_{p,1} / \lambda_{p,1}, \quad K_{n,1} = \bar{k}_{n,1} / \lambda_{n,1}, \quad \eta_{Carnot} = 1 - (T_c / T_h),$$

$$\Theta_{p,1} = (T_h - T_p^{(2)}) / (T_h - T_c), \quad \Theta_{n,1} = (T_h - T_n^{(2)}) / (T_h - T_c), \quad (2-12)$$

$$f = \frac{\sqrt{K_{p,1} \Theta_{p,1} R_{p,1}'^2 R_n'} + \sqrt{K_{n,1} \Theta_{n,1} R_{n,1}'^2 R_p'}}{\sqrt{K_{p,1} \Theta_{p,1} R_p'^2 R_n'} + \sqrt{K_{n,1} \Theta_{n,1} R_n'^2 R_p'}}, \quad R_p' = \sum_{j=1}^N \bar{\rho}_{p,j} \lambda_{p,j}, \quad R_n' = \sum_{j=1}^M \bar{\rho}_{n,j} \lambda_{n,j},$$

$$\hat{\alpha} = \alpha_{pn}(T_h) - \frac{1}{2} (\beta_p + \beta_n), \text{ and } Z = \alpha'^2 (R_{int} (K_{p,1} A_p \Theta_{p,1} + K_{n,1} A_n \Theta_{n,1}))^{-1}.$$

Equation (2-11) is also the fitness function of the STU's conversion efficiency, which is optimized using the Genetic Algorithm (GA) as discussed in subsection 2.2.3.

### 2.2.2 Electric Power and Power Density

The electric power output of the STU can be expressed in terms of the thermoelectric properties of the material of the various segments in n- and p-legs as:

$$P_e = \alpha' (T_h - T_c) I - I^2 R_{int} \quad (2-13)$$

and in terms of the resistance of the external load,  $R_L$ , as:

$$P_e = I^2 R_L \quad (2-14)$$

Equating Eq. (2-13) and Eq. (2-14) gives the following expression for the load current:

$$I = \frac{\alpha' (T_h - T_c)}{R_{int} (1 + m')} \quad (2-15)$$

Substitute Eq. (2-15) into Eq. (2-14) gives the following expression for the electric power of the STU as:

$$P_e = \frac{\alpha'^2 (T_h - T_c)^2 m'}{(m'+1)^2}. \quad (2-16)$$

The electric power density of the STU,  $PD$ , is given as:

$$PD = (P_e / (A_p + A_n)) = \alpha'^2 (T_h - T_c)^2 m' \left( (1 + m')^2 R_{int} (A_p + A_n) \right)^{-1}. \quad (2-17)$$

This equation is the fitness function used for optimizing the electrical power density,  $PD$ , of the STU using the GA. The next section describes the Genetic Algorithms used for the optimization of the STU performance for either maximum conversion efficiency or the maximum  $PD$ .

### 2.2.3 Genetic Algorithms for Performance Optimization of STU Performance

In the genetic algorithm implemented in the present 1-D model of STUs, the expressions for the conversion efficiency (Eq. 2-11) and the electrical power density (Eq. 2-17), the nonlinear relations that need to be maximized, are refereed to as the fitness or objective functions. Such maximizations are subject to specified constraints (e.g.  $T_i^{(j)} > T_i^{(j+1)}$ ,  $j = 1, 2, \dots, N+1$  for p-leg and  $j = 1, 2, \dots, M+1$  for n-leg,  $\lambda_{i,j} > 0$ , etc). Owing to the nonlinear nature of the objective functions representing the conversion efficiency,  $\eta$ , and the electrical power density,  $PD$ , linear optimization methods could not be used (Press 1996). Such methods are restricted to maximizing linear objective functions or nonlinear objective functions that can be approximated by linear functions, subject only to linear constraints. The multiplier algorithm developed by Pierre and Lowe (1975) for maximizing nonlinear objective function subject to constraints and used initially in this work was discarded. This is because the optimization results are dependent on the non-linearity of the objective functions, the initial value of the variables (initial guess), and the specified search direction.

The Genetic Algorithm (GA) used in this work (Goldberg 1989) not only maximizes nonlinear objective functions subject to the user's specified constrains, but also the results are independent of the initial guess of the values of the variables and of the search direction. The GA search procedure uses random choice as a tool to guide a highly exploitative search through a coding of a parameter space. Implementing the GA for maximizing the conversion efficiency,  $\eta$  (Eq. 2-11) or the electric power density,  $PD$  (Eq. 2-17) of the STU are discussed next.

### 2.2.4 GA for Maximizing Conversion Efficiency and PD of STU

The fitness function representing the conversion efficiency of the STU (Eq. 2-11), is maximized using the GA (Goldberg 1989). Also, the fitness function to be maximized for the PD of the STU is given by Eq. (2-17). The input parameters for maximizing Eq. (2-11) or Eq. (2-17) are  $T_h$  and  $T_c$ , the thermometric materials (Figure 2-1) and the number of segments in n- and p-legs, the total length of the legs, and cross-sectional area of the p-leg  $A_p$  ( $A_n$  could also be used instead). The calculated optimized parameters are:

- (a) the cross-section area of n-leg,  $A_n$ ,
- (b) all interfacial temperatures at segments interfaces of n- and p-legs,
- (c) lengths of the segments in the n- and p-legs, and
- (d) the ratio of load resistance to total internal resistance,  $m'$ .

The maximization of Eqs. (2-11) and (2-17) using the GA is conducted subject to the following constraints:

$$A_n / A_p > 0, \lambda_{i,j} > 0, m' > 0, \quad (2-18a)$$

$$T_h - T_p^{(2)} > 0, T_p^{(2)} - T_p^{(3)} > 0, T_p^{(3)} - T_p^{(4)} > 0, T_p^{(4)} - T_p^{(5)} > 0, T_p^{(5)} - T_c > 0 \quad (2-18b)$$

$$T_h - T_n^{(2)} > 0, T_n^{(2)} - T_n^{(3)} > 0, T_n^{(3)} - T_n^{(4)} > 0, T_n^{(4)} - T_n^{(5)} > 0, \text{ and } T_n^{(5)} - T_c > 0. \quad (2-18c)$$

Additional constraints include the maximum operation temperatures,  $T_{pi}^{\max}$ , of the thermoelectric materials in the various segments,  $Pi$  ( $i = 1, 2, \dots, 5$ ). These temperatures are determined based on consideration of vapor pressure, compatibility with the TE materials in adjacent segments, and avoiding excessive loss of volatile dopants; other constraints could also be added as needed. Thus the temperature constraints for the p-leg, are:

$$T_h \leq T_{p1}^{\max}, T_p^{(2)} \leq T_{p2}^{\max}, T_p^{(3)} \leq T_{p3}^{\max}, T_p^{(4)} \leq T_{p4}^{\max}, \text{ and } T_p^{(5)} \leq T_{p5}^{\max} \quad (2-19)$$

Similarly, in the n-leg, the additional temperature constraints are as follows:

$$T_h \leq T_{n1}^{\max}, T_n^{(2)} \leq T_{n2}^{\max}, T_n^{(3)} \leq T_{n3}^{\max}, T_n^{(4)} \leq T_{n4}^{\max}, \text{ and } T_n^{(5)} \leq T_{n5}^{\max}. \quad (2-20)$$

## 2.3 Comparison with the Model of Swanson et al. (1961)

Table 2-1 compares the present model with the approximate analytical model by Swanson et al. (1961) that has been widely used to model STUs. Although the governing equation in both models is the same, the thermoelectric properties in Swanson's et al. are evaluated based on

Table 2-1 Comparison of the Present Model and That of Swanson et al. (1961)

Specifics	Present Model	Swanson et al. (1961)
Governing Eq.	$\bar{k}_{i,j} (d^2 T_{i,j} / dx^2) + q_{i,j}'' + q_{j,i,j}'' = 0$	Same except for $\bar{k}_{i,j}$
Joule Heating	Based on volume averaging, $q_j'' = J^2 \bar{\rho}_{i,j}$	Based on temperature averaging of $\rho_{i,j}$
Thomson Heating	Accounts for dependence of $\alpha_{i,j}$ on temperature $q_{i,j}''' = - \left( J_i / \lambda_{i,j} \right) \int_{\lambda_{i,j}}^{T_{i,j}(x)} (d\alpha_{i,j} / dT_{i,j}) (dT_{i,j} / dx) dx,$	Assumes linear temperature dependences of the Seebeck coefficient $d\alpha_{i,j} / dT_{i,j}$
Properties	Based on volume integral averaging $\bar{k}_{i,j} = (1/\lambda_{i,j}) \int_{\lambda_{i,j}} k_{i,j}(T_{i,j}(x)) dx$ $\bar{\rho}_{i,j} = (1/\lambda_{i,j}) \int_{\lambda_{i,j}} \rho_{i,j}(T_{i,j}(x)) dx$ $\bar{\alpha}_{i,j} = (1/\lambda_{i,j}) \int_{\lambda_{i,j}} \alpha_{i,j}(T_{i,j}(x)) dx$	Based on temperature averaging $\bar{k}_{i,j} = (1/\Delta T_{i,j}) \int_{T_{i,j}} k_{i,j}(T_{i,j}) dT_{i,j}$ $\bar{\rho}_{i,j} = (1/\Delta T_{i,j}) \int_{T_{i,j}} \rho_{i,j}(T_{i,j}) dT_{i,j}$ $\bar{\alpha}_{i,j} = (1/\Delta T_{i,j}) \int_{T_{i,j}} \alpha_{i,j}(T_{i,j}) dT_{i,j}$
Peak Conversion Efficiency	$\eta_{\max} = \eta_{Carnot} \Psi$ $\Psi = \left[ m'_{opt} / \left( \left( (1 + m'_{opt})^2 / Z_{\max} T_h \right) + (\hat{\alpha}/\alpha') (1 + m'_{opt}) - 0.5 f \eta_{Carnot} \right) \right]$ $m'_{opt} = \sqrt{1 + Z_{\max} T_h ((\hat{\alpha}/\alpha') - 0.5 f \eta_{Carnot})}$ $f = \frac{\sqrt{K_{p,1} \ominus_{p,1} R_{p,1}'^2 R_n'} + \sqrt{K_{n,1} \ominus_{n,1} R_{n,1}'^2 R_p'}}{\sqrt{K_{p,1} \ominus_{p,1} R_p'^2 R_n'} + \sqrt{K_{n,1} \ominus_{n,1} R_n'^2 R_p'}}$	Same  Same $m'_{opt} = \sqrt{1 + Z_{\max} T_h (\hat{\alpha}/\alpha')}$
Condition for $Z_{\max}$	$(A_n/A_p)_{opt} = ((\ominus_{p,1} K_{p,1} R_n') / (\ominus_{n,1} K_{n,1} R_p'))^{0.5}$	Same
Overall Energy Balance	Satisfied ( $\eta$ calculated based on $P_e$ and $Q_{in}$ is identical to that calculated based on $Q_{rej}$ and $Q_{in}$ , Table 2-2).	Not satisfied ( $\eta$ calculated based on $P_e$ and $Q_{in}$ is different from that calculated based on $Q_{rej}$ and $Q_{in}$ , Table 2-2).

temperature averaging rather than volume averaging, which is the case in the present model. Additional approximations used in the model by Swanson et al. (1961) are listed in Table 2-1. The model of Swanson et al. (1961) can only be used for maximizing the conversion efficiency and does not apply for maximizing the power density of a STU.

A close examination of the reported expressions by Swanson et al. (1961) for the input and rejected thermal powers and of the electrical power, the conversion efficiency calculated from the electrical power output and the input thermal power is different from that calculated from the input and rejected thermal powers. This variance is because the model by Swanson et al. (1961) does not satisfy the overall energy balance. Furthermore, the peak conversion efficiency calculated using the derived expression by Swanson et al. (1961) is not only different from that determined from the energy balance, but also does not occur at  $m'_{opt}$  (Table 2-1). To better quantify these points, calculations are performed using the present model and that of Swanson et al. (1961) at the same hot and cold junction temperatures, total length, and cross sectional area of

Table 2-2 Predictions Comparison of the Present Model and That of Swanson et al. (1961).

<i>Parameters</i>	<i>Present Model</i>	<i>Swanson et al. (1961)</i>
$L$ (mm) (input)	10	10
$A_p$ (mm <sup>2</sup> ) (input)	100	100
Calculated $Q_{in}$ (W)	67.13	66.11
Calculated $Q_{rej}$ (W)	58.21	58.08
Calculated $P_e$ (W)	8.92	8.81
Residual Power (W) ( $Q_{in} - Q_{rej} - P_e$ )	0.0	-0.78
Peak Efficiency (%)	$(P_e/Q_{in}) = 13.29\%$ $(1 - Q_{rej}/Q_{in}) = 13.29\%$	$\eta = P_e/Q_{in} = 13.33\%$ $\eta = 1 - Q_{rej}/Q_{in} = 12.15\%$
$A_n$ (mm <sup>2</sup> )	88.26	88.31
$\lambda_{p,1}, \lambda_{p,2}, \lambda_{p,3}$ (mm)	5.089, 0.681, 4.230	5.104, 0.681, 4.215
$\lambda_{n,1}, \lambda_{n,2}$ (mm)	5.364, 4.636	5.361, 4.639
$I$ (A)	35.756	34.327
$m'_{opt}$ ( $R_L/R_{int}$ )	1.383	1.481

the p-leg in a STU. The results of this comparison listed in Table 2-2 show that, while the present model fully satisfies the overall energy balance, the calculations using Swanson's et al. model (1961) clearly show that the overall energy balance is not satisfied, with a residue of 0.78 W (> 1%). Furthermore, the peak conversion efficiency calculated by Swanson's et al. (1961) based on the electrical power and the input thermal power (13.33%) is different from that calculated based on the input and rejected thermal powers (12.15%). In the present model, both values for the peak efficiency (13.29%) are identical. As a result, the optimized dimensions of the STU and the value of  $m'_{opt}$  obtained by the present model are different from those calculated using the model by Swanson et al. (1961).

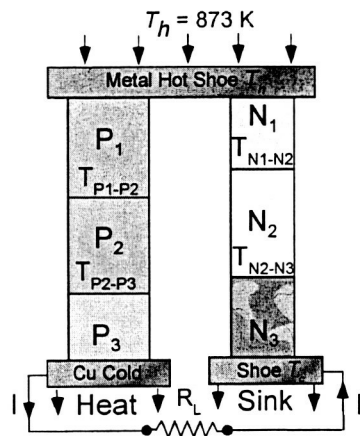
Table 2-3 Comparison of Present Model with Experimental Data of SiGe Unicouples\*.

Performance Parameters	3 hrs Test		1100 hrs Test	
	$T_h = 1272.8 \text{ K} \ \& \ T_c = 573.6 \text{ K}$		$T_h = 1275.1 \text{ K} \ \& \ T_c = 569.5 \text{ K}$	
	Experimental Data (GE 1980)	Model Predictions	Experimental Data (GE 1980)	Model Predictions
Open circuit voltage (V)	0.34094	0.35409	0.35933	0.35646
Load current (A)	2.469	2.469	2.483	2.483
Load voltage (V)	0.202389	0.217092	0.202556	0.202319
Total resistance ( $\Omega$ )	0.05611	0.055738	0.06367	0.062349
Electrical power ( $W_e$ )	0.500	0.535372	0.5028	0.501851
Efficiency (%)	-	7.653	-	7.132
Input thermal power ( $W_{th}$ ) / heat flux ( $W_{th}/cm^2$ )	-	6.997/39.23	-	7.035/39.44
Rejected power ( $W_{th}$ ) / heat flux ( $W_{th}/cm^2$ )	-	6.461/36.22	-	6.532/36.62

\*( $A_p = A_n = 2.7432 \text{ mm} \times 6.5024 \text{ mm}$ ,  $L = 20.32 \text{ mm}$  (Kelly 1975)).

## 2.4 Prediction Verification of the Present STU Model

The predictions of the present model are compared with the reported measurements for two non-segmented SiGe unicouples, which are identical to those used in State-Of-Art (SOA)-RTGs (Kelly 1975 and GE 1980). No performance data has been found in the open literature for STUs, but some has been generated in this work and reported in chapter 5. The two unicouples which



(a)

**p-leg materials:**

$P_1$ :  $\text{CeFe}_{3.5}\text{Co}_{0.5}\text{Sb}_{12}$ ,

$P_2$ :  $\text{Zn}_4\text{Sb}_3$ ,

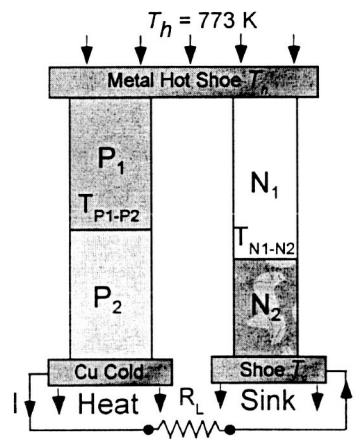
$P_3$ :  $\text{Bi}_{0.5}\text{Sb}_{1.5}\text{Te}_3$

**n-leg materials:**

$N_1$ :  $\text{CoSb}_3$ ,

$N_2$ :  $2\text{N-PbTe}$ ,

$N_3$ :  $\text{Bi}_2\text{Te}_{2.95}\text{Se}_{0.05}$



(b)

**p-leg materials:**

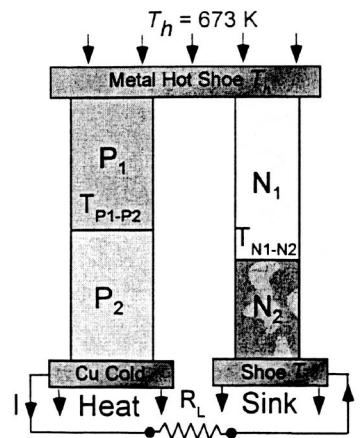
$P_1$ : TAGS-85,

$P_2$ :  $\text{Bi}_{0.5}\text{Sb}_{1.5}\text{Te}_3$

**n-leg materials:**

$N_1$ :  $2\text{N-PbTe}$ ,

$N_2$ :  $\text{Bi}_2\text{Te}_{2.95}\text{Se}_{0.05}$



(c)

**p-leg materials:**

$P_1$ :  $\text{Zn}_4\text{Sb}_3$ ,

$P_2$ :  $\text{Bi}_{0.5}\text{Sb}_{1.5}\text{Te}_3$

**n-leg materials:**

$N_1$ :  $2\text{N-PbTe}$ ,

$N_2$ :  $\text{Bi}_2\text{Te}_{2.95}\text{Se}_{0.05}$

Figure 2-3 Optimized STUs for Maximum Efficiency.



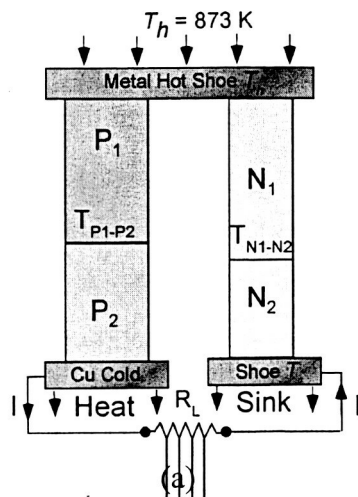
are the subject of this comparison have been tested for three hours and 1100 hours, respectively (Kelly 1975 and GE 1980), and the reported test data and the present predictions are compared in Table 2-3. The data included the open circuit voltage and both the terminal voltage and electrical power output at a load current of 2.469 A and 2.483 A, respectively. In addition, the measured total resistances of the unicouples and the hot junction and cold junction temperatures used in these tests are also listed in Table 2-3. For almost the same total uncouple resistance, the present model predictions are in excellent agreement with the reported measurements, confirming the soundness of the model.

## 2.5 Results and Discussions

In this section, the performance of a number of STUs, comprised of segments of  $\text{CeFe}_{3.5}\text{Co}_{0.5}\text{Sb}_{12}$ ,  $\text{Zn}_4\text{Sb}_3$ , TAGS-85, and  $\text{Bi}_{0.5}\text{Sb}_{1.5}\text{Te}_3$  alloys in the p-leg and  $\text{CoSb}_3$ , 2N-PbTe, and  $\text{Bi}_2\text{Te}_{2.95}\text{Se}_{0.05}$  alloys in the n-legs, are optimized both for maximum conversion efficiency and maximum electrical power density operation, using the present STU model. The analysis is conducted for a cold junction temperature,  $T_c = 298$  K, and hot junction temperatures,  $T_h = 873$  K, 773 K and 673 K. The properties database (Figure 2-1) used in the present analysis is credited to the Jet Propulsion Laboratory, California Institute of Technology, except for that for 2N-PbTe which is credited to Hi-Zi, Inc., and that of TAGS-85 which is obtained from Skrabek and Trimmer (1994). To demonstrate the effect of the contact resistance on the performance of the STUs (Figure 2-3 and Figure 2-4), performance results obtained for zero and  $150 \mu\Omega\text{-cm}^2$  total contact resistance per leg and compared in the next subsections.

### 2.5.1 STUs Performance

In the present analysis, the total length of the n- and p-legs is taken equal to 5 mm and the cross-sectional area of the p-leg is taken  $4.0 \text{ mm}^2$ . The cross-sectional area of the n-leg is determined when optimizing the operation of STUs for either maximum efficiency or maximum electrical power density. Figure 2-3 and Figure 2-4 present the STUs optimized for maximum efficiency and for maximum power density operation, respectively, at  $T_h = 873$  K, 773 K, and 673 K, and the same  $T_c = 298$  K. For  $T_h = 873$  K (Figure 2-3a and Figure 2-4a), the number of segments in the p- and n-legs, when STUs are optimized for maximum electrical power density, are generally fewer than when they are optimized for maximum efficiency operation. At lower



**p-leg materials:**

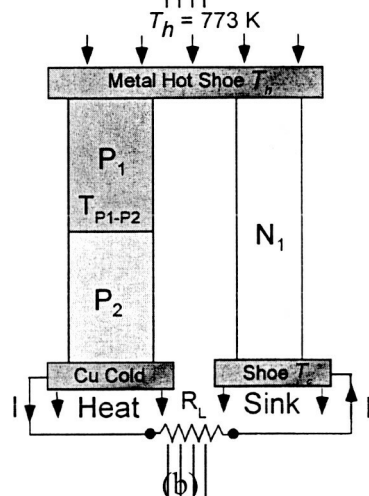
$P_1$ :  $\text{CeFe}_{3.5}\text{Co}_{0.5}\text{Sb}_{12}$ ,

$P_2$ :  $\text{Bi}_{0.5}\text{Sb}_{1.5}\text{Te}_3$

**n-leg materials:**

$N_1$ :  $\text{CoSb}_3$ ,

$N_2$ :  $2\text{N-PbTe}$



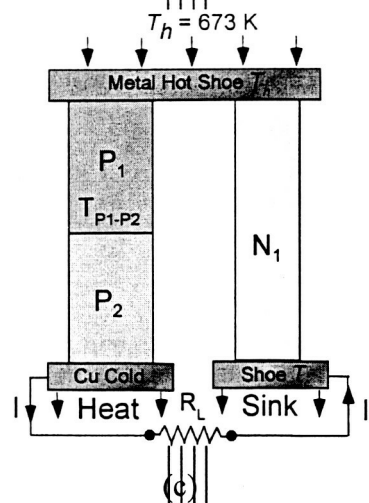
**p-leg materials:**

$P_1$ : TAGS-85,

$P_2$ :  $\text{Bi}_{0.5}\text{Sb}_{1.5}\text{Te}_3$

**n-leg materials:**

$N_1$ :  $2\text{N-PbTe}$



**p-leg materials:**

$P_1$ :  $\text{Zn}_4\text{Sb}_3$ ,

$P_2$ :  $\text{Bi}_{0.5}\text{Sb}_{1.5}\text{Te}_3$

**n-leg materials:**

$N_1$ :  $2\text{N-PbTe}$

Figure 2-4 Optimized STUs for Maximum Power Density.

hot junction temperatures of 773 K and 673 K, however, the number and materials of the segments in the p- legs are the same, but their lengths are different (Figure 2-3b, c, and Figure 2-4b, c). As indicated earlier, optimizing the STUs for maximum power density operation generally requires fewer segments in the legs (Figure 2-3 and Figure 2-4). When using the same number and materials of the segments as for when the STU is optimized for maximum conversion efficiency, the performance results insignificantly change, but the thickness of the added segments becomes infinitesimally small to be practical.

Figure 2-5a and Figure 2-5b presents the obtained performance results for the STUs (Figure 2-3 and Figure 2-4) optimized for maximum efficiency and maximum electrical power density, respectively, at different hot junction temperatures. In these figures, the solid circles indicate the peak efficiency and the open triangles indicate the conversion efficiency at the peak electric power. The portions of the curves shown in solid lines indicate the portions of the performance curves where the STUs are load-following, that is an increase in the load demand increases in the electrical power generated by the STUs. The portions of the curves in Figure 2-5a and Figure 2-5b shown in dashed lines represent the non-load following portions of the performance curves, which are of no practical value.

In the load-following portions of the characteristics in Figure 2-5a and Figure 2-5b, an increase in the external load demand, or electric current, increases the electrical power output of the STUs. Ideally, nominal operation points for the STUs are selected either at the peak efficiency, or somewhere between the peak efficiency and that corresponding to the peak electrical power. The exact operation point will depend, however, on the desired percentage increase in electric power to the load, beyond nominal, while STU still in the load following portions of the performance curves.

As indicated in Figure 2-6a and Figure 2-6b, the peak electric powers mark the end of the load following portions of performance curves. Increasing the electrical power output beyond that at the peak efficiency would be at the expense of lowering the conversion efficiency and increasing the demand on the heat source. Figure 2-6a and Figure 2-6b indicate that the peak electrical power is generally about ~2.1% higher than that at the peak efficiency. If the desired operation margins were higher than this percentage, nominal operation point would be moved further to the left of the peak efficiency (Figure 2-5 - Figure 2-6).

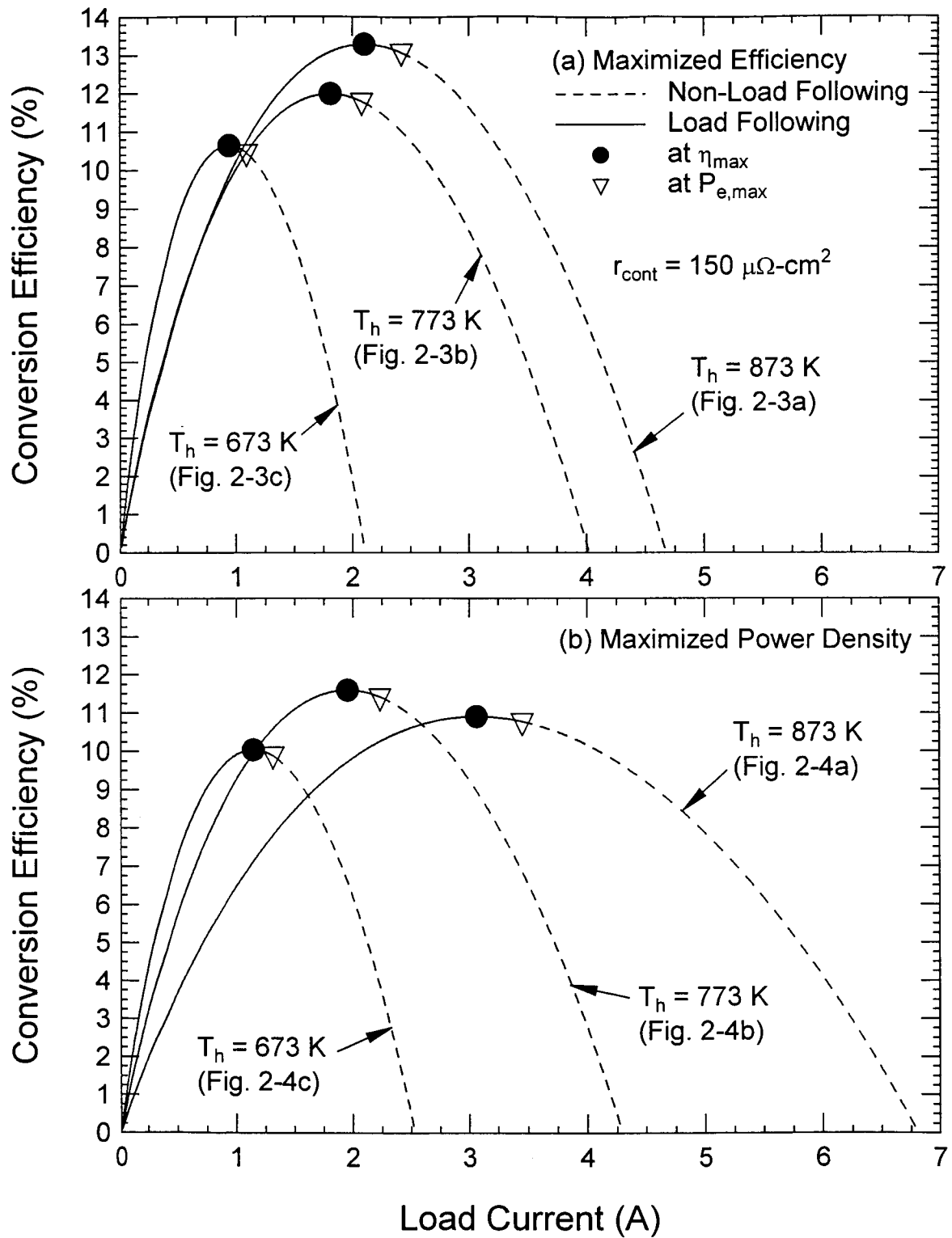


Figure 2-5 Calculated Conversion Efficiency for the STUs.

### 2.5.2 Effect of Contact Resistance

The results delineated in Figure 2-6 show that for a zero contact resistance, the calculated peak efficiencies and peak electrical powers of STUs are higher than when the assumed contact resistance per leg is  $150 \mu\Omega\text{-cm}^2$ . The differences between the peak efficiencies and peak electrical powers at these contact resistances increase as the hot junction temperature increases, reaching  $\sim 16\%$  and  $25\%$ , respectively, at  $T_h = 873 \text{ K}$  (Figure 2-6b). For the STUs optimized for maximum conversion efficiency operation (Figure 2-6a), the effect of the contact resistance on the electrical power output is smaller than for the STUs optimized for maximum electrical power density (Figure 2-6b). Figure 2-6a shows that not only the peak efficiency and the peak electrical power decrease, but also they shift to lower currents as the hot junction temperature decreases. For the STUs optimized for maximum power density, however, when  $T_h = 873 \text{ K}$  the peak conversion efficiencies and those at the peak electrical powers could be as much as  $16\%$  lower than those of the STUs optimized for maximum efficiency. This difference decreases to  $< 6\%$  as the hot junction temperature decreases to  $673 \text{ K}$  (Figure 2-6a and Figure 2-6b).

When the contact resistance per leg is assumed  $150 \mu\Omega\text{-cm}^2$ , the peak efficiency increases from  $\sim 10.9\%$  to  $\sim 11.6\%$  as the hot junction temperature decreases from  $873 \text{ K}$  to  $773 \text{ K}$ , then decreases to  $\sim 10\%$  at  $T_h = 673 \text{ K}$  (Figure 2-5b). These efficiencies are lower than for the STUs optimized for maximum efficiency operation of  $13.3\%$ ,  $12\%$ , and  $10.7\%$  at  $T_h = 873 \text{ K}$ ,  $773 \text{ K}$ , and  $673 \text{ K}$ , respectively (Figure 2-5a and Figure 2-6a). With a zero contact resistance, the peak efficiencies are  $15\%$ ,  $13.3\%$ , and  $11.7\%$ , respectively (Figure 2-6a). Figure 2-6a and Figure 2-6b also show that for the STUs optimized for maximum power density, the peak electrical powers are much higher than for those optimized for maximum conversion efficiency. For example, at  $T_h = 873 \text{ K}$ ,  $773 \text{ K}$ , and  $673 \text{ K}$  the predicted peak electric power is  $0.48$ ,  $0.27$  and  $0.12 \text{ W}_e$ , respectively, when assuming a zero contact resistance (Figure 2-6b). The peak electrical powers indicated in Figure 2-6a and Figure 2-6b decrease as the contact resistance per leg increases to  $150 \mu\Omega\text{-cm}^2$ .

### 2.5.3 Interfacial Temperatures

Figure 2-7a - Figure 2-7c shows the calculated interfacial temperatures in the legs for the STUs optimized for maximum efficiency (solid lines) and for maximum electrical power density

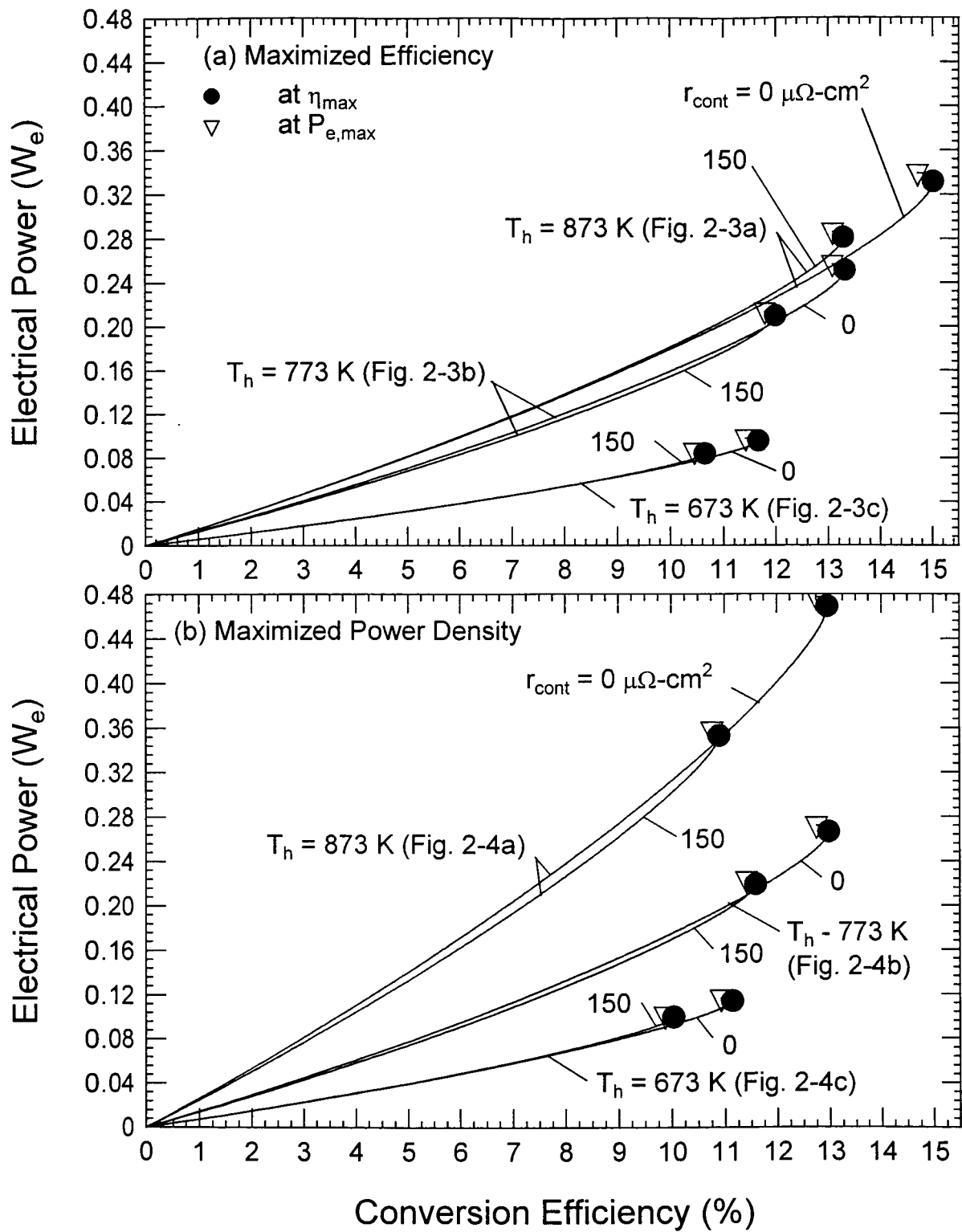


Figure 2-6 Predicted Performance Characteristics for the STUs.

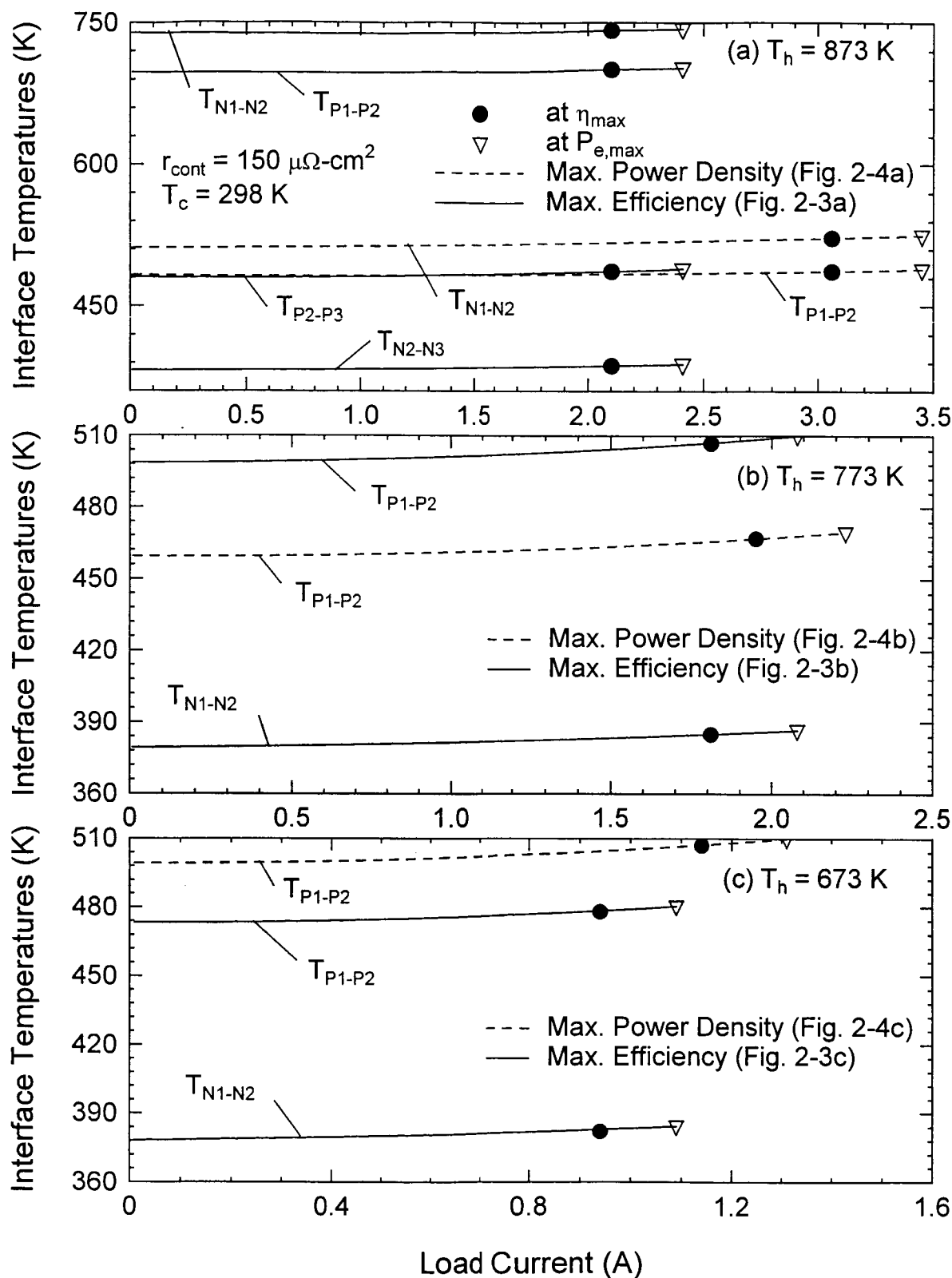


Figure 2-7 Calculated Interface Temperatures for the STUs.

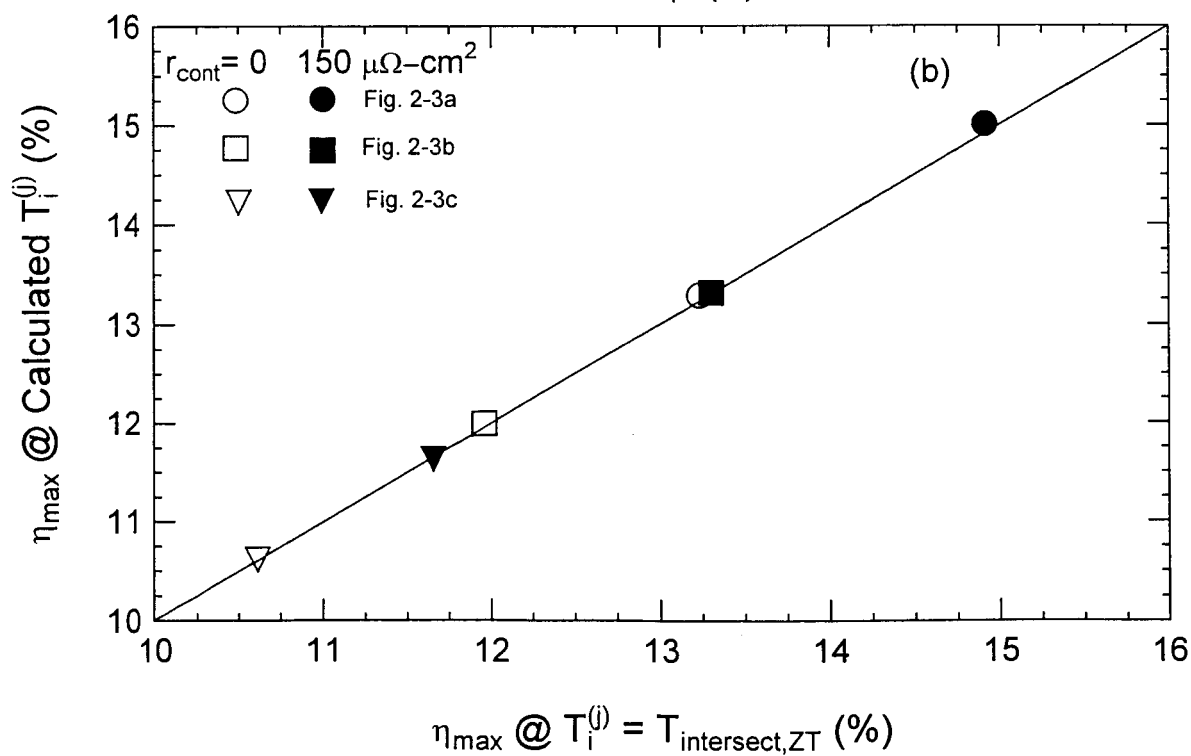
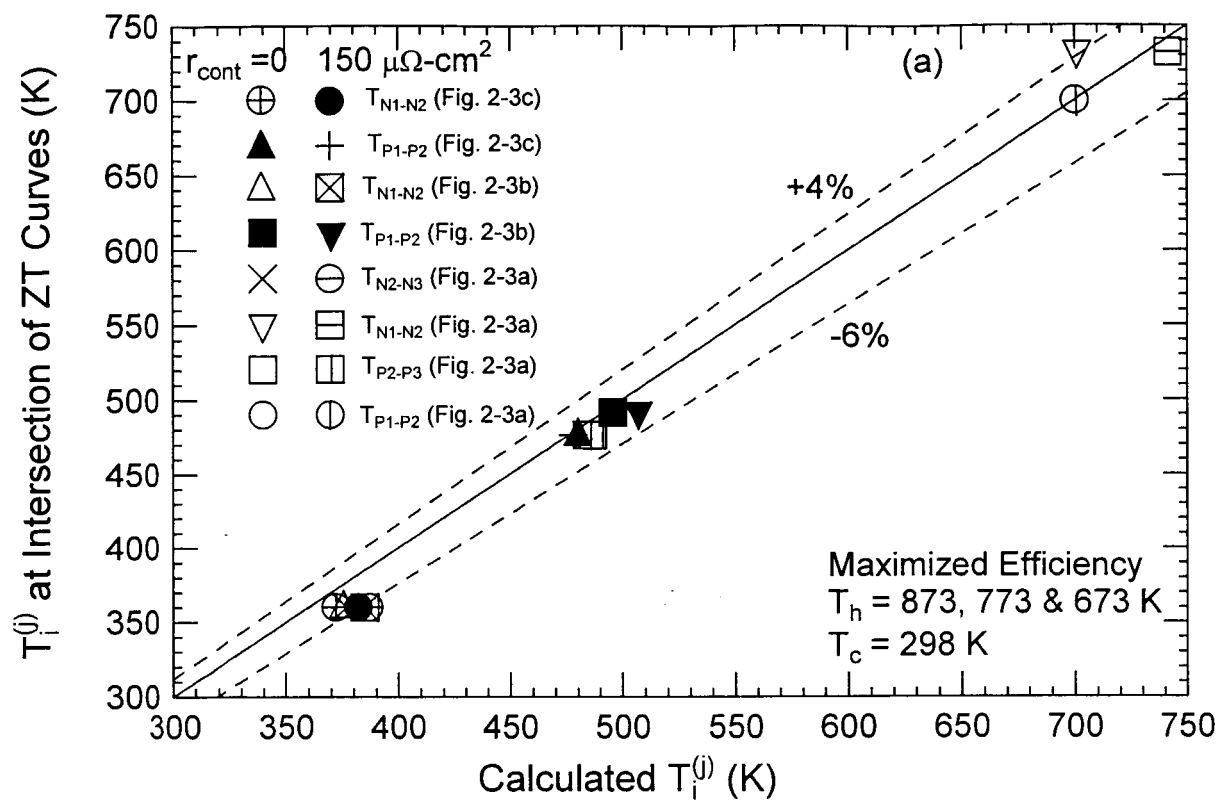


Figure 2-8 Calculated Interface Temperatures and  $\eta_{\text{max}}$ .



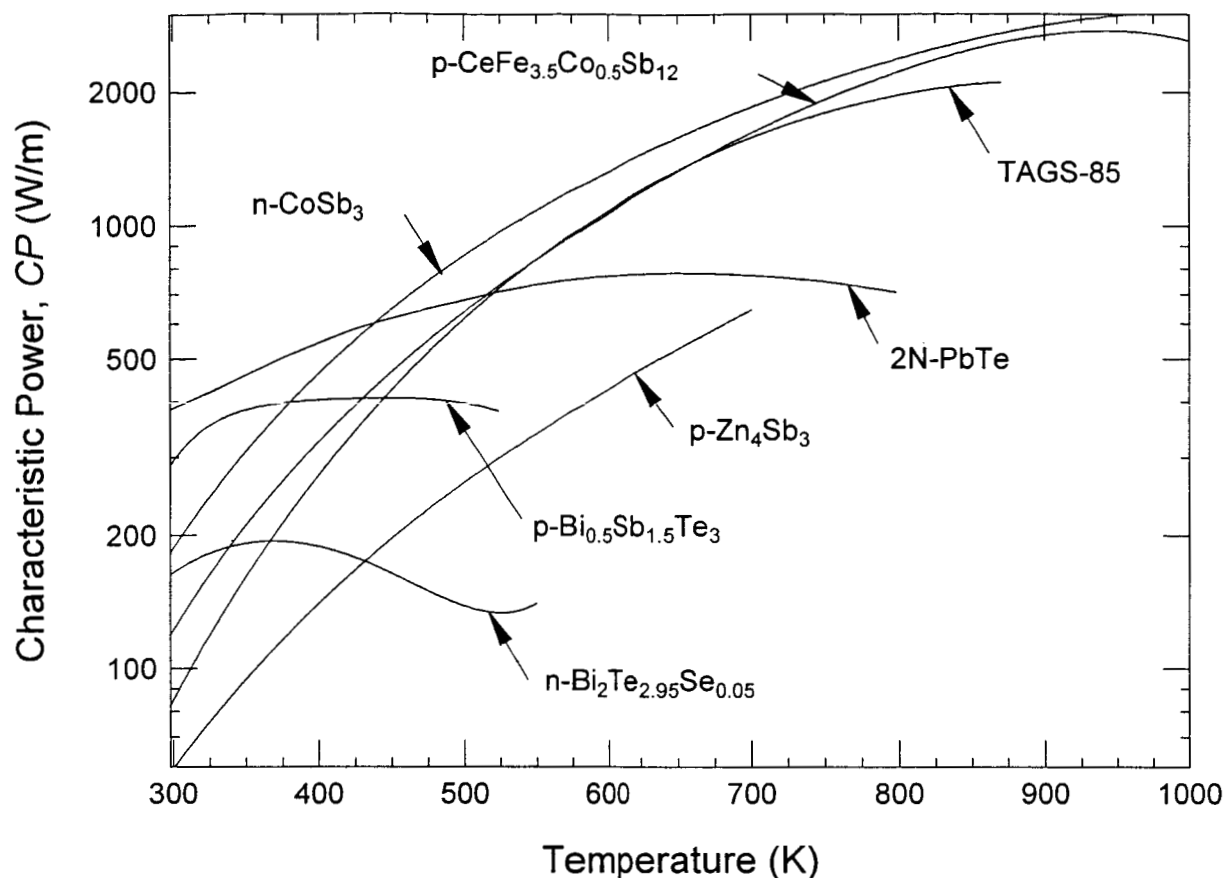


Figure 2-9 Characteristic Power of Different TE Materials.

(dashed lines), assuming a contact resistance of  $150 \mu\Omega\text{-cm}^2$  per leg. At  $T_h = 873 \text{ K}$  (Figure 2-7a), the STU optimized for maximum power density (Figure 2-4a) has only two segments in each of the n- and p-legs, versus three segments each in the STU optimized for maximum efficiency (Figure 2-3a). The interfacial temperature between the bottom two segments in the p-leg of the STU in Figure 2-3a,  $T_{P2-P3}$ , is almost same as for the STU in Figure 2-4a,  $T_{P1-P2}$ , but the interfacial temperature between the segments in the n-leg of the latter,  $T_{N1-N2}$ , is much lower and higher than those between the middle and the top and bottom segments in the n-leg of STU in Figure 2-3a, respectively.

In Figure 2-7b and Figure 2-7c, the p-leg of each the STUs optimized for maximum efficiency and, maximum power density has two segments (Figure 2-3b & c, and Figure 2-4b & c). Note that the interfacial temperature in the p-leg of the STU optimized for maximum power density is lower than for the STU optimized for maximum efficiency, when  $T_h = 773 \text{ K}$  (Figure 2-7b), but higher when  $T_h = 673 \text{ K}$  (Figure 2-7c).

At  $T_h = 873$  K, when  $r_{\text{cont}} = 0$  and  $150 \mu\Omega\text{-cm}^2$ , the calculated maximum efficiency,  $\eta_{\text{max}}$ , is 15%, and 13.3%, respectively (Figure 2-8b). When  $r_{\text{cont}} = 0$ , the calculated interface temperatures,  $T_{P1-P2}$ ,  $T_{P2-P3}$ ,  $T_{N1-N2}$ , and  $T_{N2-N3}$  are 700, 485, 701, and 376 K, respectively, and 700, 487, 741 and 387 K, respectively, when  $r_{\text{cont}} = 150 \mu\Omega\text{-cm}^2$  (Figure 2-8a). These temperatures are close to those at the intersections of the  $ZT$  curves (Figure 2-1) of the thermoelectric materials in the adjacent segments in the p- and n-legs of 700, 476, 732, 360 K, respectively (Figure 2-8a). As indicated in this figure, the differences between the calculated interfacial temperatures and those at the intersections of the  $ZT$  curves in Figure 2-1 vary from +4% to -6%. When the latter interfacial temperatures are imposed onto the GA maximization of the conversion efficiency, the performance parameters such as  $\eta_{\text{max}}$  and electrical power output are almost the same (Figure 2-8b). Therefore, for maximizing the efficiency of STUs, the interface temperatures in n- and p-legs could be taken as those at the intersections of the  $ZT$  curves of the materials of the adjacent segments in the n- and p-legs (Figure 2-1).

When maximizing the PD, the calculated interfacial temperatures in the STU are as much as 51% lower than the temperatures at the interactions of the  $ZT$  curves of the materials (Figure 2-1) in the adjacent segments in the n- and p-legs, or at which the  $ZT$  curves do not intersect. Conversely, when the thermoelectric properties are presented in terms of characteristic power,  $CP$ , defined as:  $CP = T^2 Zk$ , where  $k$  is the material thermal conductivity, versus temperature (Figure 2-9), the calculated interfacial temperatures are within 10-15% of those at the intersections of the  $CP$  curves of the materials in adjacent segments in the n- and p-legs (Figure 2-10a).

For example, for STU in Figure 2-3a, when  $r_{\text{cont}} = 0$  the calculated  $T_{N1-N2} = 483$  K versus 731 K at the intersection of  $ZT$  curves (Figure 2-1) of TE material in  $N_1$  and  $N_2$ , and the calculated  $T_{P1-P2}$  of 461 K and the  $ZT$  curves of TE in  $P_1$  and  $P_2$  do not intersect (Figure 2-1). Conversely, the corresponding values at the intersections of the  $CP$  curves of the materials of the segments in the n- and p-legs are 438 and 430 K, respectively (Figure 2-9 and Figure 2-10a). The calculated values of  $PD_{\text{max}}$  are almost the same as those obtained when the interfacial temperatures are taken the same as those at the intersections of  $CP$  curves (Figure 2-10b).

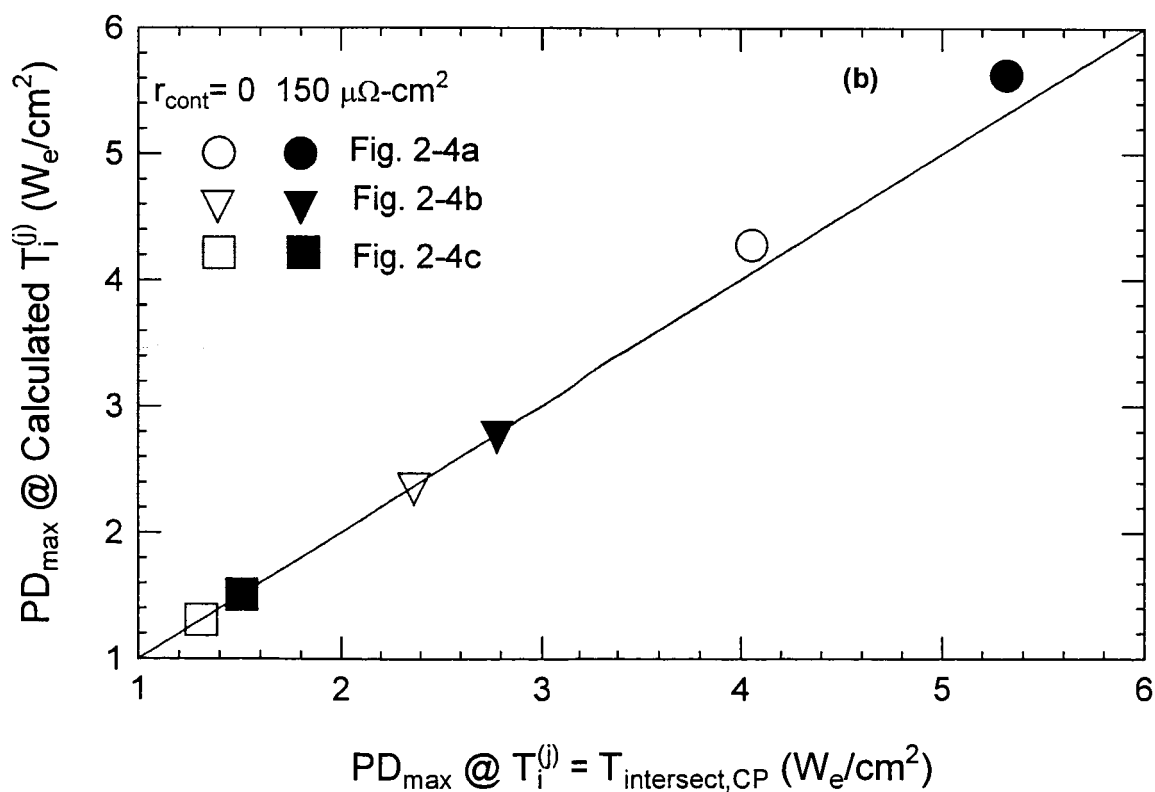
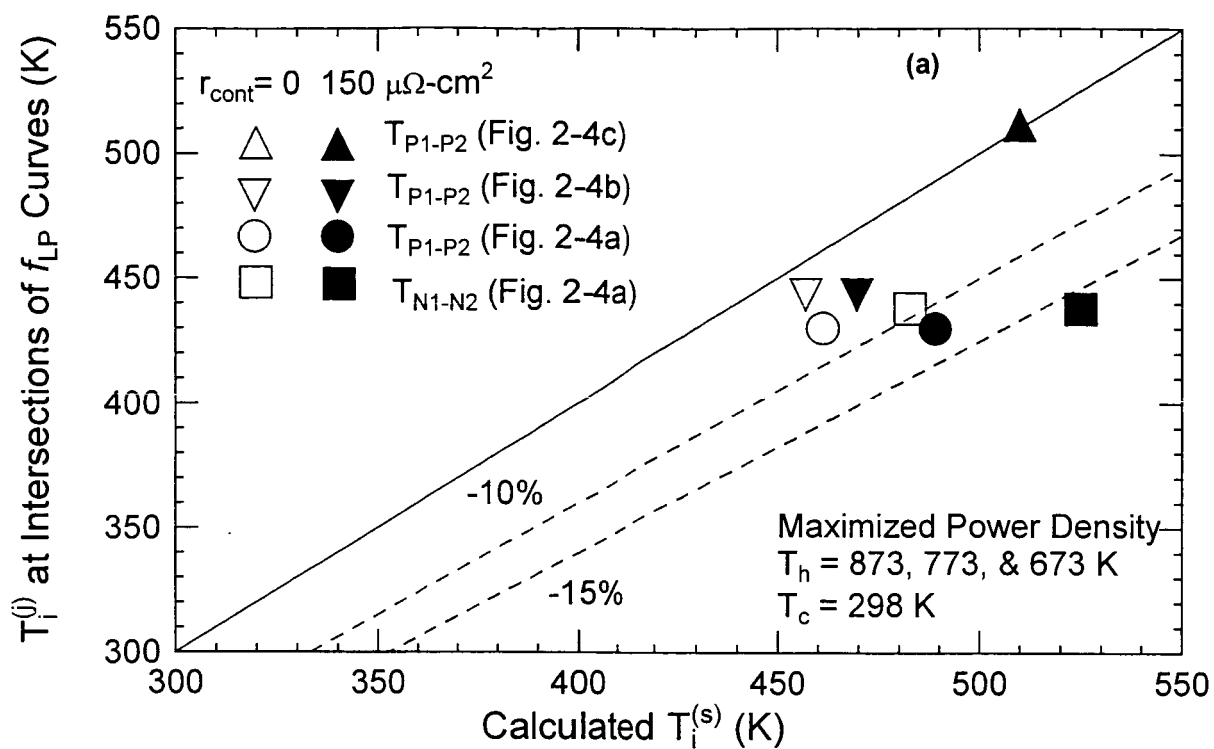


Figure 2-10 Calculated Interface Temperatures and  $PD_{\text{max}}$ .

## 2.6 Summary and Conclusions

A 1-D analytical model in conjunction with a Genetic Algorithm (GA) is developed to optimize the STUs for either maximum conversion efficiency or maximum electric power density. This model, which assumes zero side heat losses, accounts for the change in the physical and thermoelectric properties with temperature. Results showed that when maximizing the conversion efficiency, the interfacial temperatures of the segments in the n- and p-legs could be taken same as those at the intersections of the  $ZT$  curves (Figure 2-1) of the TE materials in adjacent segments. This is not true, however, when maximizing electrical power density. For the latter, interfacial temperatures could be taken as those at the intersection of the  $CP$  curves (Figure 2-9) of the TE materials in adjacent segments.

Model predictions are in agreement with reported test data by Kelly (1975) and GE (1980) of non-segmented SiGe generators used in SOA-RTGs. The comparisons of the model predictions with that of Swanson et al. (1961) have clearly showed the limitation of the latter. These include inconsistency and inaccuracy of predictions of the maximum conversion efficiency and the corresponding load current. In addition, the model by Swanson et al. (1961) is not suitable for the optimization of STUs for maximum power density operation, which is of primary interest to space power applications. It is worth noting that prior to completing the present model, the model by Swanson et al. (1961) has been widely used.

To qualify the effect of the contact resistance, the model results with contact resistances per leg of zero and  $150 \mu\Omega\text{-cm}^2$  are compared for hot junction temperatures of 873 K, 773 K, and 673K, but the same cold junction temperature of 298 K. The latter resistance is similar to that of SiGe in SOA-RTGs. For STUs optimized for maximum efficiency, peak efficiencies of 15%, 13.3%, and 11.7% are predicted at  $T_h = 873 \text{ K}$ , 773 K, and 673 K, respectively, when assuming zero contact resistance. These efficiencies decrease to  $\sim 13.3\%$ , 12% and 10.7%, respectively, when the contact resistance per leg increases to  $150 \mu\Omega\text{-cm}^2$ . At the same values of  $T_h$ , STUs optimized for maximum power density operate at  $\sim 6$  -18% lower peak conversion efficiencies, but at up to 40% higher peak electrical powers.

### 3 A THREE-DIMENSIONAL, PERFORMANCE MODEL OF SEGMENTED THERMOELECTRIC UNICOUPLES (UNM-ISNPS)

In this chapter, a three-dimensional model of Segmented Thermoelectric Unicouples (STUs) is developed and incorporated into the ANSYS commercial software. The governing equations are solved, subject to the prescribed boundary conditions, using the Finite Element Methodology (FEM) techniques and meshing capabilities in ANSYS. The model accounts for the side heat losses, handles different types of boundary conditions, and accounts for the non-homogeneity and the change in physical and thermoelectric properties of the segments materials in the n- and p-legs with temperature. The model predictions are compared with experimental data of two skutterudites-based STUs, uni8 and uni12, comprised of n-type  $\text{Bi}_2\text{Te}_{2.95}\text{Se}_{0.05}$  and  $\text{CoSb}_3$ -based alloys and p-type  $\text{Bi}_{0.4}\text{Sb}_{1.6}\text{Te}_3$  and  $\text{CeFe}_{3.5}\text{Co}_{0.5}\text{Sb}_{12}$ -based alloys, and tested at the Jet Propulsion Laboratory (JPL) at hot and cold junction temperatures of  $\sim 305$  K and 885 K, respectively. The calculations helped determine not only the side heat losses in these tests and the performance parameters of the STUs, but also the spatial dissipation of the heat losses from the various sides of and of the 3-D temperature fields in the n- and p-legs. The estimated values of the total side heat losses in uni8 and uni12 are  $3.7 W_{\text{th}}$  and  $1.83 W_{\text{th}}$ , respectively, and of the total contact resistance per leg are 146 and  $690 \mu\Omega\text{-cm}^2$ , respectively. The predicted peak conversion efficiencies for uni8 and uni12 in these tests are 4.55% and 5.65%, respectively, compared to 11.46% and 9.09%, which could be attainable with zero side heat losses, for the same total contact resistance per leg. The latter efficiencies are 2-3 percentage points lower than would be expected when used in space nuclear reactor power systems, in which side heat losses will be minimal and the contact resistances per leg could be as low as  $50 \mu\Omega\text{-cm}^2$ .

#### 3.1 Introduction

Thermoelectric devices are being used in many industrial, aerospace, medical, recreation, and auto applications for reliable and static conversion of heat to electricity at a variety of heat source temperatures from 400 K – 1300 K (Goldsmid 1986, Bennett 1994, Huber et al. 1999, Caillat et al. 2000, and Huber and Constant 2001). The performance of thermoelectric devices depend on the values of the hot and cold junction temperatures and the Figure-of-Merit,  $ZT$ , of the thermoelectric materials (Figure 2-1). For given dimensions and hot and cold junction

temperatures, the thermoelectric materials with the higher  $ZT$  give higher conversion efficiencies. Since there are no single thermoelectric materials with a high  $ZT$  over a wide range of temperatures, Segmented Thermoelectric Unicouples (STUs), in which the n- and p-legs are each comprised of several segments of different thermoelectric materials, are being developed to achieve higher conversion efficiency, not attainable with single thermoelectric material in n- and p-legs.

Recently, the skutterudites alloy developed at the Jet Propulsion Laboratory (JPL) in Pasadena California, have  $ZT$  values ranging from  $\sim 0.92$  to as much as 1.48, in the temperature range from 300 K to 973 K (Smith and Wolfe 1962, Caillat et al. 1997 and 1999, and Fleurial et al. 1997). In addition, a number of skutterudites-based STUs have been fabricated using p-type  $\text{CeFe}_{3.5}\text{Co}_{0.5}\text{Sb}_{12}$  and  $\text{Bi}_{0.4}\text{Sb}_{1.6}\text{Te}_3$ -based alloys, and n-type  $\text{CoSb}_3$  and  $\text{Bi}_2\text{Te}_{2.95}\text{Se}_{0.05}$ -based alloys, and tested at a cold junction temperature of 300 K and a hot junction temperature up to 973 K, with a demonstrated conversion efficiency of  $\sim 10\%$  and the potential of achieving up to 14-15% for an optimal configuration (Caillat et al. 2000 and 2001). Such a potential has been demonstrated recently in a performance test conducted at the University of New Mexico's Institute for Space and Nuclear Power Studies (El-Genk et al. 2004). The results are presented in chapter 5.

Additional new thermoelectric materials with  $ZT$  values higher than that for SiGe and suitable for operation between 973 K and up to 1273 K are being developed at JPL to eventually form the top segment of the STUs for use in space nuclear reactor power systems and in Advanced Radioisotope Power Systems (ARPSs). The resulting STUs will have 2-3 segments in the n-leg and 3-4 segments in the p-leg, and could operate between a hot junction temperature of 1173 – 1273 K and a cold junction temperature of 300 – 573 K, at a projected maximum conversion efficiency of  $\sim 17\%$ . For higher cold junction temperature of 700 K, this efficiency will reduce to  $\sim 8\% - 9\%$ .

The University of New Mexico's Institute for Space and Nuclear Power Studies (ISNPS) and JPL have studied the development of a high power density ARPS for potential use in NASA's future space and planetary exploration missions under this three-year grant sponsored by the NASA Cross-Enterprise Development Program. The ARPSs to be developed in chapter 5 use skutterudites-based segmented unicouples (Caillat et al. 1997, 1999, 2000 and 2001, and Fleurial et al. 1997) that are cascaded with SiGe unicouples. In addition, this joint effort included

conducting performance tests and modeling and optimization of STUs. As a part of this ISNPS/JPL joint effort, a 1-D analytical model (see chapter 2) and a 3-D model of STUs, which is described in this chapter, have been developed and their predictions compared with some of the test data generated for skutterudites-based STUs. In addition, these models are being used to help improve the testing arrangement in the experiments and optimize the dimensions and the selection of the interfacial temperatures of the segments of various materials in the n- and p-legs and of sublimation suppression coatings.

In this chapter, the developed three-dimensional model of STUs is described. The model predictions are compared with experimental data of two skutterudites-based STUs, uni8 and uni12, which are comprised of n-type  $\text{Bi}_2\text{Te}_{2.95}\text{Se}_{0.05}$  and  $\text{CoSb}_3$ -based alloys and p-type  $\text{Bi}_{0.4}\text{Sb}_{1.6}\text{Te}_3$  and  $\text{CeFe}_{3.5}\text{Co}_{0.5}\text{Sb}_{12}$ -based alloys. These STUs have been tested between hot and cold junction temperatures of  $\sim 305$  K and 885 K, respectively. The obtained 3-D calculations are not only of the side heat losses in these tests and their effect on the performance parameters of STUs, but also of the spatial distributions of these losses and of the 3-D temperature fields in the n- and p-legs. Model predictions are validated using those of the 1-D analytical model detailed in chapter 2, for zero side heat losses and same contact resistance per leg.

### 3.2 Model Description

Determining the 3-D temperature fields in the n- and p-legs and the spatial distribution of the side heat losses from the legs are important for improving the setup of the performance tests and for confirming the theoretical potential of the skutterudites-based STUs. The calculated temperature fields are also important for performing subsequent thermal stress analyses of the n- and p-legs, which are subjected to a large linear temperature gradient of up to hundreds of degrees per mm. In addition, 3-D thermal calculations for these STUs would aid in optimizing the selection of the type and thickness of potential coatings to suppress material sublimation in the n- and p-legs, near the hot shoe. The hot junction temperature at which the STUs are tested at JPL is up to 973 K.

The 3-dimensional energy equations of the various segments in the n- and p-legs, including Joule and Thomson heating, are solved numerically, subject to the prescribed boundary conditions at the various sides of the STU. In these equations, all physical and thermoelectric

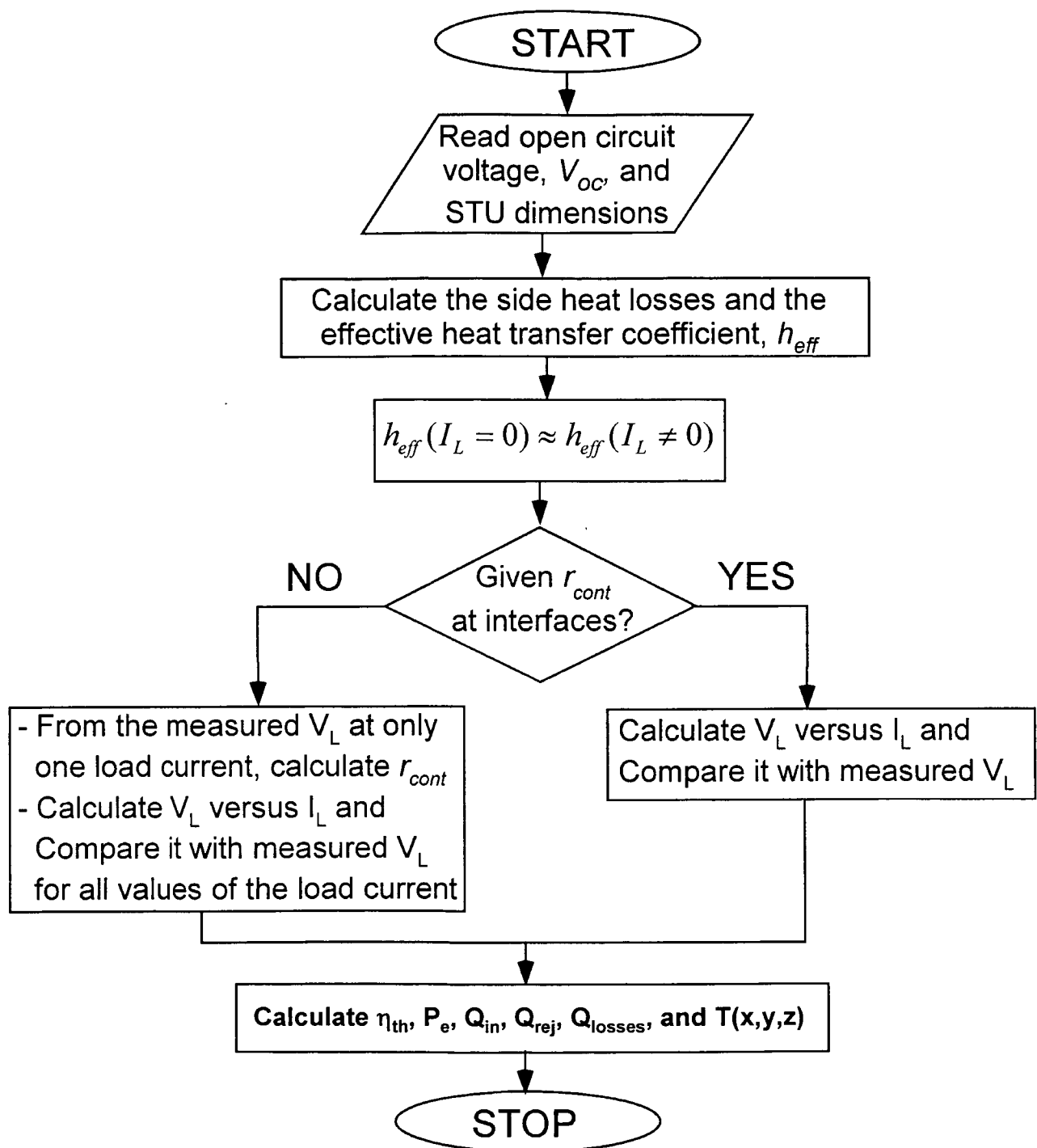


Figure 3-1 Flow Diagram of Evaluating Side Heat Losses from STUs in Performance Tests.



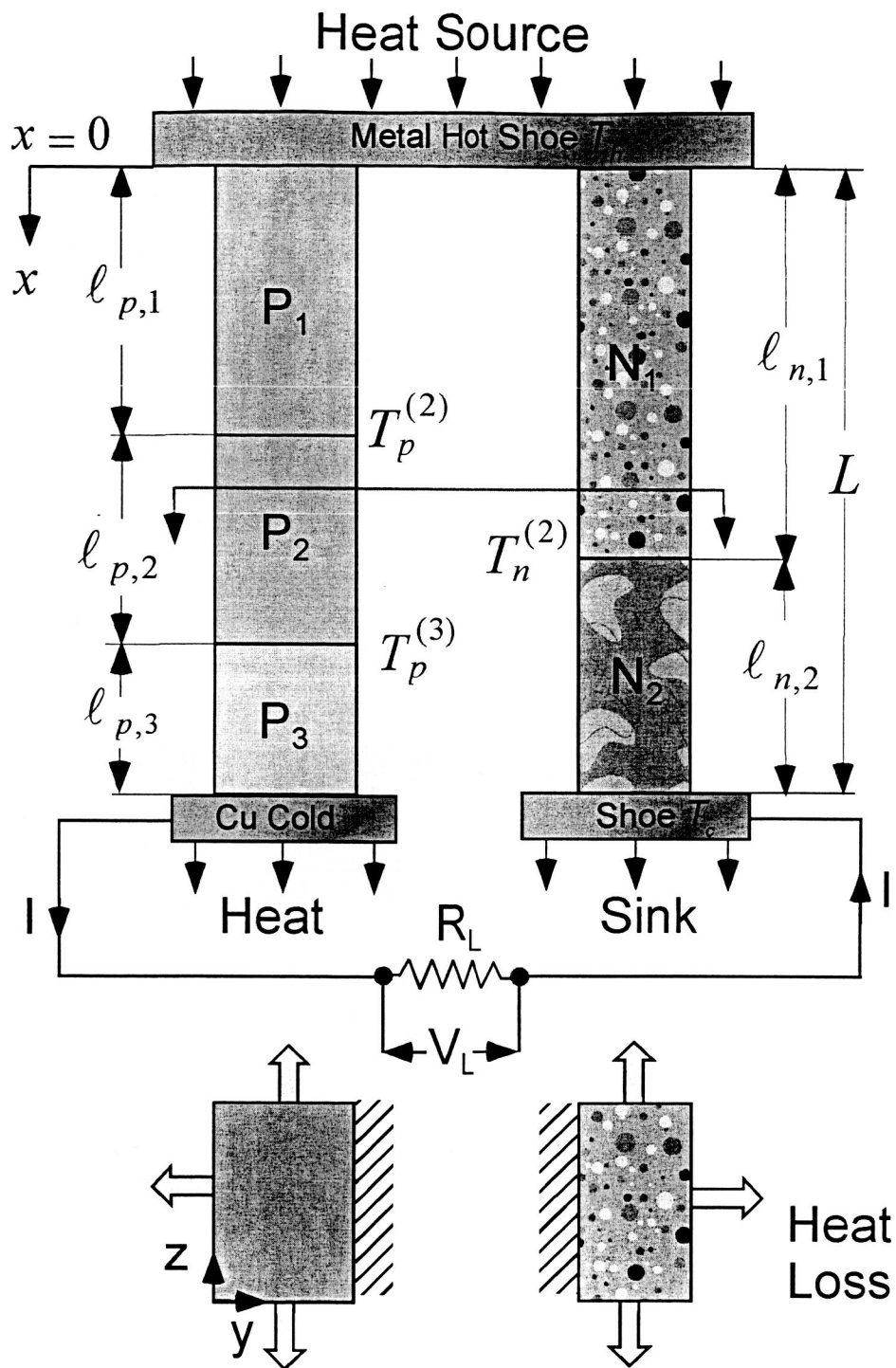


Figure 3-2 A Schematic of a STU.

properties of the material in each segment are treated as temperature dependent. These properties, which include thermal conductivity, electrical resistivity, and Seebeck and Thomson coefficients, could be either isotropic or orthotropic.

The heat losses from the STU in the 3-D model to the ambient in performance test could be either by radiation or convection, or by both radiation and convection. Calculating the radiation heat losses, however, require knowledge of the surface emissivity of all segments in the n- and p-legs as a function of temperature as well as the gas pressure surrounding the STU in performance tests. Basically, accurate measurement of the heat losses from the STU is extremely difficult. On the other hand, measuring the electric load voltage could be done accurately. The electrical load voltage,  $V_L$ , and the corresponding electrical power,  $P_e$ , are given as:

$$V_L = V_{oc} - I_L (R_{int} + R_{cont}), \text{ and} \quad (3-1a)$$

$$P_e = V_{oc} I_L - I_L^2 (R_{int} + R_{cont}). \quad (3-1b)$$

From Eq. (3-1a), the open circuit voltage at  $I = 0$ ,  $V_{oc}$ , equals  $V_L$ , which depends on the Seebeck coefficients and hence the temperature distributions within all the segments of the STU (chapter 2). Since, the temperature distribution in the STU is directly affected by the amount of heat losses from the sides, the measured open circuit voltage,  $V_{oc}$ , could be used to accurately estimate the amount of heat losses from the STU and hence the effective or equivalent heat transfer coefficient. In addition, assuming the effective heat transfer coefficient to be independent of the load electrical current,  $I_L$ , the electrical load voltage,  $V_L$ , can be determined as a function of the load current, when the sum of the contact resistances,  $R_{cont}$ , at all interfaces are measured. However, when the contact resistances at all interfaces are not measured, they could be calculated by knowing the measured electrical load voltage at only one electrical load current. A schematic of flow diagram illustrating the procedure of evaluating the heat losses from the STU using the 3-D model, in conjunction with experimental measurements is shown in Figure 3-1.

When the legs of the STU are perfectly insulated, the analytical solution of the one-dimensional energy equations accurately obtains the axial temperature distributions and predicts the performance parameters, including the electrical current, load voltage, interfacial temperatures, electrical power and input and rejected thermal powers (chapter 2). However, since the surface area to volume ratios of the n- and p-legs, are relatively large (Figure 3-2), the

side heat losses could be large, affecting the temperature distributions within the n- and p-legs and, hence, the performance parameters of the STUs in the tests. In this case, these parameters could not be accurately predicted using the one-dimensional STU model described in chapter 2, but estimated using the 3-D model described in this chapter.

### 3.2.1 Governing Equation

The general, 3-D heat conduction equation in the segments in the n- and p-legs of a STU (Figure 3-2) can be written as:

$$\begin{aligned} \omega C_p \frac{\partial T}{\partial t} = & \frac{\partial}{\partial x} \left( k_x(T) \frac{\partial T}{\partial x} \right) + \frac{\partial}{\partial y} \left( k_y(T) \frac{\partial T}{\partial y} \right) + \frac{\partial}{\partial z} \left( k_z(T) \frac{\partial T}{\partial z} \right) - \tau_x(T) J_x \frac{\partial T}{\partial x} - \\ & \tau_y(T) J_y \frac{\partial T}{\partial y} - \tau_z(T) J_z \frac{\partial T}{\partial z} + \rho_x(T) J_x^2 + \rho_y(T) J_y^2 + \rho_z(T) J_z^2, \end{aligned} \quad (3-2a)$$

where,

$$T = \hat{T} \text{ on } \Gamma_T, \text{ and } \left( -k_x \frac{\partial T}{\partial x} n_x - k_y \frac{\partial T}{\partial y} n_y - k_z \frac{\partial T}{\partial z} n_z \right) = \hat{q} \text{ on } \Gamma_q. \quad (3-2b)$$

In Eq. (3-2a),  $J_x$ ,  $J_y$ , and  $J_z$  are the electrical current densities in x-, y-, and z-directions, respectively, which equal zero at the open circuit condition. Note that, the electrical current flows *only* in the direction perpendicular to the cross-section area of the n- and p-legs of the STU, thus is non-zero, but the other two components must be zero. For example, at the closed circuit condition, if the cross-section areas of the p- and n-legs are in the x-z plane, then  $J_x = 0$ ,  $J_y \neq 0$ , and  $J_z = 0$ . In Eq. (3-2a), the physical properties are treated as temperature dependent and either isotropic or orthotropic.

As indicated in Eq. (3-2b),  $\hat{T}$  and  $\hat{q}$  are specified functions of position on the portions  $\Gamma_T$  and  $\Gamma_q$ , respectively, of the total surface  $\Gamma$  of the STU.  $\Gamma_T$  is a portion from the total surface,  $\Gamma$ , on which the temperature boundary conditions are specified and  $\Gamma_q$  is another portion from the total surface,  $\Gamma$ , on which the heat flux, convection, and/or radiation boundary conditions are specified. The sum of the two portions of the surface  $\Gamma_T$  and  $\Gamma_q$  equals the total surface of the STU,  $\Gamma$ . Therefore, the present model handles different types of boundary conditions at different portions of the STU surface.

The domain of each segment of the STU is discretized by three-dimensional elements,  $\Omega^e$ , as prism or tetrahedral elements. A major disadvantage associated with using prism elements is that they do not conform well to curved boundaries. However, the tetrahedral elements used in developing the present 3-D STU model (Figure 3-3) are better suited to approximate curved boundaries with a minimum discretizing error. As shown in Figure 3-3, four nodes and four faces define a tetrahedral element, and each face of the element is represented by a triangle.

The symmetric weak form (variational formulation) of Eqs. (3-2a) and (3-2b) over the domain of a tetrahedral element,  $\Omega^e$ , is obtained upon multiplying both sides of Eq. (3-2a) by a test function  $v$  and integrating both sides over the volume of the element, which yields:

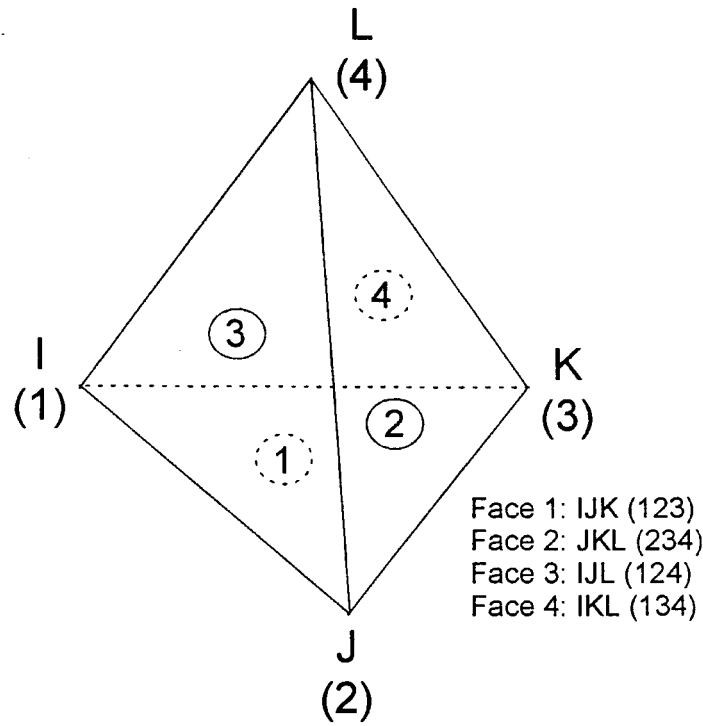


Figure 3-3 A Schematic of Three-Dimensional Tetrahedral Element.

$$\int_{\Omega^e} \left( v \omega C_p T + k_x \frac{\partial T}{\partial x} \frac{\partial v}{\partial x} + k_y \frac{\partial T}{\partial y} \frac{\partial v}{\partial y} + k_z \frac{\partial T}{\partial z} \frac{\partial v}{\partial z} + v \tau_x(T) J_x \frac{\partial T}{\partial x} + v \tau_y(T) J_y \frac{\partial T}{\partial y} + v \tau_z(T) J_z \frac{\partial T}{\partial z} - v (\rho_x(T) J_x^2 + \rho_y(T) J_y^2 + \rho_z(T) J_z^2) \right) dx dy dz + \oint_{\Gamma^e} v q ds = 0. \quad (3-3)$$

The last term on the left hand side of Eq. (3-3) is the contribution from flux, convective, or radiative boundary conditions to the element matrices and vectors for all boundary elements that

see the surfaces of the legs of the STU as detailed next. This contribution, however, is zero for all non-boundary elements.  $\Gamma^e$  in Eq. (3-3) is the face of the tetrahedral element (see Figure 3-3) on it flux, convective, or radiative boundary condition is specified.

### 3.2.2 Element Vectors and Matrices

In this subsection, the nodal basis functions of the tetrahedral element and the different boundary conditions are applied into Eq. (3-3) to obtain all element matrices and vectors, including: (a) the mass or the damping matrix, (b) the conductivity matrix, and (c) the forcing vectors. The legs of the STU are meshed by tetrahedral elements using the meshing capabilities in ANSYS. The different boundary conditions on the surfaces of the legs of the STU are transferred to the corresponding surfaces of the boundary elements (*i.e.* the elements that see the surfaces of the legs of the STU). The contributions of different boundary condition to the matrices and vectors of the boundary elements are explained in details in next two subsections. Over the domain of the element,  $\Omega^e$ , the temperature,  $T$ , is represented using linear function in  $x, y$  and  $z$  as:

$$T = C_1 + C_2x + C_3y + C_4z. \quad (3-4)$$

Considering the nodal temperatures (*i.e.* the temperature at each node of the element, see Figure 3-3), Eq. (3-4) must satisfy the following conditions:

$$\begin{aligned} T &= T_I \quad \text{at } x = x_I, \quad y = y_I, \quad \text{and } z = z_I, \\ T &= T_J \quad \text{at } x = x_J, \quad y = y_J, \quad \text{and } z = z_J, \\ T &= T_K \quad \text{at } x = x_K, \quad y = y_K, \quad \text{and } z = z_K, \quad \text{and} \\ T &= T_L \quad \text{at } x = x_L, \quad y = y_L, \quad \text{and } z = z_L. \end{aligned} \quad (3-5)$$

Substituting from Eq. (3-5) into Eq. (3-4) results in four equations in four unknowns ( $C_1, C_2, C_3$ , and  $C_4$ ). Solving for these unknowns and substituting back into Eq. (3-4), and regrouping the parameters gives:

$$T = T_I \Psi_1(x, y, z) + T_J \Psi_2(x, y, z) + T_K \Psi_3(x, y, z) + T_L \Psi_4(x, y, z), \quad (3-6)$$

where,  $\Psi_j$  ( $j = 1 - 4$ ) are the nodal basis functions (or shape functions) of the tetrahedral element, which are given as:

$$\begin{Bmatrix} \Psi_1 \\ \Psi_2 \\ \Psi_3 \\ \Psi_4 \end{Bmatrix} = \frac{1}{6V^e} \begin{Bmatrix} a_1 + b_1x + c_1y + d_1z \\ a_2 + b_2x + c_2y + d_2z \\ a_3 + b_3x + c_3y + d_3z \\ a_4 + b_4x + c_4y + d_4z \end{Bmatrix}. \quad (3-7)$$

In Eq. (3-7), the volume of the tetrahedral element,  $V^e$ , is computed from the following equation:

$$V^e = \left(\frac{1}{6}\right) \begin{vmatrix} x_I & y_I & z_I & 1 \\ x_J & y_J & z_J & 1 \\ x_K & y_K & z_K & 1 \\ x_L & y_L & z_L & 1 \end{vmatrix}. \quad (3-8)$$

The terms  $a_1, b_1, c_1, d_1, \dots$ , and  $a_4, b_4, c_4, d_4$  in Eq. (3-7) are given, respectively, as:

$$\begin{aligned} a_1 &= - \begin{vmatrix} x_J & y_J & z_J \\ x_K & y_K & z_K \\ x_L & y_L & z_L \end{vmatrix}, \quad b_1 = \begin{vmatrix} y_J & z_J & 1 \\ y_K & z_K & 1 \\ y_L & z_L & 1 \end{vmatrix}, \quad c_1 = - \begin{vmatrix} x_J & z_J & 1 \\ x_K & z_K & 1 \\ x_L & z_L & 1 \end{vmatrix}, \quad d_1 = \begin{vmatrix} x_J & y_J & 1 \\ x_K & y_K & 1 \\ x_L & y_L & 1 \end{vmatrix}, \\ a_2 &= - \begin{vmatrix} x_K & y_K & z_K \\ x_I & y_I & z_I \\ x_L & y_L & z_L \end{vmatrix}, \quad b_2 = \begin{vmatrix} y_K & z_K & 1 \\ y_I & z_I & 1 \\ y_L & z_L & 1 \end{vmatrix}, \quad c_2 = - \begin{vmatrix} x_K & z_K & 1 \\ x_I & z_I & 1 \\ x_L & z_L & 1 \end{vmatrix}, \quad d_2 = \begin{vmatrix} x_K & y_K & 1 \\ x_I & y_I & 1 \\ x_L & y_L & 1 \end{vmatrix}, \\ a_3 &= - \begin{vmatrix} x_L & y_L & z_L \\ x_I & y_I & z_I \\ x_J & y_J & z_J \end{vmatrix}, \quad b_3 = \begin{vmatrix} y_L & z_L & 1 \\ y_I & z_I & 1 \\ y_J & z_J & 1 \end{vmatrix}, \quad c_3 = - \begin{vmatrix} x_L & z_L & 1 \\ x_I & z_I & 1 \\ x_J & z_J & 1 \end{vmatrix}, \quad d_3 = \begin{vmatrix} x_L & y_L & 1 \\ x_I & y_I & 1 \\ x_J & y_J & 1 \end{vmatrix}, \\ a_4 &= - \begin{vmatrix} x_J & y_J & z_J \\ x_I & y_I & z_I \\ x_K & y_K & z_K \end{vmatrix}, \quad b_4 = \begin{vmatrix} y_J & z_J & 1 \\ y_I & z_I & 1 \\ y_K & z_K & 1 \end{vmatrix}, \quad c_4 = - \begin{vmatrix} x_J & z_J & 1 \\ x_I & z_I & 1 \\ x_K & z_K & 1 \end{vmatrix}, \quad d_4 = \begin{vmatrix} x_J & y_J & 1 \\ x_I & y_I & 1 \\ x_K & y_K & 1 \end{vmatrix}. \end{aligned} \quad (3-9)$$

Substituting the test function  $v$  equal  $\Psi_i$ , and Eq. (3-6) into Eq. (3-3), the variational formulation over the domain of the element becomes:

$$[C]^e \{F\}^e + [K]^e \{T\}^e = \{F\}^e, \quad (3-10)$$

where  $[C]^e$  is the element damping (or mass) matrix. The element conductivity matrix,  $[K]^e$ , and element forcing vector,  $\{F\}^e$  are given, respectively, as:

$$[K]^e = [KF]^e + [KT]^e + [KL]^e, \text{ and} \quad (3-11a)$$

$$\{F\}^e = \{FJ\}^e + \{FQ\}^e + \{FL\}^e. \quad (3-11b)$$

The contributions to the element conductivity matrix,  $[K]^e$ , due to Fourier effect, Thomson heating, and the heat losses either by convection or/and radiation from the sides of the n- and p-legs are represented by the matrices  $[KF]^e$ ,  $[KT]^e$ , and  $[KL]^e$ , respectively (Eq. 3-11a). While, the contributions to the element forcing vector,  $\{F\}^e$ , due to Joule heating, heat flux boundary conditions, and the heat losses either by convection or radiation, are represented by the vectors  $\{FJ\}^e$ ,  $\{FQ\}^e$ , and  $\{FL\}^e$ , respectively (Eq. 3-11b). Note that if the element is not a boundary element (*i.e.* the element does not see one of the side surfaces of the STU), the contributions of both heat flux boundary condition for when the input heat flux or rejected heat flux is specified rather than hot junction temperature or cold junction temperature, respectively, and heat losses either by convection or/and radiation to both the element conductivity matrix,  $[K]^e$ , and forcing vector,  $\{F\}^e$ , must be zero as will be discussed in detail later.

The element damping matrix, conductivity matrix and the forcing vector, respectively, are given as:

$$[C]^e = \begin{bmatrix} C_{11} & C_{12} & \dots & C_{14} \\ C_{21} & C_{22} & \dots & \dots \\ \dots & \dots & \dots & \dots \\ C_{41} & \dots & \dots & C_{44} \end{bmatrix}, \quad (3-12a)$$

$$[K]^e = \begin{bmatrix} KF_{11} + KT_{11} + KL_{11} & KF_{12} + KT_{12} + KL_{12} & \dots & KF_{14} + KT_{14} + KL_{14} \\ KF_{21} + KT_{21} + KL_{21} & KF_{22} + KT_{22} + KL_{22} & \dots & \dots \\ \dots & \dots & \dots & \dots \\ KF_{41} + KT_{41} + KL_{41} & \dots & \dots & KF_{44} + KT_{44} + KL_{44} \end{bmatrix}, \text{ and} \quad (3-12b)$$

$$\{F\}^e = \begin{Bmatrix} FJ_1 + FQ_1 + FL_1 \\ FJ_2 + FQ_2 + FL_2 \\ \dots \\ FJ_4 + FQ_4 + FL_4 \end{Bmatrix}. \quad (3-12c)$$

The components of the element mass and conductivity matrixes and the forcing vector given in Eq. (3-12) are obtained as:

$$C_{ij} = \int_{\Omega^e} [\omega^e C p^e \Psi_i \Psi_j] dx dy dz, \quad (3-13a)$$

$$KF_{ij} = \int_{\Omega^e} \left( k_x^e \left( \frac{\partial \Psi_i}{\partial x} \right) \left( \frac{\partial \Psi_j}{\partial x} \right) + k_y^e \left( \frac{\partial \Psi_i}{\partial y} \right) \left( \frac{\partial \Psi_j}{\partial y} \right) + k_z^e \left( \frac{\partial \Psi_i}{\partial z} \right) \left( \frac{\partial \Psi_j}{\partial z} \right) \right) dx dy dz, \quad (3-13b)$$

$$KT_{ij} = \int_{\Omega^e} \left( \tau_x^e J_x \Psi_i \left( \frac{\partial \Psi_j}{\partial x} \right) + \tau_y^e J_y \Psi_i \left( \frac{\partial \Psi_j}{\partial y} \right) + \tau_z^e J_z \Psi_i \left( \frac{\partial \Psi_j}{\partial z} \right) \right) dx dy dz, \quad (3-13c)$$

$$FJ_i = \int_{\Omega^e} (\rho_x^e J_x^2 \Psi_i + \rho_y^e J_y^2 \Psi_i + \rho_z^e J_z^2 \Psi_i) dx dy dz. \quad (3-13d)$$

Since the physical properties of TE materials in the segments of the n- and p-legs of the STU are temperature dependant, therefore, for each computational element, the material physical properties in Eq. (3-13) are evaluated at the mean temperature of the element. Upon substituting from Eq. (3-7) into Eq. (3-13) gives the following matrices in Eqs. (3-10) and (3-11) as follows:

$$[C]^e = \frac{\omega^e C p^e V^e}{10} \begin{bmatrix} 2 & 1 & 1 & 1 \\ 1 & 2 & 1 & 1 \\ 1 & 1 & 2 & 1 \\ 1 & 1 & 1 & 2 \end{bmatrix}, \quad (3-14a)$$

$$[KF]^e = \frac{k_x^e}{36 V^e} \begin{bmatrix} b_1^2 & b_1 b_2 & b_1 b_3 & b_1 b_4 \\ b_1 b_2 & b_2^2 & b_2 b_3 & b_2 b_4 \\ b_1 b_3 & b_2 b_3 & b_3^2 & b_3 b_4 \\ b_1 b_4 & b_2 b_4 & b_3 b_4 & b_4^2 \end{bmatrix} + \frac{k_y^e}{36 V^e} \begin{bmatrix} c_1^2 & c_1 c_2 & c_1 c_3 & c_1 c_4 \\ c_1 c_2 & c_2^2 & c_2 c_3 & c_2 c_4 \\ c_1 c_3 & c_2 c_3 & c_3^2 & c_3 c_4 \\ c_1 c_4 & c_2 c_4 & c_3 c_4 & c_4^2 \end{bmatrix} + \frac{k_z^e}{36 V^e} \begin{bmatrix} d_1^2 & d_1 d_2 & d_1 d_3 & d_1 d_4 \\ d_1 d_2 & d_2^2 & d_2 d_3 & d_2 d_4 \\ d_1 d_3 & d_2 d_3 & d_3^2 & d_3 d_4 \\ d_1 d_4 & d_2 d_4 & d_3 d_4 & d_4^2 \end{bmatrix}, \quad (3-14b)$$



$$\begin{aligned}
[KT]^e = & \frac{\tau_x^e J_x}{24 V^e} \begin{bmatrix} b_1 & b_2 & b_3 & b_4 \\ b_1 & b_2 & b_3 & b_4 \\ b_1 & b_2 & b_3 & b_4 \\ b_1 & b_2 & b_3 & b_4 \end{bmatrix} + \frac{\tau_y^e J_y}{24 V^e} \begin{bmatrix} c_1 & c_2 & c_3 & c_4 \\ c_1 & c_2 & c_3 & c_4 \\ c_1 & c_2 & c_3 & c_4 \\ c_1 & c_2 & c_3 & c_4 \end{bmatrix} \\
& + \frac{\tau_z^e J_z}{24 V^e} \begin{bmatrix} d_1 & d_2 & d_3 & d_4 \\ d_1 & d_2 & d_3 & d_4 \\ d_1 & d_2 & d_3 & d_4 \\ d_1 & d_2 & d_3 & d_4 \end{bmatrix}, \text{ and}
\end{aligned} \tag{3-14c}$$

$$\{FJ\}^e = \frac{V^e}{4} \left( \rho_x^e J_x^2 + \rho_y^e J_y^2 + \rho_z^e J_z^2 \right) \begin{Bmatrix} 1 \\ 1 \\ 1 \\ 1 \end{Bmatrix}. \tag{3-14d}$$

In the next subsections, the contributions to the element conductivity matrix and element forcing vector due to different boundary conditions are discussed.

### 3.2.3 Heat Flux Boundary Condition

The heat flux boundary condition is the case when the applied heat flux from the heater or the heat source at the hot junction of the STU is specified. In this case, the hot junction temperature,  $T_h$ , is not required for solving for the temperature field within the STU, but it is part of the results of the computations. Having one face (or more) of the computational elements (see Figure 3-3) subject to a heat flux boundary condition normal to the element face will contribute to the element forcing vector. This contribution is given as:

$$\begin{aligned}
FQ_i = & - \oint_{\Gamma^{(e)}} \Psi_i q_{nx} n_x ds - \oint_{\Gamma^{(e)}} \Psi_i q_{ny} n_y ds - \oint_{\Gamma^{(e)}} \Psi_i q_{nz} n_z ds = - \oint_{\Gamma^{(e)}} \Psi_i (\vec{q}_n \cdot \vec{n}) ds \\
= & - \int_{p=0}^{p=1} \int_{u=0}^{u=1-p} \Psi_i (\vec{q}_n \cdot \vec{N}) du dp,
\end{aligned} \tag{3-15a}$$

where,

$$\begin{aligned}
\vec{q}_n = & q_{nx} \vec{i} + q_{ny} \vec{j} + q_{nz} \vec{k}, \quad q_{nx} = \frac{N_x}{|\vec{N}|} q_n, q_{ny} = \frac{N_y}{|\vec{N}|} q_n, q_{nz} = \frac{N_z}{|\vec{N}|} q_n, \\
\vec{N} = & N_x \vec{i} + N_y \vec{j} + N_z \vec{k}, \text{ and } |\vec{N}| = \sqrt{N_x^2 + N_y^2 + N_z^2}.
\end{aligned} \tag{3-15b}$$

Substituting Eqs. (3-7) and (3-15b) into Eq. (3-15a), gives the contribution to element forcing vector as:

$$FQ_i = \begin{Bmatrix} FQ_1 \\ FQ_2 \\ FQ_3 \\ FQ_4 \end{Bmatrix} = -q_n \left| \vec{N} \right| \int_{p=0}^1 \int_{u=0}^{1-p} \Psi_i du dp = -\frac{q_n \left| \vec{N} \right|}{6V^e} \left[ \frac{1}{2} \gamma_{i1} + \frac{1}{6} \gamma_{i2} + \frac{1}{6} \gamma_{i3} \right]. \quad (3-16)$$

Note that the values of the parameters  $\gamma_{i1}$ ,  $\gamma_{i2}$ , and  $\gamma_{i3}$  ( $i = 1, \dots, 4$ ) and  $N_x$ ,  $N_y$ , and  $N_z$  depend on which face of the tetrahedral computational element is subject to heat flux boundary condition. When face one (Figure 3-3) is subject to heat flux boundary condition ( $q_n$  is replaced by  $q_{n1}$  in Eq. 3-16), the values of these parameters are listed as:

$$\begin{aligned} \gamma_{i1} &= a_i + b_i x_1 + c_i y_1 + d_i z_1, \\ \gamma_{i2} &= b_i (x_2 - x_1) + c_i (y_2 - y_1) + d_i (z_2 - z_1), \\ \gamma_{i3} &= b_i (x_3 - x_1) + c_i (y_3 - y_1) + d_i (z_3 - z_1), \end{aligned} \quad (3-17a)$$

and,

$$\begin{aligned} N_x &= (y_2 - y_1)(z_3 - z_1) - (y_3 - y_1)(z_2 - z_1), \\ N_y &= (x_3 - x_1)(z_2 - z_1) - (x_2 - x_1)(z_3 - z_1), \\ N_z &= (x_2 - x_1)(y_3 - y_1) - (x_3 - x_1)(y_2 - y_1). \end{aligned} \quad (3-17b)$$

Similarly, when face two, three, or four of the tetrahedral computational element (see Figure 3-3) is subject to heat flux boundary condition,  $q_n$  in Eq. (3-16) is replaced by  $q_{n2}$ ,  $q_{n3}$ , or  $q_{n4}$ , respectively, and the values of the parameters  $\gamma_{i1}$ ,  $\gamma_{i2}$ , and  $\gamma_{i3}$  ( $i = 1, \dots, 4$ ) and  $N_x$ ,  $N_y$ , and  $N_z$ , respectively, are given as:

**(a) Face two (Figure 3-3) subject to heat flux boundary condition:**

$$\begin{aligned} \gamma_{i1} &= a_i + b_i x_2 + c_i y_2 + d_i z_2, \\ \gamma_{i2} &= b_i (x_3 - x_2) + c_i (y_3 - y_2) + d_i (z_3 - z_2), \\ \gamma_{i3} &= b_i (x_4 - x_2) + c_i (y_4 - y_2) + d_i (z_4 - z_2), \end{aligned} \quad (3-18a)$$

and,

$$\begin{aligned} N_x &= (y_3 - y_2)(z_4 - z_2) - (y_4 - y_2)(z_3 - z_2), \\ N_y &= (x_4 - x_2)(z_3 - z_2) - (x_3 - x_2)(z_4 - z_2), \\ N_z &= (x_3 - x_2)(y_4 - y_2) - (x_4 - x_2)(y_3 - y_2). \end{aligned} \quad (3-18b)$$

**(b) Face three (Figure 3-3) subject to heat flux boundary condition:**

$$\begin{aligned}
\gamma_{i1} &= a_i + b_i x_1 + c_i y_1 + d_i z_1, \\
\gamma_{i2} &= b_i(x_2 - x_1) + c_i(y_2 - y_1) + d_i(z_2 - z_1), \\
\gamma_{i3} &= b_i(x_4 - x_1) + c_i(y_4 - y_1) + d_i(z_4 - z_1),
\end{aligned} \tag{3-19a}$$

and,

$$\begin{aligned}
N_x &= (y_2 - y_1)(z_4 - z_1) - (y_4 - y_1)(z_2 - z_1), \\
N_y &= (x_4 - x_1)(z_2 - z_1) - (x_2 - x_1)(z_4 - z_1), \\
N_z &= (x_2 - x_1)(y_4 - y_1) - (x_4 - x_1)(y_2 - y_1).
\end{aligned} \tag{3-19b}$$

**(c) Face four (Figure 3-3) subject to heat flux boundary condition:**

$$\begin{aligned}
\gamma_{i1} &= a_i + b_i x_1 + c_i y_1 + d_i z_1, \\
\gamma_{i2} &= b_i(x_3 - x_1) + c_i(y_3 - y_1) + d_i(z_3 - z_1), \\
\gamma_{i3} &= b_i(x_4 - x_1) + c_i(y_4 - y_1) + d_i(z_4 - z_1),
\end{aligned} \tag{3-20a}$$

and,

$$\begin{aligned}
N_x &= (y_3 - y_1)(z_4 - z_1) - (y_4 - y_1)(z_3 - z_1), \\
N_y &= (x_4 - x_1)(z_3 - z_1) - (x_3 - x_1)(z_4 - z_1), \\
N_z &= (x_3 - x_1)(y_4 - y_1) - (x_4 - x_1)(y_3 - y_1).
\end{aligned} \tag{3-20b}$$

If more than one face of the tetrahedral element are subject to heat flux boundary conditions, the contributions to the element forcing vector equal to the sum of the contributions of each of these faces.

### 3.2.4 Convection/Radiation Boundary Condition

The convection or radiation boundary condition is the case when the STU experiences side heat losses either by convection ( $h = h_{conv}$ ), by radiation ( $h = h_{rad}$ ), or by both convection and radiation ( $h = h_{eff}$ ). It is also, the case when either the cold junction or the hot junction is cooled or heated, respectively, by convection or radiation. Having these types of boundary conditions on one face or more faces of the tetrahedral computational element (see Figure 3-3) contributes to the element conductivity matrix and to the element forcing vector as discussed below.

After substituting  $v = \Psi_i$ , the last term in Eq. (3-3) reduces to:

$$\oint_{\Gamma^e} \Psi_i q \, ds = \oint_{\Gamma^e} \Psi_i \left( -k_x \frac{\partial T}{\partial x} n_x \right) ds + \oint_{\Gamma^e} \Psi_i \left( -k_y \frac{\partial T}{\partial y} n_y \right) ds + \oint_{\Gamma^e} \Psi_i \left( -k_z \frac{\partial T}{\partial z} n_z \right) ds, \tag{3-21}$$

where,

$$-k_x \frac{\partial T}{\partial x} = q_{Loss} n_x, -k_y \frac{\partial T}{\partial y} = q_{Loss} n_y, -k_z \frac{\partial T}{\partial z} = q_{Loss} n_z, \text{ and } q_{Loss} = h(T - T_\infty). \quad (3-22)$$

Substituting Eq. (3-22) into Eq. (3-21) gives:

$$\oint_{\Gamma^e} \Psi_i q \, ds = \oint_{\Gamma^e} \Psi_i h T (\hat{n} \bullet \hat{n}) \, ds - \oint_{\Gamma^e} \Psi_i h T_\infty (\hat{n} \bullet \hat{n}) \, ds. \quad (3-23)$$

The first term on the right hand side of Eq. (3-23) is the contribution of heat losses by convection or radiation to the element's conductivity matrix. While the second term on the right hand side of this equation is the corresponding contribution to the element's forcing vector.

When face one (Figure 3-3) of the tetrahedral element is subject to a convective ( $h = h_1^e = h_{conv,1}^e$ ), radiative ( $h = h_1^e = h_{rad,1}^e$ ), or both convective and radiative boundary condition ( $h = h_1^e = h_{eff,1}^e$ ) the contribution to the element conductivity matrix is obtained upon substituting Eq. (3-6) into the first term on the right hand side of Eq. (3-23), which gives:

$$[KL]^{(e)} = \begin{bmatrix} KL_{11} & KL_{12} & \dots & KL_{14} \\ KL_{21} & KL_{22} & \dots & \dots \\ \dots & \dots & \dots & \dots \\ KL_{41} & \dots & \dots & KL_{44} \end{bmatrix}, \quad (3-24a)$$

where,

$$KL_{ij} = h_1^e |N| \int_{p=0}^{p=1} \int_{u=0}^{u=1-p} \Psi_i \Psi_j \, du \, dp. \quad (3-24b)$$

Substituting Eq. (3-7) into Eq. (3-24b) gives:

$$KL_{ij} = \frac{h_1^e |N|}{36 (V^e)^2} \begin{pmatrix} \gamma_{i1} \left( \frac{1}{2} \gamma_{j1} + \frac{1}{6} \gamma_{j2} + \frac{1}{6} \gamma_{j3} \right) + \\ \gamma_{i2} \left( \frac{1}{6} \gamma_{j1} + \frac{1}{12} \gamma_{j2} + \frac{1}{24} \gamma_{j3} \right) + \\ \gamma_{i3} \left( \frac{1}{6} \gamma_{j1} + \frac{1}{24} \gamma_{j2} + \frac{1}{12} \gamma_{j3} \right) \end{pmatrix}. \quad (3-25)$$

While, the contribution to the element's forcing vector (second term on the right hand side of Eq. 3-23) is obtained as:

$$\{FL\}^{(e)} = \begin{Bmatrix} FL_1 \\ FL_2 \\ \dots \\ FL_4 \end{Bmatrix}, \quad (3-26a)$$

where,

$$FL_i = h_1^e T_\infty \left| \bar{N} \right| \int_{p=0}^1 \int_{u=0}^{1-p} \Psi_i du dp. \quad (3-26b)$$

Substituting from Eq. (3-7) into Eq. (3-26b) gives:

$$FL_i = \frac{h_1^e T_\infty \left| \bar{N} \right|}{6V^e} \left[ \frac{1}{2} \gamma_{i1} + \frac{1}{6} \gamma_{i2} + \frac{1}{6} \gamma_{i3} \right]. \quad (3-27)$$

In Eqs. (3-25), and (3-27), the values of the parameters  $\gamma_{i1}$ ,  $\gamma_{i2}$ , and  $\gamma_{i3}$  ( $i = 1, \dots, 4$ ) and  $N_x$ ,  $N_y$ , and  $N_z$  are given, respectively, by Eq. (3-17a) and (3-17b).

When face two, face three, or face four of the tetrahedral element is subject to convective or radiative boundary condition, the contributions to both element conductivity matrix and forcing vector are given by Eq. (3-25) and Eq. (3-27), respectively, after replacing  $h_1^e$  by  $h_2^e$ ,  $h_1^e$  by  $h_3^e$ , or  $h_1^e$  by  $h_4^e$ , respectively. The values of the parameters  $\gamma_{i1}$ ,  $\gamma_{i2}$ , and  $\gamma_{i3}$ , and  $N_x$ ,  $N_y$ , and  $N_z$  are also given by Eq. (3-18), Eq. (3-19) or Eq. (3-20), respectively.

### 3.2.5 Global Vector and Matrices and Method of Solution

The element matrixes and vectors obtained above are used to assemble the global matrices and vector in the form:

$$[C]^G \{T\}^G + [K]^G \{T\}^G = \{F\}^G, \quad (3-28)$$

where,

$$[C]^G = \sum_{e=1}^{N_E} [C]^e, \quad [K]^G = \sum_{e=1}^{N_E} [K]^e, \quad \text{and} \quad \{F\}^G = \sum_{e=1}^{N_E} \{F\}^e, \quad \text{and} \quad (3-29)$$

$N_E$  in Eq. (3-29) is the total number of computational elements in the meshed legs of the STU. In Eq. (3-28),  $[C]^G$  is the global mass or damping matrix. For steady state operation, the first term on the left hand side of Eq. (3-28) is zero, which is the case of the present analyses. Both the global conductivity matrix,  $[K]^G$ , and the global forcing vector,  $\{F\}^G$ , in Eq. (3-28) account for the Fourier effect, Joule and Thomson heating, and the different type of the specified

boundary conditions, including temperature, heat flux, convective and radiative. Equation (3–28) represents a set of linear algebraic equations, which are solved for the temperature fields in the n- and p-legs of the STU,  $\{T\}^G$ , using Gauss-Jordan Method.

As indicated earlier, all properties of the materials of the STU are temperature dependent. In the first iteration, these properties are evaluated at local temperatures obtained from 1-D model detailed in chapter 2, where STU is assumed perfectly thermal insulated. Then Gauss-Jordan Method solves the set of the linear algebraic equations (Eq. 3–28) for the temperature field  $\{T\}^G$ . In the second iteration, the obtained temperature field  $\{T\}^G$  is used to update all materials properties and then solve the set of the linear algebraic equations (Eq. 3–28) again for the temperature field  $\{T\}^G$ . This procedure is repeated until the maximum difference in  $\{T\}^G$  between to successive iterations is  $\leq 10^{-3}$  K. The obtained temperature fields are used to evaluate all performance parameters of the STU as a function of the load current. These performance parameters are the load voltage, conversion efficiency, electrical power output and input and rejected thermal powers. In addition, the calculated side heat losses are those which correspond to when the calculated and measured  $V_{oc}$  are equal.

### 3.3 Incorporation of the STU Model in ANSYS Software

The 3-D model developed using the capabilities of the ANSYS commercial Software makes it possible to do thermal stress analyses and performance optimization studies. The development of the 3-D STU model is incorporated into ANSYS in two steps (see Figure 3-4):

- (1) A new computational element having a shape of tetrahedral is created. The name of this element is USER100. This new element is linked to ANSYS commercial Software to create a customized version of ANSYS that has this element in its database. This element is then used in the environment of the customized version of ANSYS to perform meshing, define the material properties of each element and obtaining the nodes number associated with each element and the three coordinates (x, y and z) of each node (Figure 3-4). This information is necessary for the next step.
- (2) An external subroutine that uses the information in the previous step is developed using the Finite Element Methodologies (FEM) detailed in the previous section. The output of this subroutine includes the temperature field in the legs of the STU, the I-V

characteristic curve, conversion efficiency, electrical power, and input and rejected thermal powers.

Comparing the predictions of the 3-D model with the 1-D analytical model detailed in chapter 2, with zero side heat losses, provide a benchmark of the 3-D model predictions. As detailed in next section, the calculated temperature fields in the legs of the STU, the I-V characteristic, conversion efficiency, and electrical power using the 3-D and the 1-D (chapter 2) models are in excellent agreement.

### 3.4 Verification of Model Predictions

The performance parameters of the uni12, tested at JPL, are calculated using the present 3-D model and compared with the predictions of 1-D analytical model detailed in chapter 2, for when the total contact resistance per leg of  $50 \mu\Omega\text{-cm}^2$  and there are no side heat losses. The uni12 is comprised of two segments in the p-leg and two segments in the n-leg. The materials and the dimensions of the various segments are listed in Figure 3-5. Figure 3-6a compares the predictions of the axial temperature distributions by the 3-D model (open and closed symbols) with those calculated by the 1-D analytical model (solid and dashed lines) for the n- and p-legs of uni12. The cold and hot junction temperatures in these calculations are 320 K and 868 K, respectively, and the total length of n- and p-legs is 14.535 mm.

As shown in Figure 3-6a, the predictions of the 3-D and the 1-D models are in excellent agreement for a load current of 6.1883 A. Figure 3-6b shows that the predictions of the 3-D model of the load voltage and electrical power of uni12 are also in excellent agreement with those of the 1-D analytical model. Figure 3-6c and Figure 3-6d show excellent agreement between the predictions of the conversion efficiency and the input and rejected thermal powers by the 3-D and the 1-D (chapter 2) models. Similar agreements are obtained when comparing the predictions of the 3-D and the 1-D models for uni8, whose composition and dimensions are also indicated in Figure 3-5.

### 3.5 Comparison with Test Data

Figure 3-7 and Figure 3-8 compare the predictions of the 3-D model with the experimental data for uni8 and uni12, respectively, tested in vacuum at JPL. The hot junction temperature of uni8 in the test decreased from 885 K at open circuit condition to 830 K at the highest load current of 7.3 A, while keeping the cold junction temperature constant at 305 K. The hot and

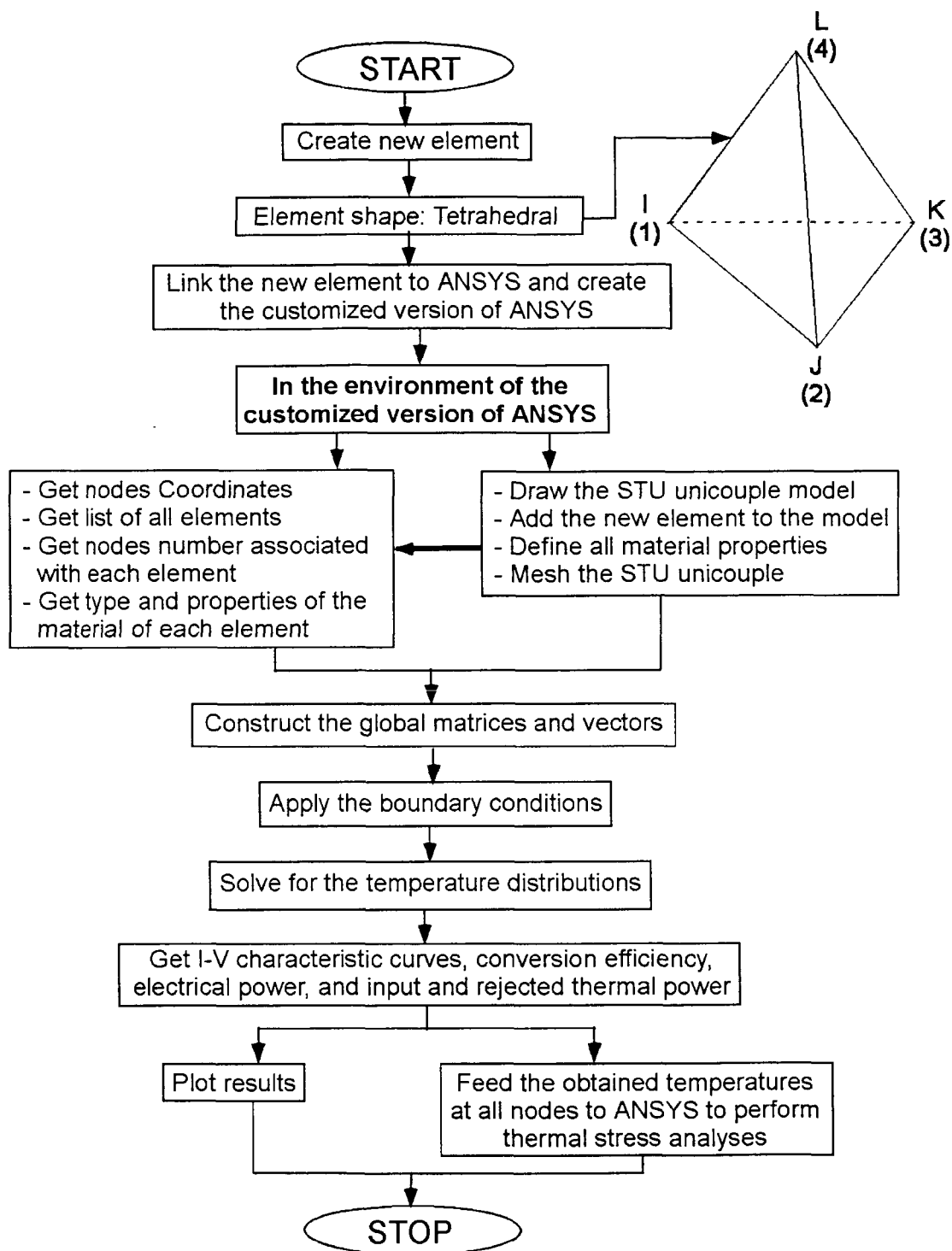


Figure 3-4 A Flow Diagram for Incorporating the 3-D Model of STU into ANSYS.



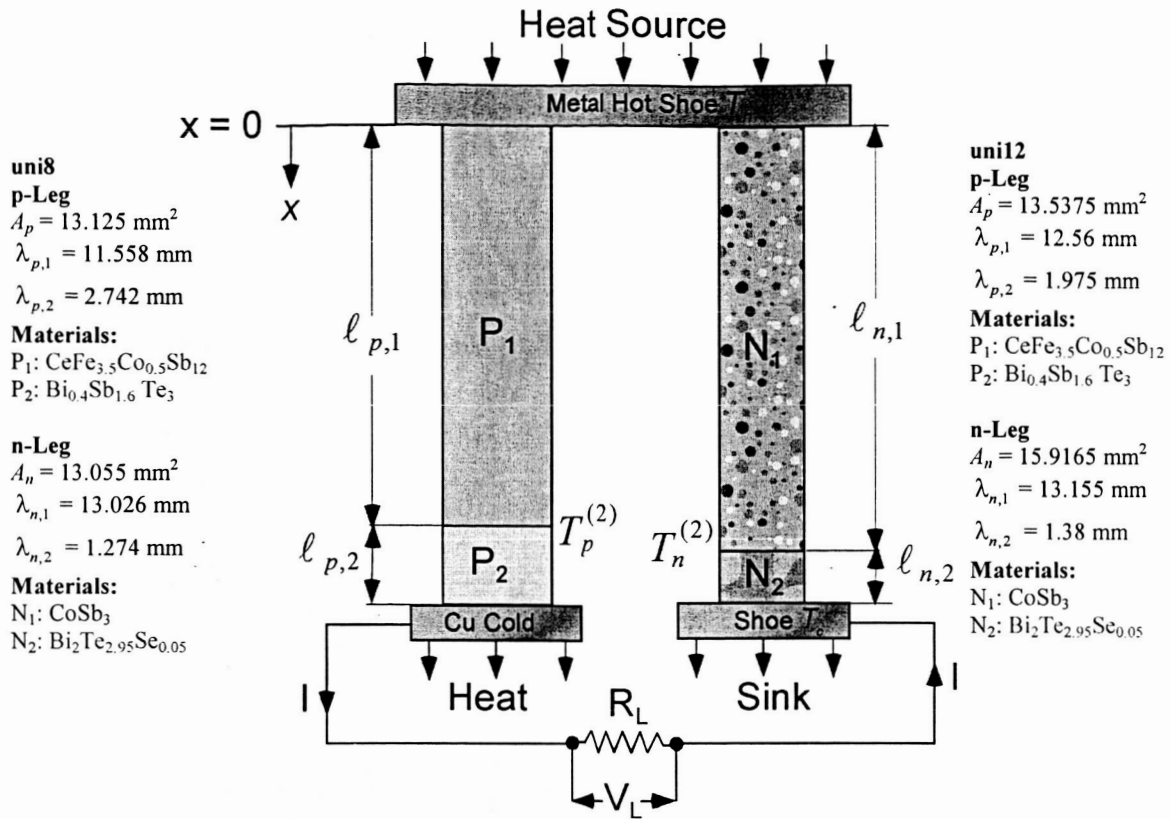


Figure 3-5 A Schematic of the uni8 and uni12 Compositions and Dimensions.

cold junction temperatures for in the uni12 test were kept constant at  $\sim 872 \text{ K}$  and  $316 \text{ K}$ , respectively. The measured I-V and I- $P_e$  characteristics for the uni8 and uni12 are shown in Figure 3-7a and Figure 3-7b, and in Figure 3-8a and Figure 3-8b, respectively. The dashed lines in these figures represent the predictions of the 1-D analytical model (chapter 2). The measured open circuit voltages for both uni8 and uni12 (Figure 3-7a and Figure 3-8a) are smaller than those predicted by the 1-D model, indicating that there were side heat losses in the tests. The open circuit voltage depends on the Seebeck coefficients of all segments (*i.e.* depends on the temperature distribution within the legs of the STU), which in turn depend on the amount of the side heat losses.

Figure 3-7a and Figure 3-7b for uni8, and Figure 3-8a and Figure 3-8b for uni12 show perfect agreement between the predictions of the 3-D model (solid lines) and the experimental data of the load voltage and electrical power for all values of the electrical load current, with a total contact resistance per leg in uni8 and uni12 of  $146$  and  $690 \mu\Omega\text{-cm}^2$ , respectively. These contact

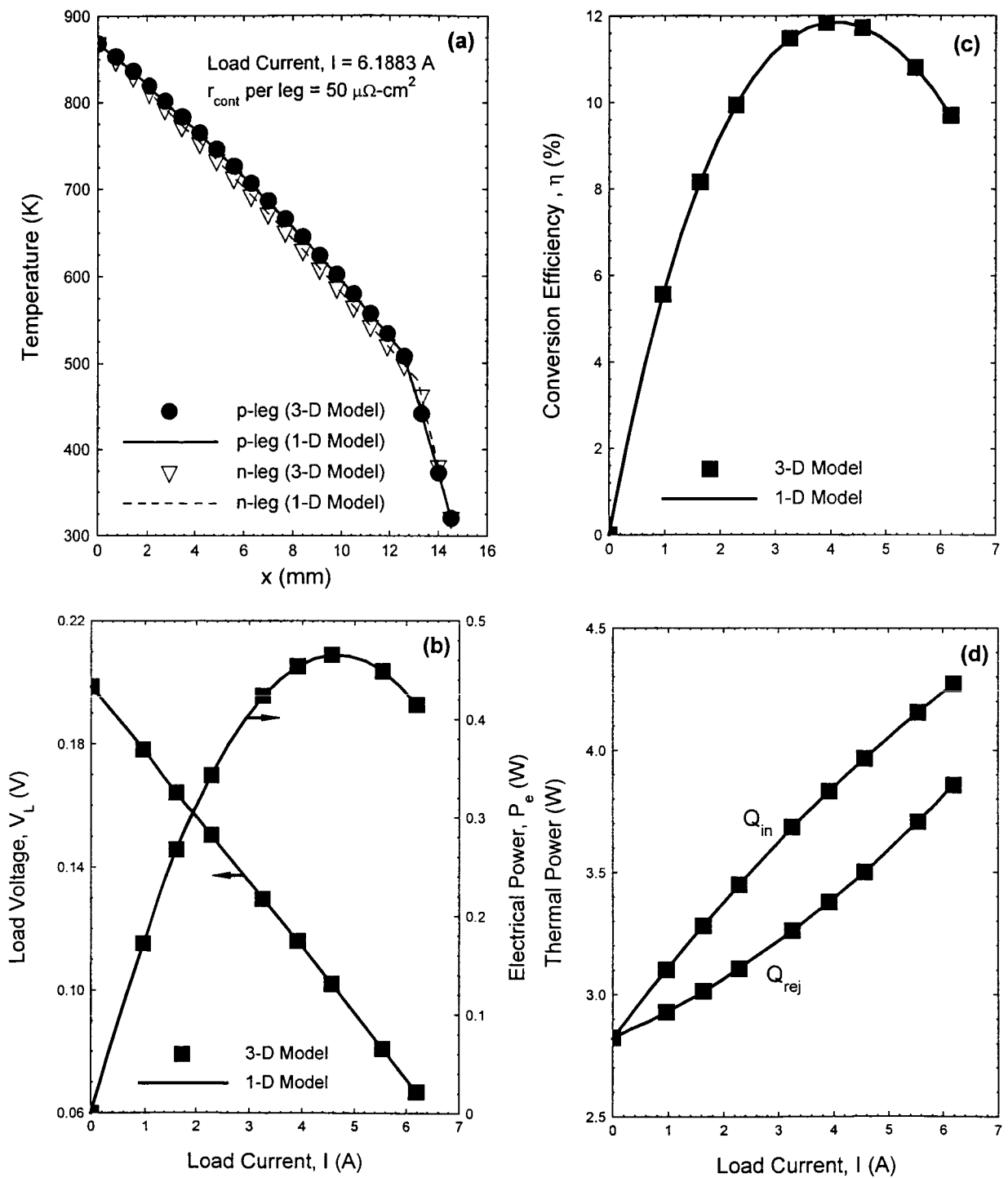


Figure 3-6 Comparisons of Predictions of 3-D and 1-D Models, Assuming Zero Side Heat Losses for uni12.

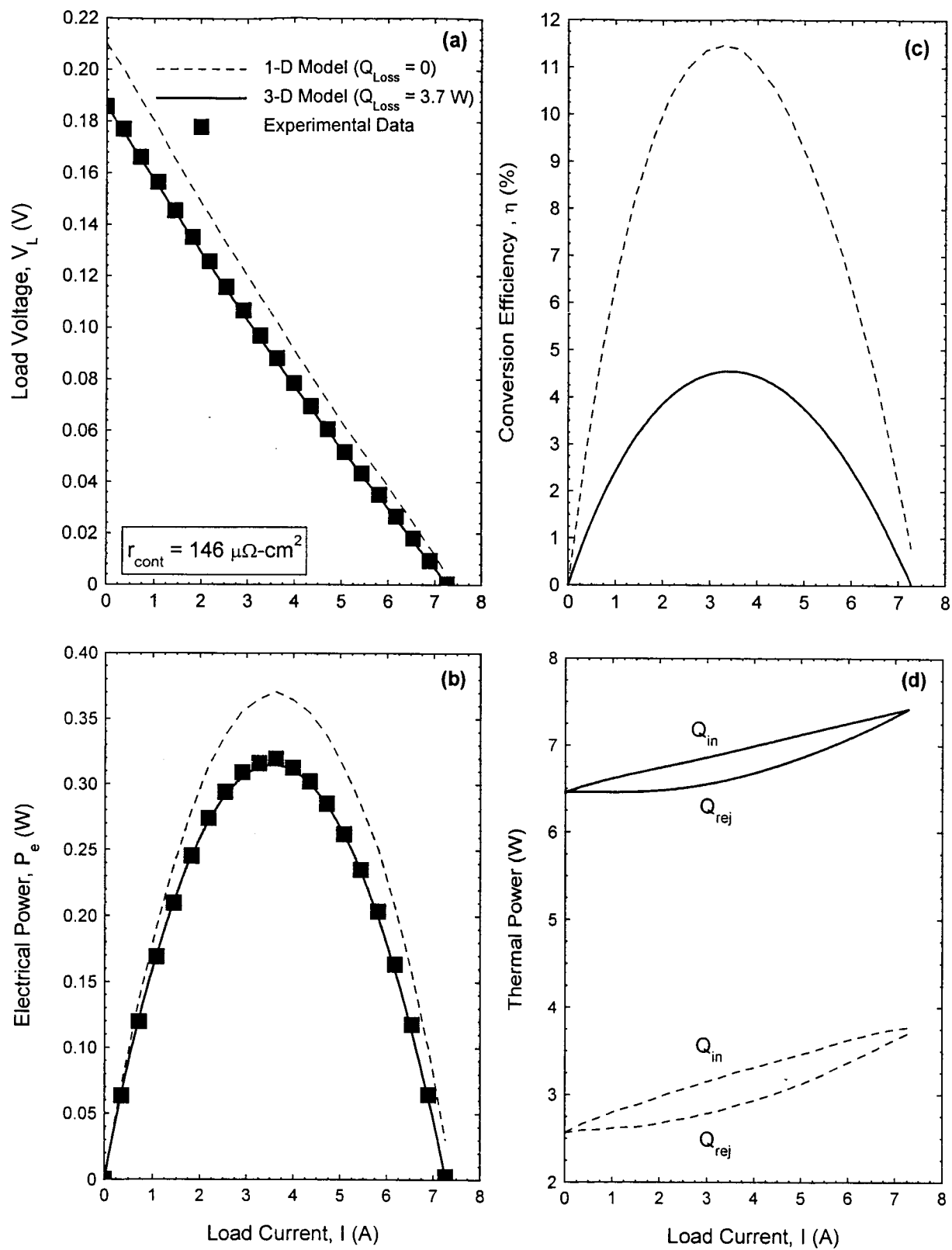


Figure 3-7 Comparisons of 3-D and 1-D Models with Test Data for uni8.

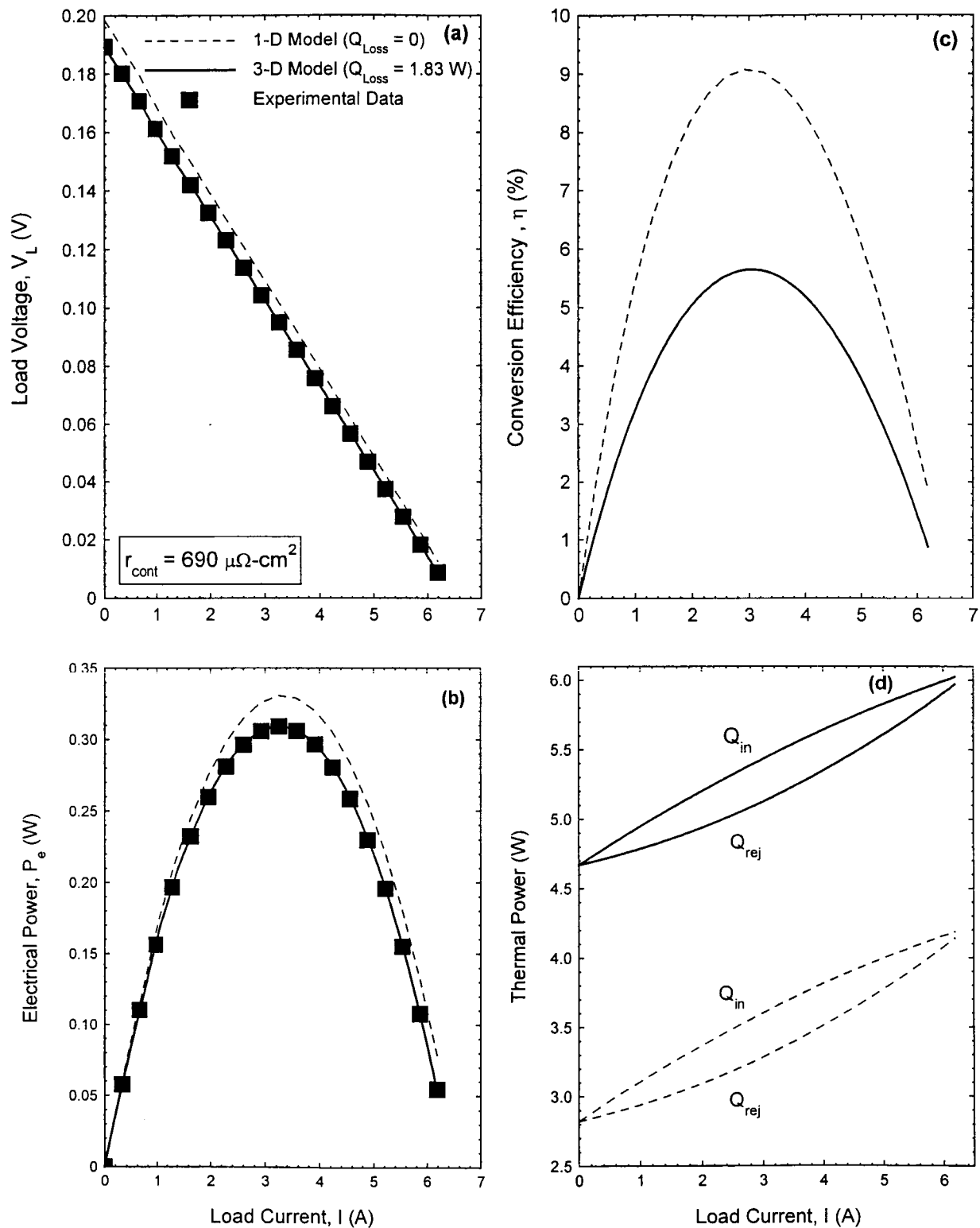


Figure 3-8 Comparisons of 3-D STU Model and 1-D Models with Test Data for uni12.

resistances are independent of the load current. Figure 3-7b and Figure 3-7c for uni8 and Figure 3-8b and Figure 3-8c for uni12 show that, for the same contact resistance per leg, reducing the side heat losses would have significantly enhanced the measured performance of the STUs in the experiments, increasing not only the electrical power output, but also the conversion efficiency. For example, the peak electrical power and peak efficiency of uni8 would have increased, respectively, from the measured values of 0.315  $W_e$  and 4.55% to as much as 0.371  $W_e$  and 11.46%, if side heat losses were minimal (Figure 3-7b and Figure 3-7c). Similarly, the peak electrical power and peak conversion efficiency of uni12 would have increased from the measured values of 0.309  $W_e$  and 5.65% to 0.331  $W_e$  and 9.08%, respectively, had the STU been well insulated in the test (Figure 3-8b and Figure 3-8c).

The calculated input and rejected thermal powers for uni8 and uni12 using the 3-D (solid lines) and 1-D (dashed lines) models are compared in Figure 3-7d and Figure 3-8d, respectively. As shown in these figures, the input and rejected thermal powers in the tests are significantly greater than in the absence of side heat losses. For example, the calculated values of the input and rejected thermal power at the peak conversion efficiency for uni8 and uni12, decrease from  $\sim 6.92 W_{th}$  and  $6.60 W_{th}$  to  $\sim 3.23 W_{th}$  and  $2.85 W_{th}$  (Figure 3-7d) and from  $\sim 5.44 W_{th}$  and  $5.13 W_{th}$  to  $\sim 3.61 W_{th}$  and  $3.29 W_{th}$  (Figure 3-8d), in the absence of side heat losses, respectively. In the next two sections, sample predictions of the temperature fields in the n- and p-legs of uni8 in the tests are presented and discussed.

### 3.6 Calculated Temperature Fields

Because of the side heat losses, the three-dimensional temperature distributions at any cross-section in the n- and p-legs of uni8 are not uniform. Figure 3-9 and Figure 3-10 show a sample of the calculated temperature fields and side heat losses in a slice parallel to  $y$ - $z$  plane, at  $x = 12.12$  mm. This slice cuts through the  $P_2$  segment ( $p\text{-Bi}_{0.4}\text{Sb}_{1.6}\text{Te}_3$ ) and the  $N_1$  segment ( $n\text{-CoSb}_3$ ) (Figure 3-5). The facing surfaces of the n- and p-legs, which are assumed adiabatic, experience the highest temperatures as delineated in Figure 3-9a and Figure 3-9b for the p- and n-legs, respectively. On other three sides, the surface heat losses occur at lower temperatures. Figure 3-10a of the surface temperature distribution along the perimeter of  $P_2$  segment at  $x = 12.12$  mm, show the highest temperature of  $\sim 361$  K occurring at the middle of the right side,

while the lowest surface temperature of  $\sim 337$  K occurs at the corners of the lower and left sides and of the left and upper sides of the  $P_2$  segment.

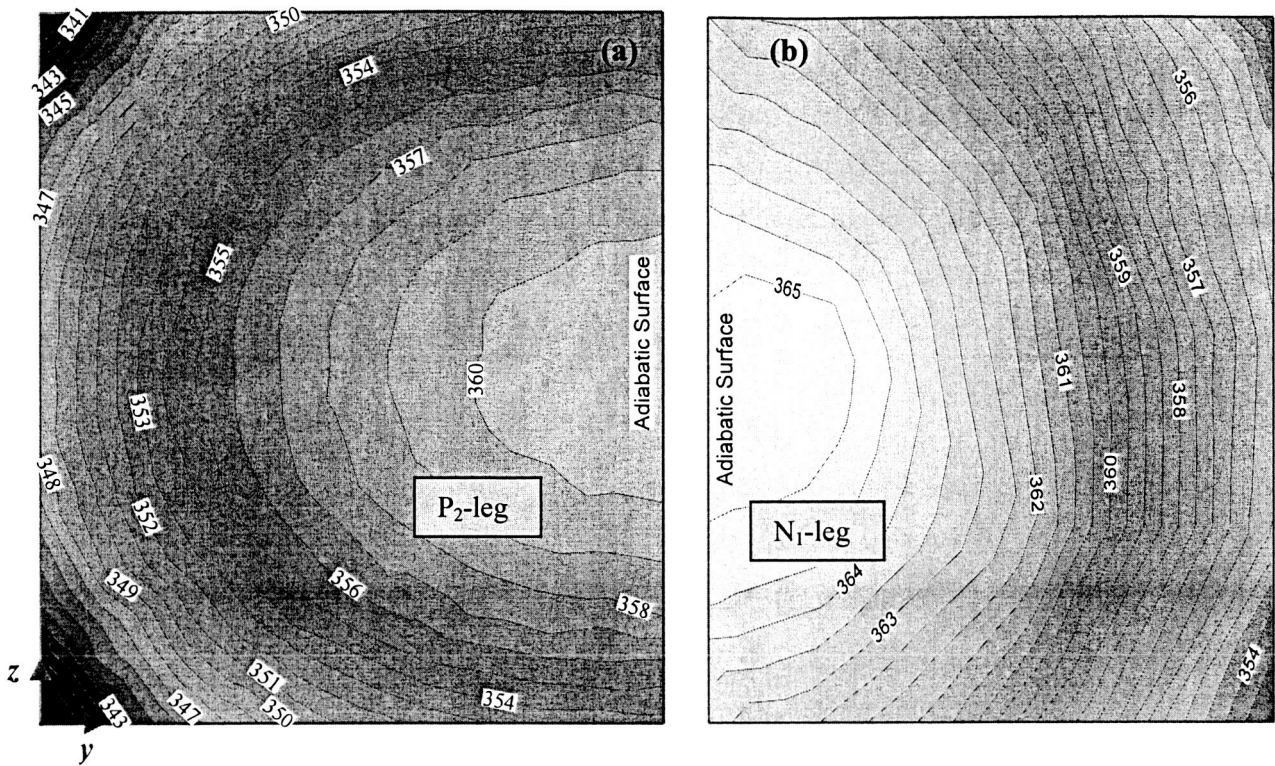


Figure 3-9 Calculated Temperature Field in a Slice in the n- and p-Legs of uin8 at  $x=12.12$  mm.

The calculated side heat losses per unit surface area along the perimeter of the  $P_2$  segment at  $x = 12.12$  mm are shown in Figure 3-10b. The highest side heat losses of  $\sim 1020$  W/m<sup>2</sup> occur at the corners of the lower and right sides and the upper and right sides of the  $P_2$  segment. The lowest side heat losses of  $\sim 727$  W/m<sup>2</sup>, however, occur at the corners of the lower and left sides and the upper and left sides of the  $P_2$  segment. A sample result on the effect of sublimation suppression coating on the temperature distribution of STU is performed using the 3-D STU model and discussed next.

### 3.7 Effect of Sublimation Suppression Coating on Temperature Field

Earlier tests of skutterudites uncouples performed at UNM-ISONPS vacuum facility ( $\sim 10^{-5}$  Pa) showed extensive sublimation of Antimony (Sb) from the n- and p-legs near the hot junction. The MAR-03, JUN-03 and JUL-03 tests are performed in Argon cover gas at 0.051-0.068 MPa in order in suppressing the sublimation of Sb from the n- and p-legs. The Argon cover gas was successful to suppress sublimation of Sb (see chapter 5 for more details). Note that, a thin  $\text{Si}_3\text{N}_4$

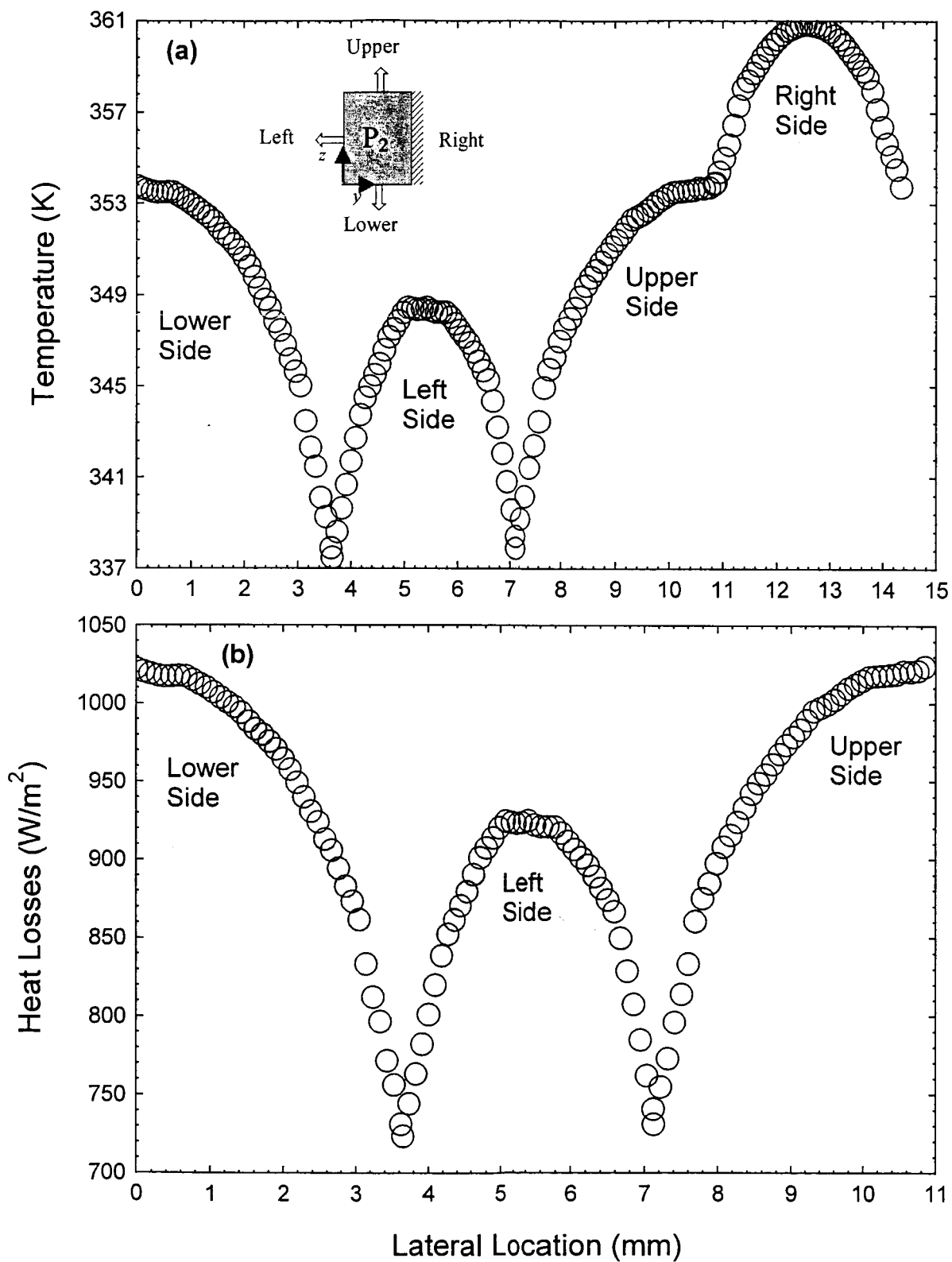


Figure 3-10 Calculated Temperature Field and Side Heat Losses in a Slice Parallel to y-z Plane in  $P_2$  and  $N_1$  Segments at  $x=12.12$  mm in uni8.

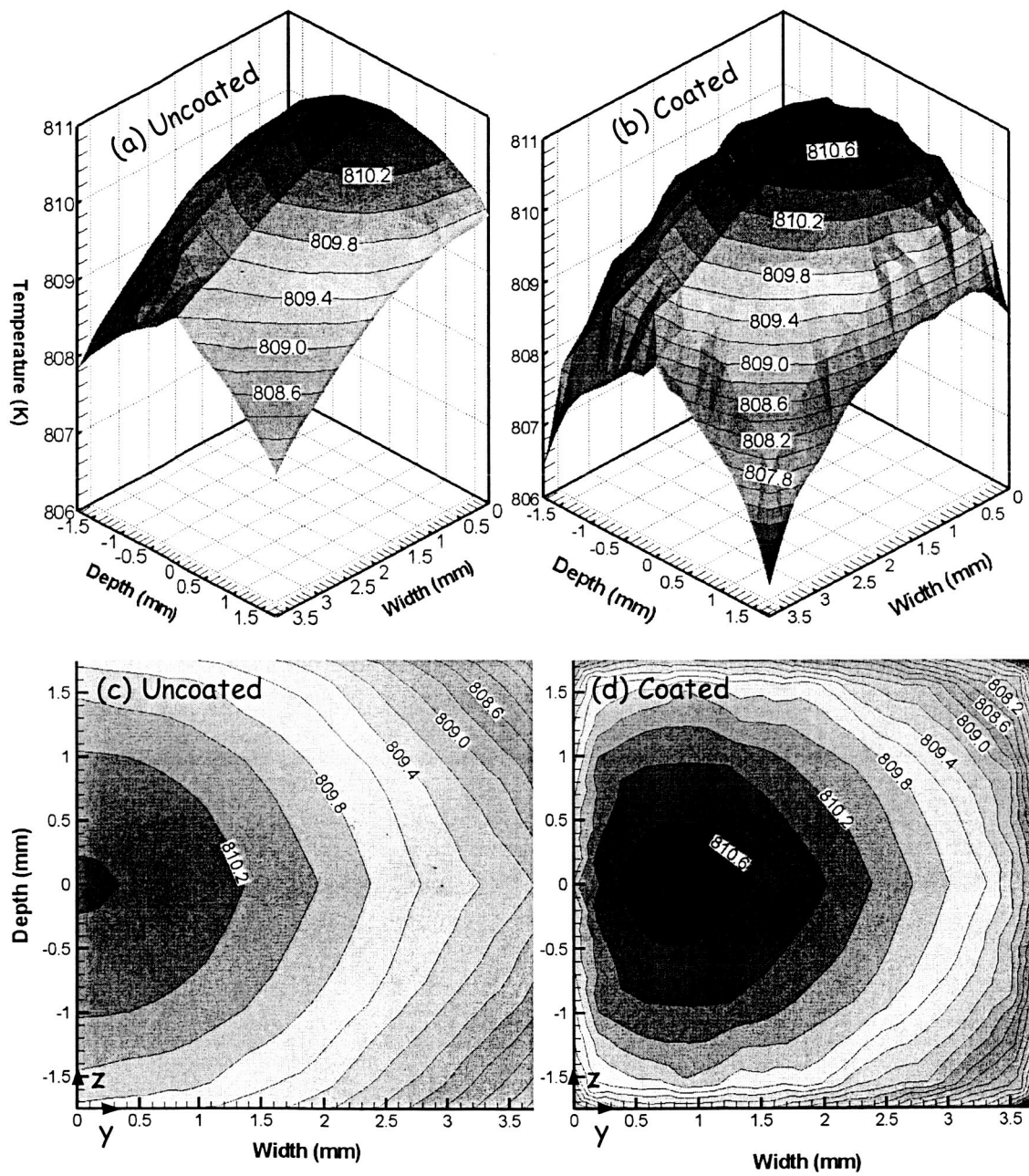


Figure 3-11 Temperature Field at a Slice in n-leg of uni8 at  $x = 0.2$  mm.



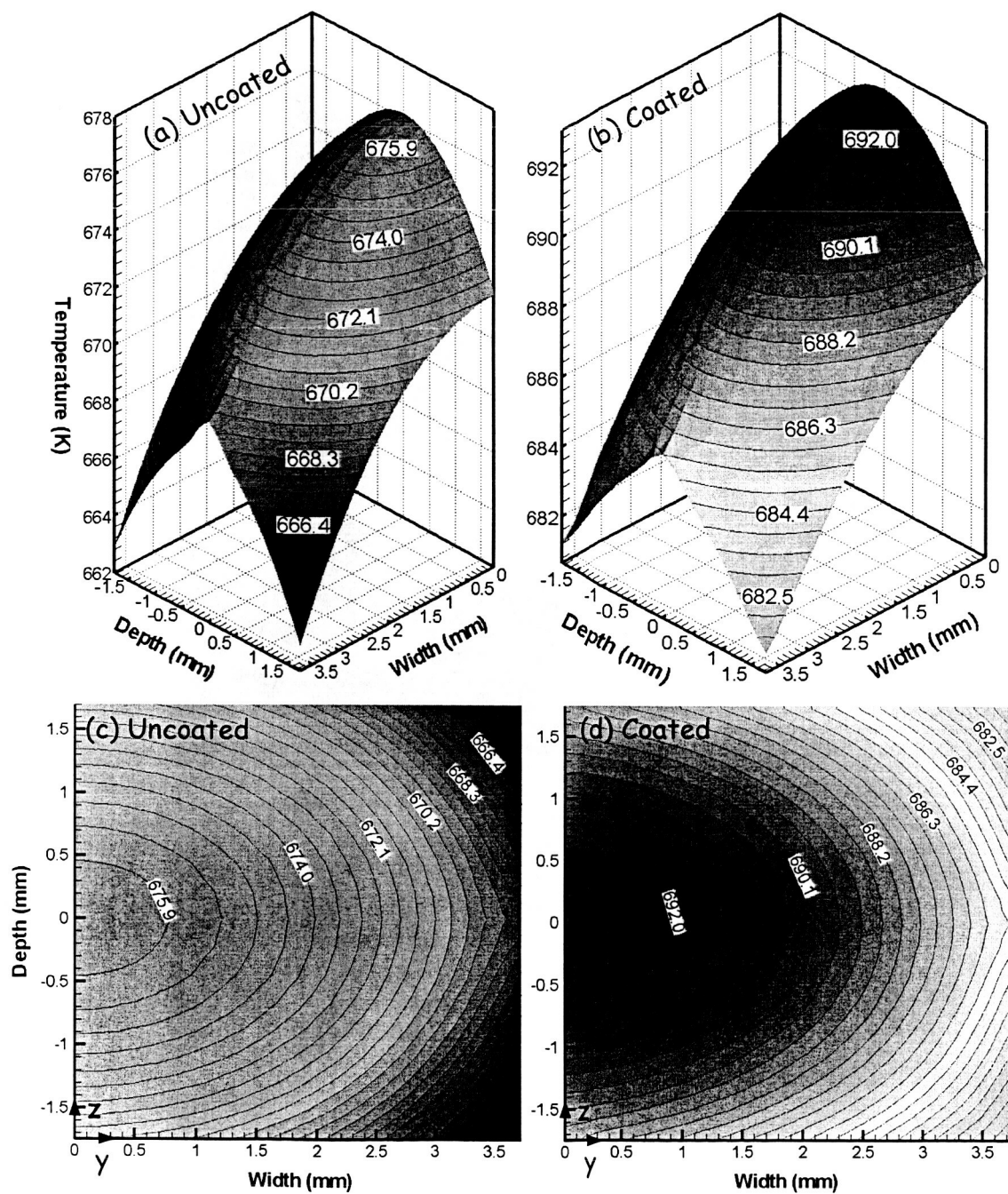


Figure 3-12 Temperature Field at a Slice in n-leg of uni8 at  $x = 2.5$  mm (Middle of Ti Coating).

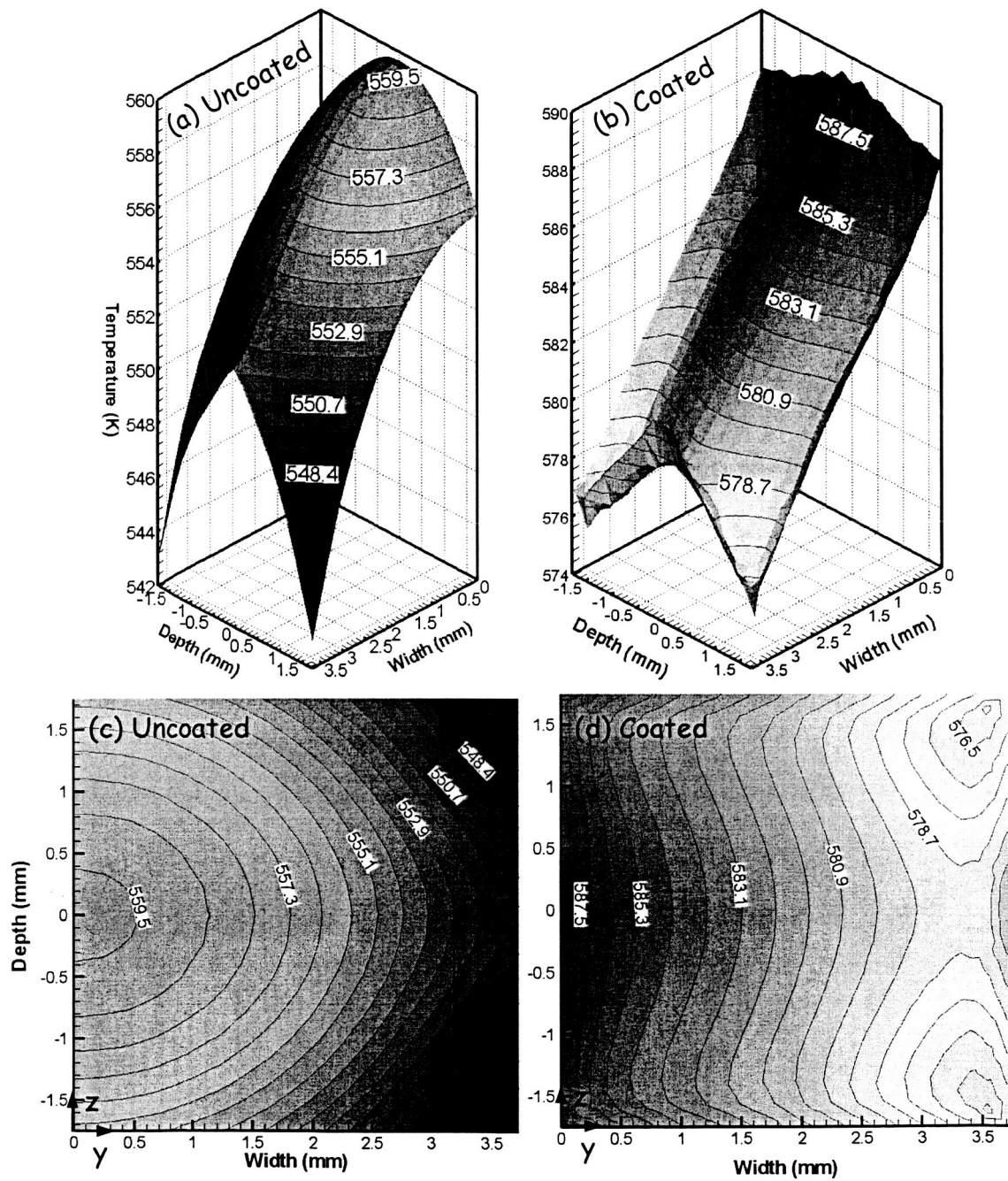


Figure 3-13 Temperature Field at a Slice in n-Leg of uni8 at  $x = 5.0$  mm (End of Ti Coating).

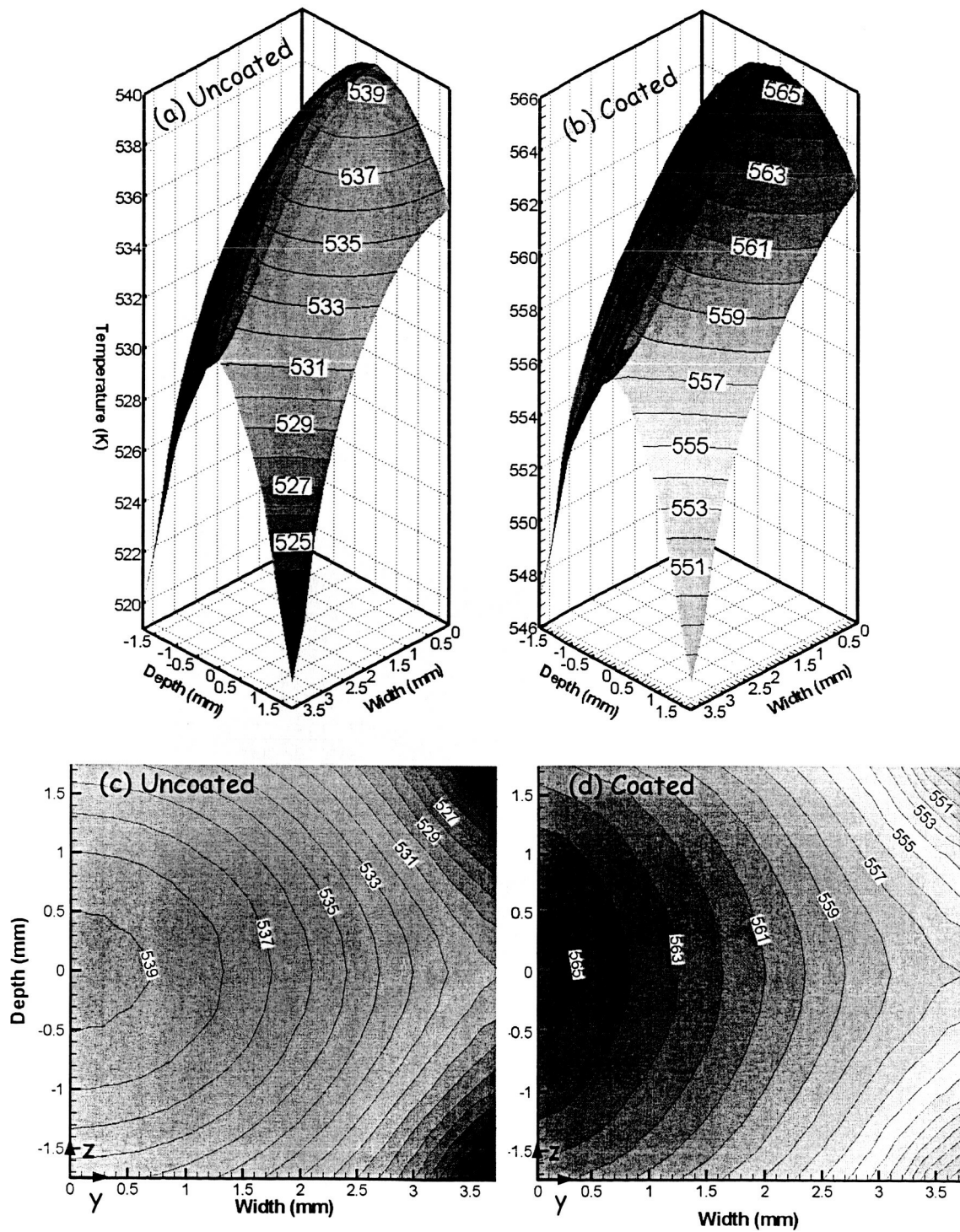


Figure 3-14 Temperature Field at a Slice in n-Leg of uni8 at  $x = 5.5$  mm (0.5 mm Below Ti Coating).

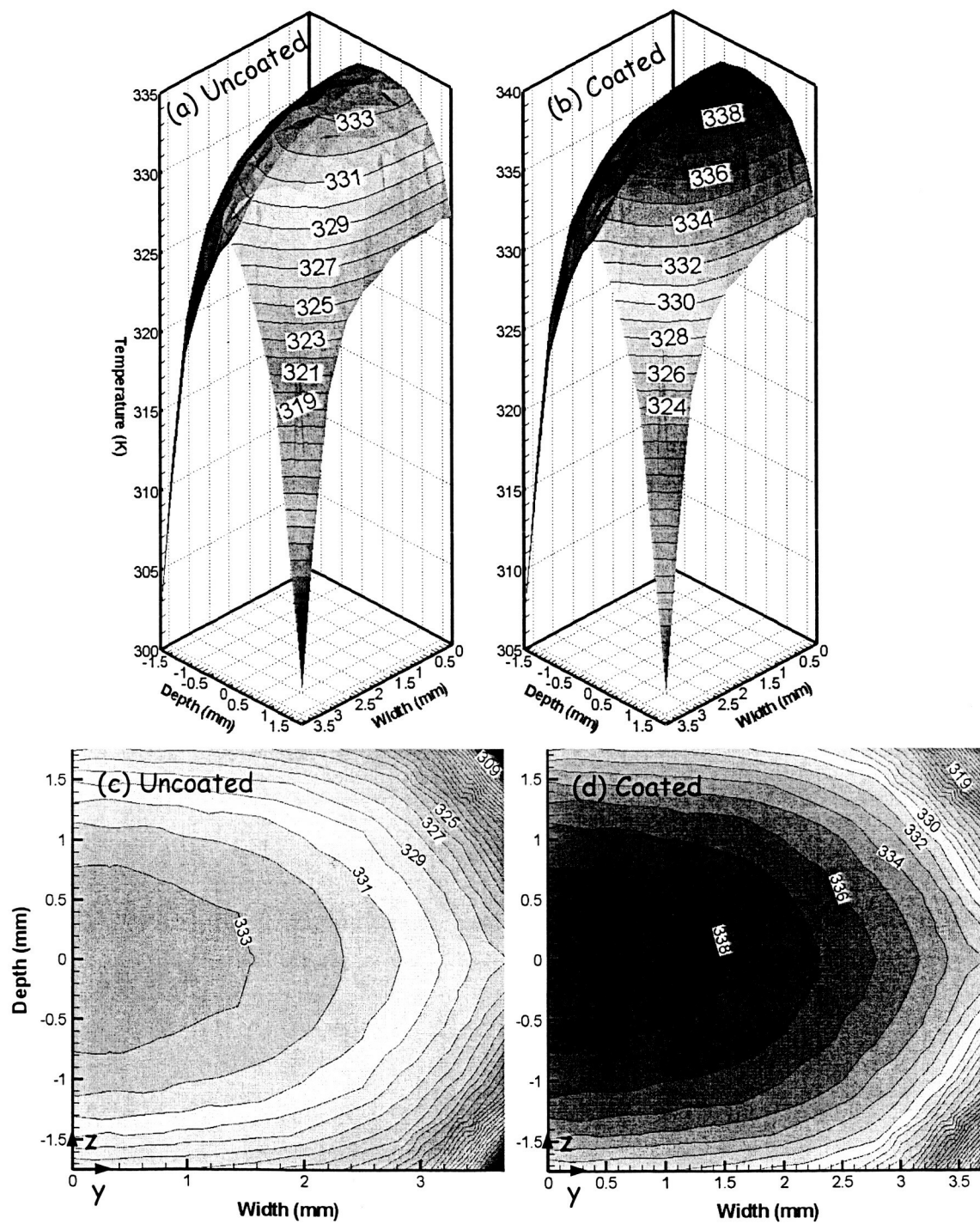


Figure 3-15 Temperature Field at a Slice in n-Leg of uni8 at  $x = 13.663$  mm (Middle of  $N_2$ ).

coating has been used for sublimation suppression coating for the SiGe unicouples used in the Radioisotope Thermoelectric Generators (RTGs). The sublimation suppression coating should be compatible with the materials of the n- and p-legs and chemically stable at high temperature of interest. In the next analysis, Titanium that is 5 mm long and a thickness of 25  $\mu\text{m}$  is assumed to coat the n- and p-legs near the hot junction of uni8 (see Figure 3-5). The calculated effect of the Ti coating on the temperature fields in slices at different axial location in n-leg of uni8 is discussed for  $T_h = 832\text{ K}$ ,  $T_c = 306\text{ K}$  and  $I_L = 5.44\text{ A}$ . Also, comparisons of the temperature fields in slices at different axial location in n-leg of the coated and uncoated uni8, at the same test conditions listed above is detailed below.

Figure 3-11 shows a comparison of the temperature fields in a slice parallel to  $y$ - $z$  plane and close the hot junction ( $x = 0.2\text{ mm}$ , see Figure 3-5) for uncoated and coated uni8 with Ti. Because of side heat losses, the temperature field is not uniform (see Figure 3-11). As shown in Figure 3-11a - Figure 3-11c, the highest temperature in this slice occurred at the middle of the side facing the p-leg ( $y = 0$ ) for uncoated uni8 (810.4 K) while the minimum temperature (808 K) occurs at the side of  $y = 3.73\text{ mm}$  and  $z = \pm 1.75\text{ mm}$ . For a coated uni8 with Ti, the location of the highest temperature (810.7 K) is shifted toward the center of the leg at  $y = 0.836\text{ mm}$  and  $z = 0$  and the minimum temperature (806.7 K) occurs at  $y = 3.73\text{ mm}$  and  $z = \pm 1.75\text{ mm}$  (Figure 3-11b & Figure 3-11d). The maximum temperature difference in this slice ( $x = 0.2\text{ mm}$ ) is 2.4 K, and 4.0 K for the uncoated (Figure 3-11a & Figure 3-11c) and coated uni8 (Figure 3-11b & Figure 3-11d), respectively. Since Ti has higher thermal conductivity than that for  $\text{CoSb}_3$ , it behaves as a heating jacket removing more heat from the heat source and consequently resulting in a higher temperature in the coated uni8.

Figure 3-12 shows the temperature field in slices at  $x = 2.5\text{ mm}$  for both the uncoated and coated uni8. These slice cut axially through the middle of the Ti coating for the coated uni8. The maximum and minimum temperatures in this slice for the uncoated uni8 are 676.2 K ( $y = 0$  and  $z = 0$ ) and 663.3 K ( $y = 3.73\text{ mm}$  and  $z = \pm 1.75\text{ mm}$ ), respectively, with a maximum temperature difference of 12.9 K (Figure 3-12a and Figure 3-12c). While, the maximum and minimum temperatures in the slice for the coated uni8 are 692.5 K ( $y = 0$  and  $z = 0$ ) and 681.3 K ( $y = 3.73\text{ mm}$  and  $z = \pm 1.75\text{ mm}$ ), respectively, with a maximum temperature difference of 11.2 K (Figure 3-12b and Figure 3-12d). As delineated earlier, Ti which has high thermal

conductivity, acts as a heating jacket and results in a higher temperature in the coated than in uncoated uni8 in all the slices along the n-leg (see Figure 3-11 – Figure 3-15).

Figure 3-13, Figure 3-14 and Figure 3-15 show the temperature fields in slices at  $x = 5.0$  mm (at the end of Ti coating for the coated uni8), at  $x = 5.5$  mm (0.5 mm below the end of the Ti coating), and at  $x = 13.663$  mm (middle of the clod segment of n-leg made of  $\text{Bi}_2\text{Te}_{2.95}\text{Se}_{0.05}$ ), respectively, for both the uncoated and coated uni8. These figures indicate that the temperature in the coated uni8 is higher than that for the uncoated uni8. The maximum temperature difference in the slice located at  $x = 5.0$  mm is 16.4 K (Figure 3-13a and Figure 3-13c) and 13.4 K (Figure 3-13b and Figure 3-13d) for the uncoated and coated uni8, respectively. While these values are 19 K (Figure 3-14a and Figure 3-14c) and 18 K (Figure 3-14b and Figure 3-14d), and 30.4 K (Figure 3-15a and Figure 3-15c) and 30.2 K (Figure 3-15b and Figure 3-15d) for the uncoated and coated uni8, respectively, in the slices located at  $x = 5.5$  mm and  $x = 13.663$  mm, respectively.

### 3.8 Summary

A three-dimensional model of STUs is developed and incorporated into the ANSYS commercial software. The model solves the governing equations, with the prescribed boundary conditions, using the Finite Element Methodologies (FEM) and meshing capabilities in ANSYS. This model treats isotropic or orthotropic physical and thermoelectric properties, which could also be temperature dependent. The model handles temperature, heat flux, convective and radiation boundary conditions. The technique of developing this 3-D STU model using the ANSYS commercial Software would enable performing thermal stress analyses and performance and optimization studies for coated and uncoated STU in laboratory tests and in actual Radioisotope Thermoelectric Generators (RTGs).

The model predictions are compared with experimental data of two STUs, uni8 and uni12, comprised of n-type  $\text{Bi}_2\text{Te}_{2.95}\text{Se}_{0.05}$  and  $\text{CoSb}_3$ -based alloys and p-type  $\text{Bi}_{0.4}\text{Sb}_{1.6}\text{Te}_3$  and  $\text{CeFe}_{3.5}\text{Co}_{0.5}\text{Sb}_{12}$ -based alloys, and tested at JPL between hot and cold side temperatures of  $\sim 305$  K and 885 K, respectively. The obtained 3-D calculations are not only of the side heat losses in these tests and their effect on the measured performance parameters, but also of the spatial distributions of these losses and of the 3-D temperature fields in the n- and p-legs. The predictions of the present 3-D model of the various performance parameters and the temperature

distributions in the n- and p-legs of uni12, are in excellent agreement with the predictions of a 1-D analytical model detailed in chapter 2, when assuming zero side heat losses.

The present 3-D model calculated the side heat losses in the experiments for two STUs, uni8 and uni12, in recent tests at JPL. The results for uni8 and uni12 indicate that, due to the high calculated side heat losses in the experiments of  $3.7 W_{th}$  and  $1.83 W_{th}$  and of the contact resistance per leg of 146 and  $690 \mu\Omega\text{-cm}^2$ , respectively, the predicted peak electrical power and peak conversion efficiency are significantly lower than their values had the unicouples been better thermally insulated in the tests. The measured peak electrical power and the calculated conversion efficiency for uni8 and uni12 are  $0.315 W_e$  and 4.55%, and  $0.309 W_e$  and 5.65%, respectively, compared to  $0.371 W_e$  and 11.46%, and  $0.331 W_e$  and 9.09% with minimal side heat losses.



## **4 CASCADED THERMOELECTRIC MODULES-ADVANCED RADIOISOTOPE POWER SYSTEMS (CTM-ARPSs) (UNM-ISPNS)**

In this chapter, Conceptual designs of Advanced Radioisotope Power System (ARPS) with Cascaded Thermoelectric Converters (CTCs) are developed and optimized for maximum efficiency operation for End-Of Mission (EOM) electrical power of 100  $W_e$ . These power systems each employs four General Purpose Heat Source (GPHS) bricks generating 1000  $W_{th}$  at Beginning-of-Life (BOL) and 32 Cascaded Thermoelectric Modules (CTMs). Each CTM consists of a top and a bottom array of thermoelectric unicouples, which are thermally, but not electrically, coupled. The top and bottom arrays of the CTMs are connected in series in two parallel strings with the same nominal voltage of > 28 VDC. The ARPSs nominal efficiency of 10.82% - 10.85% is  $\sim 90\%$  higher than that of State-of-the-Art (SOA) Radioisotope Thermoelectric Generators (RTGs). The SiGe unicouples in the top array of the CTMs are optimized for a nominal hot junction temperature of 1273 K and a constant cold junction temperature of either 780 K or 980 K, depending on the thermoelectric materials of the unicouples in the bottom array. For a SiGe cold junction temperature of 780 K, the unicouples in the bottom array have p-legs of TAGS-85 and n-legs of 2N-PbTe and operate at constant hot junction temperature of 765 K and nominal cold junction temperature of 476.4 K. When the SiGe cold junction temperature is 980 K, the unicouples in the bottom arrays of CTMs have p-legs of skutterudites  $CeFe_{3.5}Co_{0.5}Sb_{12}$  or  $CeFe_{3.5}Co_{0.5}Sb_{12}$  and  $Zn_4Sb_3$ , segments and n-legs of  $CoSb_3$  and operate at constant hot junction temperature of 965 K and nominal cold junction temperatures of 446.5 K or 493.5 K, respectively. The specific powers of the ARPSs with the present CTMs vary from 8.2  $W_e/kg$  to 8.8  $W_e/kg$ , which are 71% to 83% higher, respectively, than that of SOA-RTGs, and with  $\sim 43\%$  less  $^{238}PuO_2$  fuel.

### **4.1 Introduction**

Future planetary exploration of the solar system requires developing Advanced Radioisotope Power Systems (ARPSs) for electrical powers ranging from a few milli-watts to 100's  $W_e$ , or even more to enable a host of potential missions. NASA's Space Nuclear Initiative (SNI), announced in February 2002, aims at advancing key energy conversion technologies for ARPSs and for Space Reactor Power Systems (SRPSs). The former may generate 10's to hundreds of



$W_e$  while the latter could generate 10's to 100's of  $kW_e$  for deep space missions and long-duration surface and subsurface exploration of Mars and other planets. The focus of this chapter is on the development of conceptual designs of ARPSs with Cascaded Thermoelectric Converters (CTCs) for a nominal power of 100  $W_e$ , which are scalable to different power levels from as little as 25  $W_e$  and to 1  $kW_e$ .

Desirable conversion technologies for ARPSs are those that could decrease the amount of  $^{238}\text{PuO}_2$  fuel and increase the system's specific power for a reduced mission cost. Specific goals are to: (a) increase the sARPS specific power by a factor of two relative to State-Of-the Art (SOA) Radioisotope Thermoelectric Generators (RTGs) (4.6  $W_e/\text{kg}$ ); and (b) increase the ARPS efficiency by a factor of 2 to 4 compared to SOA-RTG (5.7%). Both goals are difficult to realize with a single conversion technology (El-Genk 2002). For example, the dynamic Free-Piston Stirling Engines (FPSEs) have an efficiency of 22% (Qui et al. 2002), significantly reducing the amount of  $^{238}\text{PuO}_2$  fuel. For a typical 100  $W_e$  ARPS only two GPHS bricks will be needed versus 7 in SOA-RTG (Qiu et al. 2002, and Thieme, Schreiber, and Mason 2002) with two 55  $W_e$  FPSEs. However, because FPSEs are heavy, the specific power of an ARPS with two, 55  $W_e$  FPSEs is slightly lower than that of SOA-RTG (El-Genk 2002); 4.5  $W_e/\text{kg}$ .

The developmental goal of high conversion efficiency and specific power ARPS could both be partially achieved using CTCs of currently available thermoelectric materials with well-known properties and fabrication techniques. SiGe unicouples, which had demonstrated excellent performance on numerous NASA space exploration missions with SOA-RTGs (Bennett, Lambardo and Rick 1987, and Carpenter 1970), are used in the top array of the (Cascaded Thermoelectric Module) CTM. These unicouples are cascaded with the unicouples in the bottom array of the CTMs, to ensure thermal, but not electrical, coupling. Because of the incompatibility of SiGe with candidate thermoelectric materials for the unicouples in the bottom array of the CTMs, they could not be assembled into segmented thermoelectric (STE) unicouples. The STE unicouples, with the proper selection of thermoelectric materials for various segments in the n- and p-legs, are excellent options for increasing conversion efficiency (Caillat, Fleurial, Borshchevsky 1997, Caillat et al. 1999 and 2000, El-Genk, Saber, and Caillat 2002 and 2003, El-Genk and Saber 2002). Skutterudites with high Figure-Of-Merits (FOM) have been tested and demonstrated high conversion efficiency at hot junction temperatures up to 973 K (El-Genk et al. 2003, and El-Genk, Saber and Caillat 2004). Other thermoelectric

materials with high FOMs that are capable of operating at hot junction temperatures up to 1273 K and compatible with skutterudites are currently being developed at the Jet Propulsion Laboratory, California Institute of Technology, in Pasadena, CA. The SiGe has a FOM that increases with temperature and is the only thermoelectric material currently qualified to operate at hot junction temperatures up to 1273 K. Therefore, developing CTCs that take advantage of the high temperature operation of SiGe and of other thermoelectric materials, which have high FOMs at lower temperatures, could be a viable option. This option is explored in some detail in this chapter relative to its potential use in ARPSs for 7-10 year missions with a nominal EOM power of 100 W<sub>e</sub>. Details on the optimization of CTCs and CTMs are presented elsewhere (El-Genk and Saber 2004).

The objective of this chapter is to develop conceptual design of ARPS with CTMs for a nominal EOM power of 100 W<sub>e</sub>. Demonstrated is the possibility of operating these ARPSs at an efficiency  $\geq 10\%$  and with a specific power that much higher than that of SOA-RTG. The uncouples in the bottom arrays of the CTMs have one of the following three compositions, which are selected for optimum performance at a constant hot junction temperature of the top SiGe uncouples of either 780 K or 980 K. For the lower temperature, the bottom uncouples have p-legs of TAGS-85 and n-leg of 2N-PbTe; and for the higher temperature they have p-leg of either of CeFe<sub>3.5</sub>Co<sub>0.5</sub>Sb<sub>12</sub> or CeFe<sub>3.5</sub>Co<sub>0.5</sub>Sb<sub>12</sub> and Zn<sub>4</sub>Sb<sub>3</sub> segments and n-legs of CoSb<sub>3</sub>. The TAGS-85 and 2N-PbTe could be used up to 700 K and are widely used in many applications including past RTGs; however, the skutterudites could be used up to 973 K and are currently at Technology Readiness Level-3 (TRL-3) and expected to reach TRL-5 in a few years.

## 4.2 Cascaded Thermoelectric Converters

To ensure compatibility with the current GPHS and aluminum casing of SOA-RTG, the developed CTMs are easily integrated into the aluminum casing and radiatively coupled to the GPHS bricks such that <sup>238</sup>PuO<sub>2</sub> fuel and the iridium cladding remain at their same design temperatures in SOA-RTGs. Therefore, the surface temperature of the CTMs is maintained at 1305 K, which corresponds to a hot junction temperature of 1273 K for the SiGe uncouples in the top arrays in the CTMs. The present ARPSs with CTMs each employ four GPHS bricks. Each brick generates 250 W<sub>th</sub> by radioactive decay of <sup>238</sup>PuO<sub>2</sub> fuel in four pellets clad in iridium

and encapsulated into two graphite impact shells (GIS), enclosed in a graphite reentry shell (Carpenter 1970).

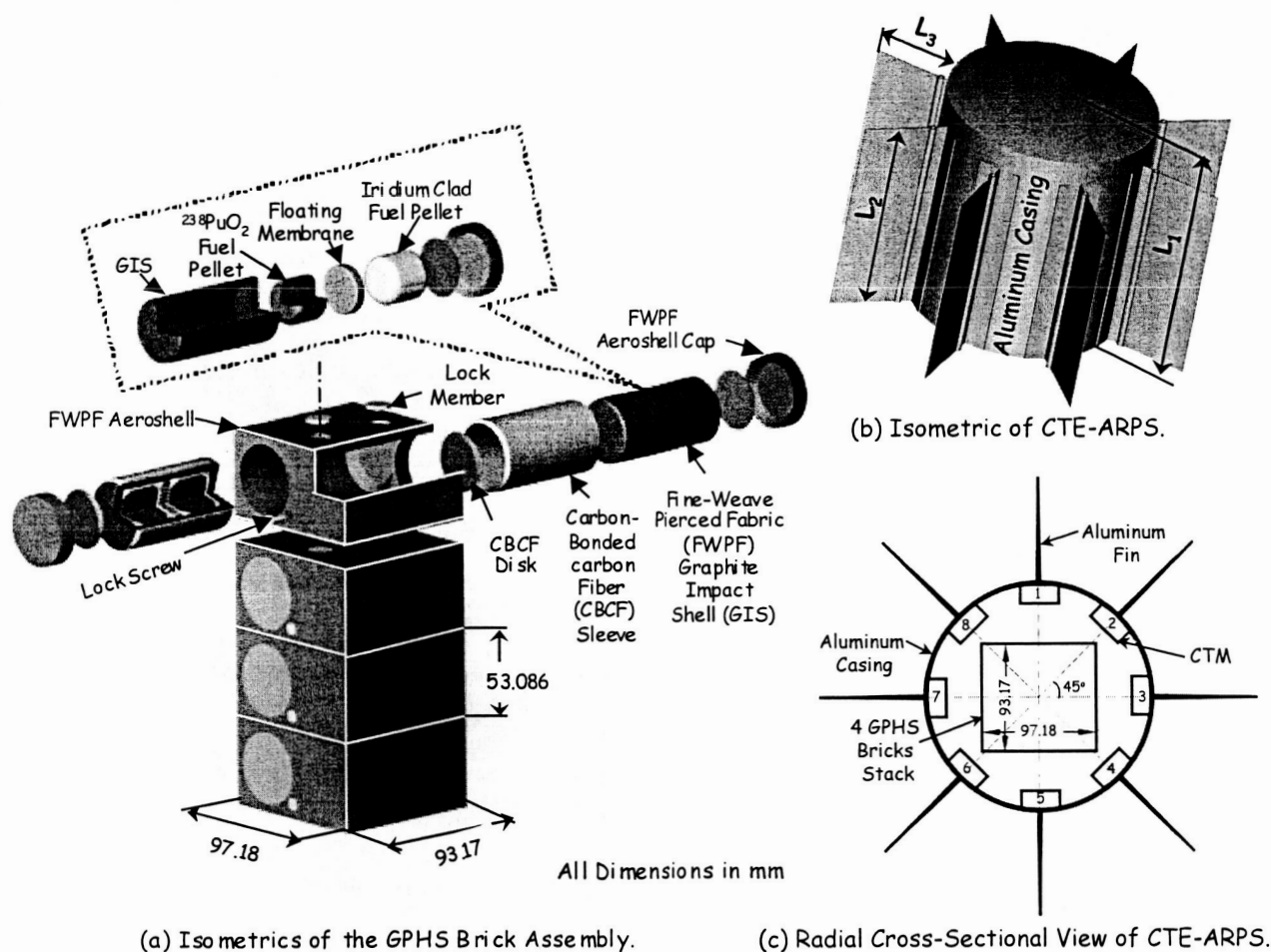


Figure 4-1 Arrangement of CTMs Around GPHS Brick in ARPSs.

Each of the developed ARPS employs a total of 32 CTMs; 8 per GPHS brick, arranged at 45° angle apart around the brick and radiatively coupled to it. Each CTM receives 1/8 of the thermal power of the GPHS brick, after accounting for 5% losses through the thermal insulation to the aluminum casing (Figure 4-1). Thus, each CTM receives 29.69  $W_{th}$  as input to the SiGe thermoelectric uncouples in the top array. Schematics of the design and the coupling of the SiGe uncouples in the top and bottom arrays of a CTM are shown in Figure 4-2; the top uncouples are thermally, but not electrically, coupled to the bottom uncouples in the CTM.

The number and cross-sectional areas of the n- and p-legs of the uncouples in the top and bottom arrays of CTMs are determined based on several considerations: (1) the SiGe uncouples operate at the thermal power received from the GPHS after accounting for 5% thermal losses and

the rate of heat rejected equals the rate of heat input to the bottom uncouples in the CTM; (2) the nominal hot junction of the SiGe uncouples,  $T_{h,T}$ , for operating at the peak efficiency is 1273 K and the cold junction temperature,  $T_{c,T}$ , is kept constant at either 780 K or 980 K, depending on the materials of the uncouples in the bottom array (Figure 4-2); (3) the SiGe and bottom uncouples in the CTMs are connected in series in two parallel strings each; all strings operate at the same nominal voltage of 28 VDC or higher; (4) the hot junction temperature of the bottom uncouples,  $T_{h,B}$ , is kept constant and 15 K lower than the cold junction of the top SiGe uncouples; while the cold junction temperature of the bottom uncouples,  $T_{c,B}$ , changes with load demand (Figure 4-2); (5) the length of the SiGe and bottom uncouples is same (10 mm), but the cross-sectional areas of the n- and p-legs are optimized for maximum efficiency at or near the nominal temperature of the hot junctions for the top and bottom uncouples, and (6) the CTMs temperature for heat rejection is kept 15 K below the cold junction of the bottom uncouples.

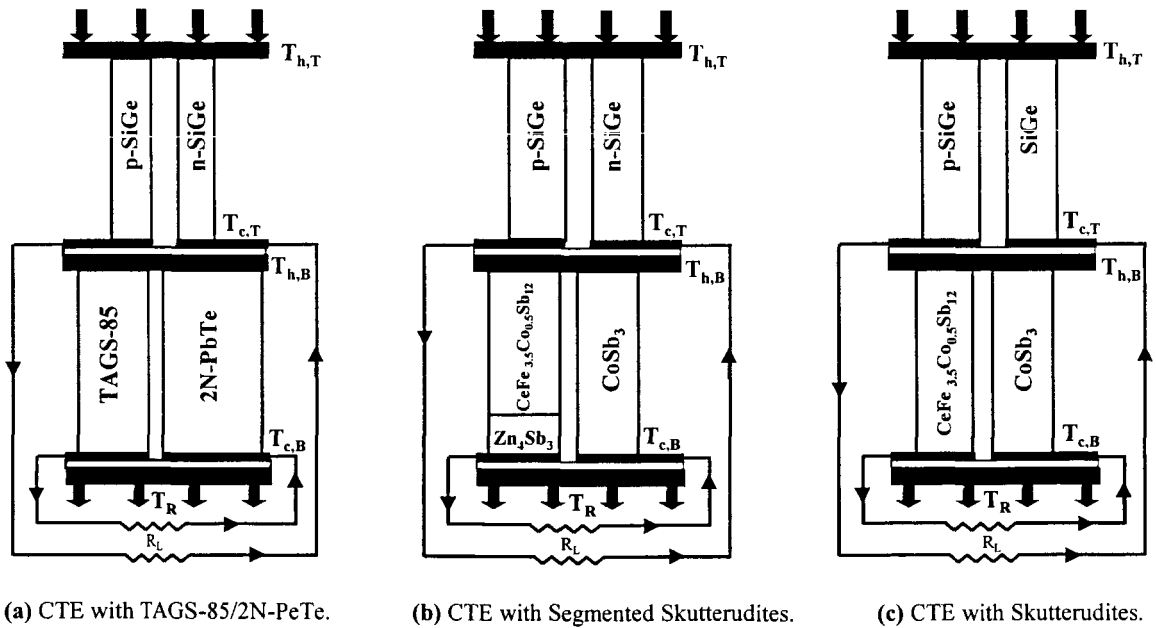


Figure 4-2 Schematics of the Cascaded Thermoelectric (CTE) Uncouples for ARPSs.

### 4.3 Thermoelectric Arrays

The number of uncouples in and the size of the top and bottom arrays in the CTM change with the material selections of the bottom uncouples and their nominal hot junction temperature. In the cascaded thermoelectric (CTE) configuration in Figure 4-2a, the nominal cold junction temperature for the SiGe uncouples is 780 K and that of the junction of the bottom uncouples is

15 K lower at 765 K. The CTM has 12 SiGe unicouples in a 3 x 4 rectangular array, for a total of 384 in the ARPS and 21 TAGS-85/2N-PbTe unicouples in 3 x 7 array, for a total of 672 in the ARPS. The unicouples in the top and bottom arrays are connected in series in two parallel

Table 4-1 Dimensions and Operation Parameters for CTEs and CTMsfor the ARPSs.

Parameter	Cascaded Thermoelectric Modules (CTMs)					
	Configuration, Figure 4-2a		Configuration, Figure 4-2b		Configuration, Figure 4-2c	
	Top Array	Bottom Array	Top Array	Bottom Array	Top Array	Bottom Array
<b>Temperatures &amp; Optimized Dimensions:</b>						
Hot Junction (K)	1273	765	1273	965	1273	965
Cold Junction (K)	780	476.4	980	493.5	980	446.5
$\Delta T$ across Unicouple (K)	493	288.6	293	471.5	293	518.5
Unicouple Length (mm)	10	10	10	10	10	10
p-leg c. s. area (mm <sup>2</sup> )	4.272	8.879	4.694	7.453	4.694	4.939
n-leg c. s. area (mm <sup>2</sup> )	4.272	16.439	4.694	5.749	4.694	5.180
p-leg Material (s)	SiGe	TAGS-85	SiGe	CeFe <sub>3.5</sub> Co <sub>0.5</sub> Sb <sub>12</sub> and Zn <sub>4</sub> Sb <sub>3</sub>	SiGe	CeFe <sub>3.5</sub> Co <sub>0.5</sub> Sb <sub>12</sub>
n-leg Material	SiGe	2N-PbTe	SiGe	CoSb <sub>3</sub>	SiGe	CoSb <sub>3</sub>
Footprint (mm)	53 x 37.71	53 x 37.71	53 x 37.71	53 x 37.71	53 x 37.71	53 x 37.71
Number of Unicouples/CTM	12 (3 x 4)	21 (3 x 7)	18 (3 x 6)	15 (3 x 5)	18 (3 x 6)	15 (3 x 5)
Number per GPHS Brick	96	168	144	120	144	120
Number in ARPS	384	672	576	480	576	480
<b>Nominal CTM Operation:</b>						
Input Power (W <sub>in</sub> )	29.67	27.94	29.7	28.67	29.7	28.67
Rejected Power (W <sub>th</sub> )	27.943	26.121	28.67	26.13	28.666	26.120
Nominal Current (A)	0.943	0.904	0.565	1.40	0.565	1.404
TE Efficiency (%)	5.877	6.522	3.443	8.850	3.443	8.880
Electric Power (W <sub>e</sub> )	1.745	1.822	1.022	2.537	1.022	2.546
Nominal Voltage (VDC)	1.930	1.930	1.81	1.81	1.81	1.81
Specific Power (W <sub>e</sub> /kg)	569.2	45.3	202.3	167.4	202.3	216.9
Power Density (W <sub>e</sub> /cm <sup>3</sup> )	1.702	0.343	0.605	1.281	0.605	1.677
<b>CTE:</b>						
- Specific Power (W <sub>e</sub> /kg)	82.4		176.1		212.5	
- Power Density (W <sub>e</sub> /cm <sup>3</sup> )	0.563		0.970		1.112	
<b>ARPSs with CTMs:</b>						
ARPS Load Voltage (VDC)	28 + 2.88		28 + 0.95		28 + 0.95	
ARPS TE Efficiency (%)	12.02		11.99		12.02	
ARPS Thermal Efficiency (%)	95		95		95	
ARPS Electrical Losses (%)	5		5		5	
ARPS Efficiency (%)	10.85		10.82		10.85	
ARPS BOM Power (W <sub>e</sub> )	108.5		108.2		108.5	
ARPS Radiator Base Temperature (K)	461.4		478.5		431.5	

strings with a nominal load voltage of 28+2.88 VDC (Table 4-1). The top and the bottom arrays have the same dimensions, measuring 53 x 37.71 mm (Figure 4-3a and Figure 4-3b). The SiGe unicouples wrapped in thermal insulation measure 4.57 mm x 4.336 mm in cross-section, while the insulated unicouples in the bottom array (Figure 4-2b) measure 5.047 mm x 8.381 mm in

cross-section. The assembled uncouples in the top and bottom arrays of the CTM are surrounded with additional multi-foils insulation to further reduce the side heat losses.

For the CTE configuration in Figure 4-2b, the top array of the CTM has 18 uncouples in a 3 x 6 array for a total of 576 in the ARPS and the bottom array has 15 uncouples in a 3 x 5 array for a total of 480. Similarly, with the CTE configuration in Figure 4-2c, the top array of the CTM has 18 uncouples in a 3 x 6 array for a total of 576 in the ARPS and the bottom array has 15 uncouples in a 3 x 5 array for a total of 480 in the ARPS. With the CTE configurations in Figure 4-2b and Figure 4-2c, the uncouples in the top and bottom arrays of the CTMs are connected in series in two parallel strings each with each string having a nominal load voltage of  $28 \pm 0.95$  VDC (Table 4-1).

For the same hot and cold junction temperatures, the efficiency of SOA-SiGe uncouples of 9.10% to 9.50% is 76% to 79% of that of the CTEs in Figure 4-2a-Figure 4-2c. For almost the same BOL power ( $\sim 105$  W<sub>e</sub>), a SOA-RTG would require 7 GPHS bricks, versus only 4 bricks for the CTM-ARPSs, to generate a nominal EOM power of 100 W<sub>e</sub> (Table 4-2). For almost the same BOL nominal power, the ARPSs with CTMs need only four GPHS bricks, a saving of 43% in the <sup>238</sup>PuO<sub>2</sub> fuel mass (Table 4-2). On the other hand, SOA-SiGe uncouples operating at the same hot and cold junction temperatures have specific powers that are 42%, 99%, and 83% higher than those of the CTEs with the configurations in Figure 4-2a, Figure 4-2b, and Figure 4-2c, respectively, and power densities that are 93%, 7.94%, and 4.5% higher, respectively. Such high power density and specific power of a SOA-SiGe uncouple, despite its lower thermoelectric efficiency, is because SiGe has significantly lower density (2.99 g/cm<sup>3</sup>) than the materials of the bottom uncouples in the CTEs (Figure 4-2a-Figure 4-2c); 6.313 g/cm<sup>3</sup>, 8.242 g/cm<sup>3</sup>, 7.85 g/cm<sup>3</sup>, 6.54 g/cm<sup>3</sup>, and 7.62 g/cm<sup>3</sup> for TAGS-85, 2N-PbTe, CeFe<sub>3.5</sub>Co<sub>0.5</sub>Sb<sub>12</sub>, Zn<sub>4</sub>Sb<sub>3</sub>, and CoSb<sub>3</sub>, respectively. However, the higher mass of the CTMs is more than compensated for by the reduction the <sup>238</sup>PuO<sub>2</sub> fuel mass, with the end result being higher specific power for the CTM-ARPSs (Table 4-2).

#### 4.4 Electrical Connections of CTM Arrays

Figure 4-4 presents the circuit diagram for connecting the top and bottom arrays in the CTMs in the ARPS to ensure high operation redundancy. As indicated earlier, the lengths of the uncouples in the top and the bottom arrays of the CTM are the same (10 mm) (Table 4-1), but

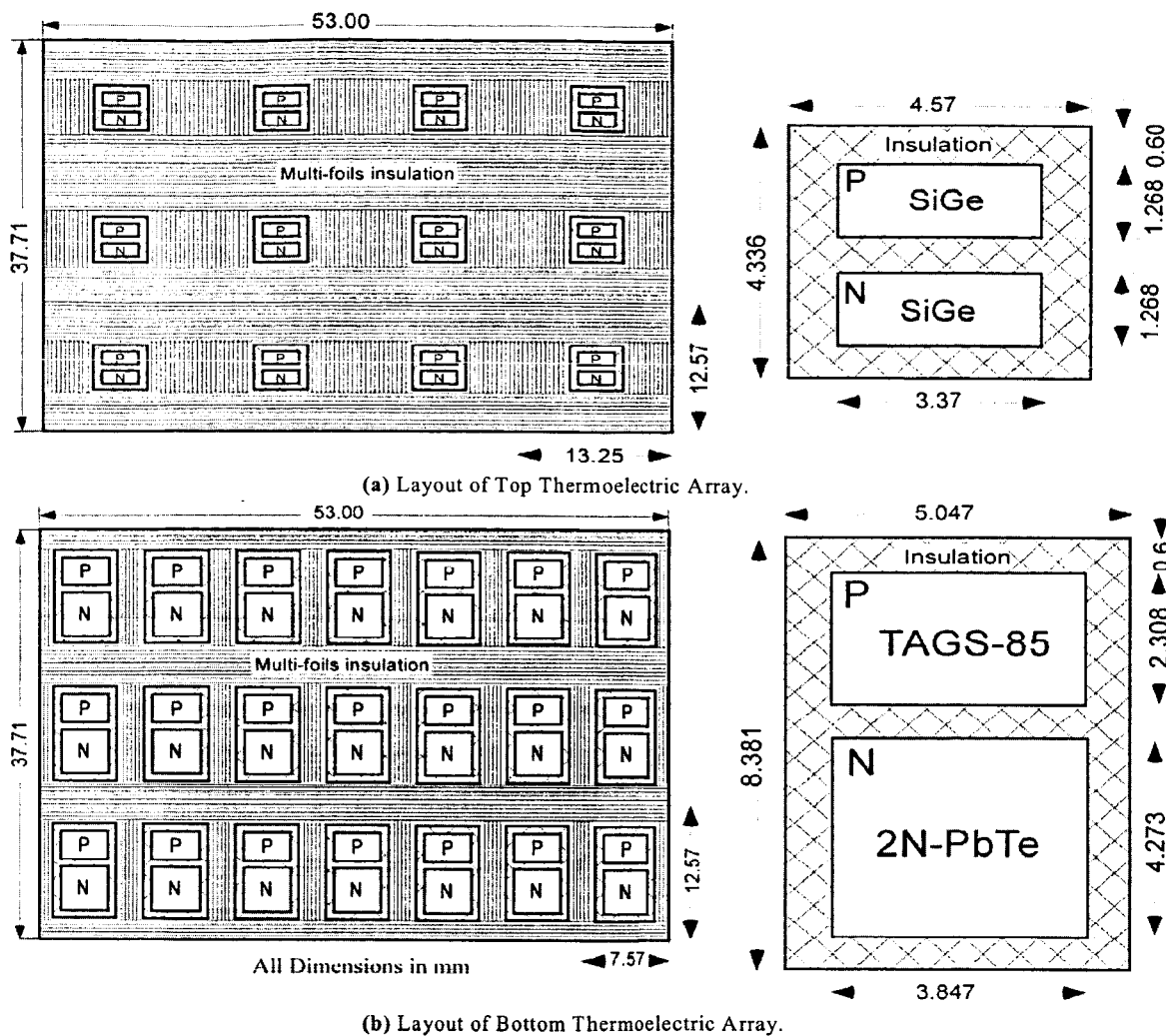


Figure 4-3 Arrangements of Unicouples in Top and Bottom Arrays of CTM with the CTE Configuration in Figure 4-2a.

the cross-sectional areas of the n- and p-legs are optimized for maximum efficiency operation and for having the same nominal terminal voltage for the top and the bottom arrays in the CTMs. This voltage is 1.930 VDC with the CTE configuration in Figure 4-2a and 1.81 VDC with CTE configurations in Figure 4-2b and Figure 4-2c (Table 4-1). The former results in a nominal load voltage of 30.88 VDC each for the two parallel strings of the top and of the bottom arrays of CTMs in the ARPSs. Each string has 16 arrays connected in series. This electrical connection provides four parallel strings operating at the same nominal load voltage (Table 4-1), two for the top and two for the bottom arrays.

In Figure 4-4, the letters “T” and “B” stand for the top and the bottom array, respectively. The three numbers in the subscript, when read from right to left, indicate the CTM on the opposite side of a primary CTM indicated by the second number (Figure 4-1 and Figure 4-4). The third number on the far right in the subscript indicates the GHPS brick number. For example,  $T_{151}$  indicates that the top array of the CTM number 1 (Figure 4-4) is connected in series with the top array in the CTM number 5, which both the GHPS brick number 1 supports (Figure 4-1). Similarly,  $B_{263}$  indicates that the bottom array in the CTM number 2 is connected in series with the bottom array in the CTM number 6; which are both provided for by the GHPS brick number 3 supports. The “T” and “B” blocks in Figure 4-4, respectively, indicate two top and two bottom arrays connected in series for a nominal load voltage of 3.86 VDC with the

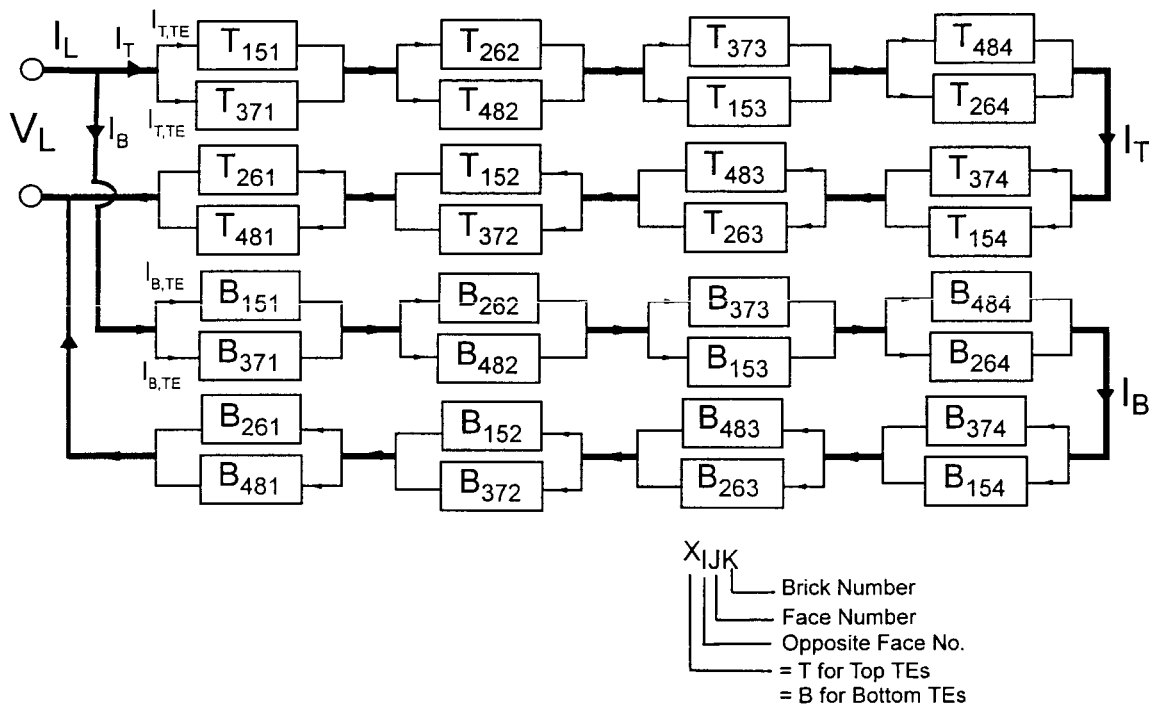


Figure 4-4 Circuit Diagram for Connecting the 32 CTMs in the Present CTM-ARPSs. uncouples of the configuration in Figure 4-2a, and 3.62 VDC with the uncouples of the configuration in either Figure 4-2b or Figure 4-2c. Thus, the 32 top and bottom arrays of the CTMs in the ARPS are integrated into 16 “T” and 16 “B” blocks (or Cascaded Thermoelectric Blocks (CTBs) in the circuit diagram in Figure 4-4. The 16 “T” and “B” CTBs in Figure 4-4 are paired into eight Cascaded Thermoelectric Units (CTUs) which are connected in series. In each CTUs, the two CTBs are connected in parallel, and each CTB consists of the arrays in two CTMs placed on opposite sides around a GHPS and connected in series. The eight top and bottom



CTUs connected in series in Figure 4-4 are referred to as the top and bottom Cascaded Thermoelectric Converters (CTCs), respectively.

In summary, the circuit diagram in Figure 4-4 consists of one top and one bottom CTC operating at same nominal load voltage but different current. This load voltage is 30.88 VDC with the CTE configuration in Figure 4-2a, and 28.95 VDC with the CTE configuration in either Figure 4-2b or Figure 4-2c. Each CTC converter consists of eight CTUs connected in series. Each of the top and the bottom CTUs operate nominally at the same load voltage, which depends on the configuration of the CTE (Figure 4-2). For the CTE configuration in Figure 4-2a, the nominal voltage for either the top or the bottom CTU is 3.86 VDC, and it is 3.62 VDC when using the CTE configuration in Figure 4-2b or Figure 4-2c. Each CTU consists of two CTBs connected in parallel and operate at the same nominal voltage. Each CTB consists of two CTAs connected in series, and each provides half the nominal voltage of either the CTB or the CTU, and half the nominal current of the CTU. The nominal current of the CTB is the same as the CTAs, but half that of the CTC. Therefore, the nominal load voltage,  $V_L$ , is the same as those of the top and bottom CTCs, but the nominal load current,  $I_L = I_T + I_B$ , where  $I_T$  and  $I_B$  are the nominal current of the top and bottom CTC, respectively. Also,  $I_B = 2 \times I_{B, TE}$  and  $I_T = 2 \times I_{T, TE}$ , where  $I_{B, TE}$  and  $I_{T, TE}$  are the nominal current for the bottom and top CTA, respectively. The

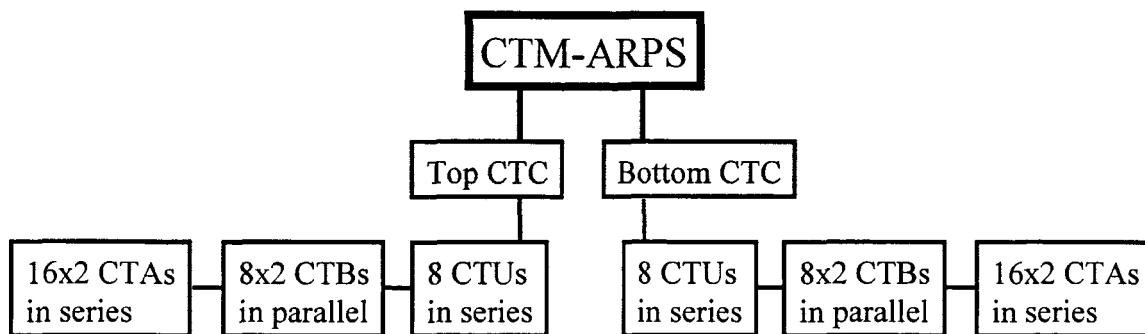


Figure 4-5 Building Blocks of CTMs in the Present CTM-ARPSs.

electric currents of CTB and CTA are the same and equal to  $0.5 I_T$  or  $0.5 I_B$  in the top or bottom CTC, respectively. A break down of the building blocks of the CTCs in ARPS is shown in Figure 4-5. In the circuit diagram in Figure 4-4, special unidirectional diodes could be connected in parallel with the two CTBs in each CTU to ensure that a failure of one CTA within a CTB will neither change the nominal electrical current of the CTC that it belongs to nor cause a complete loss of the CTC.

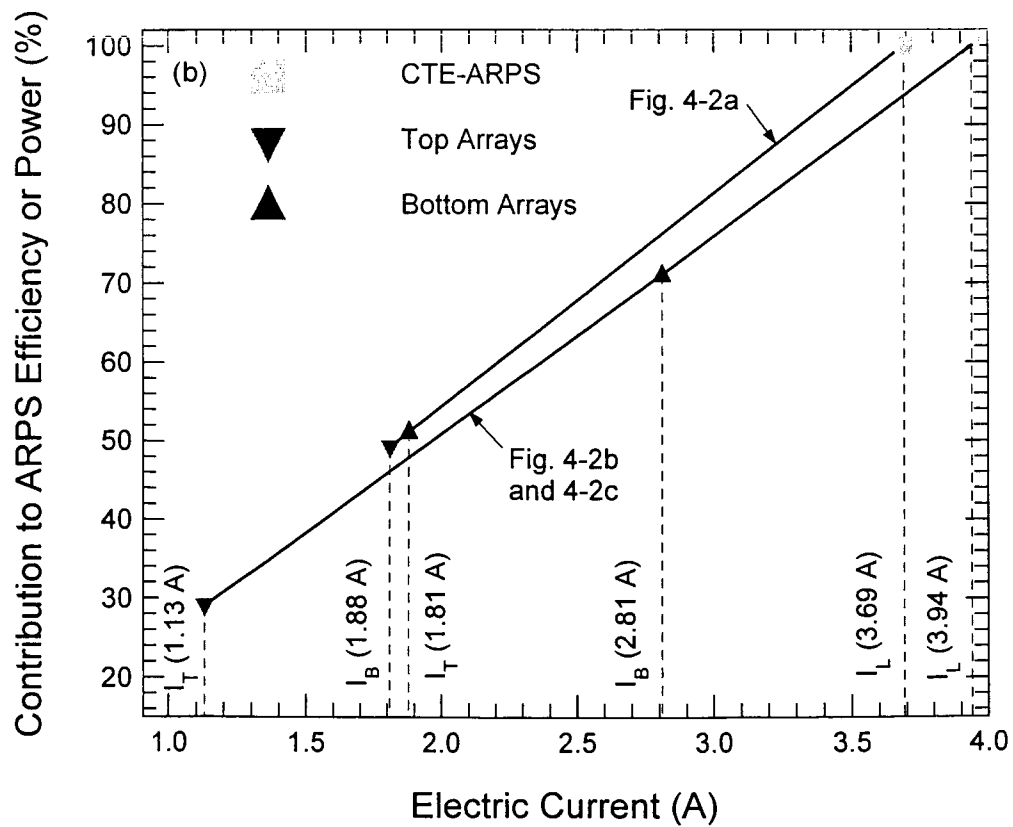
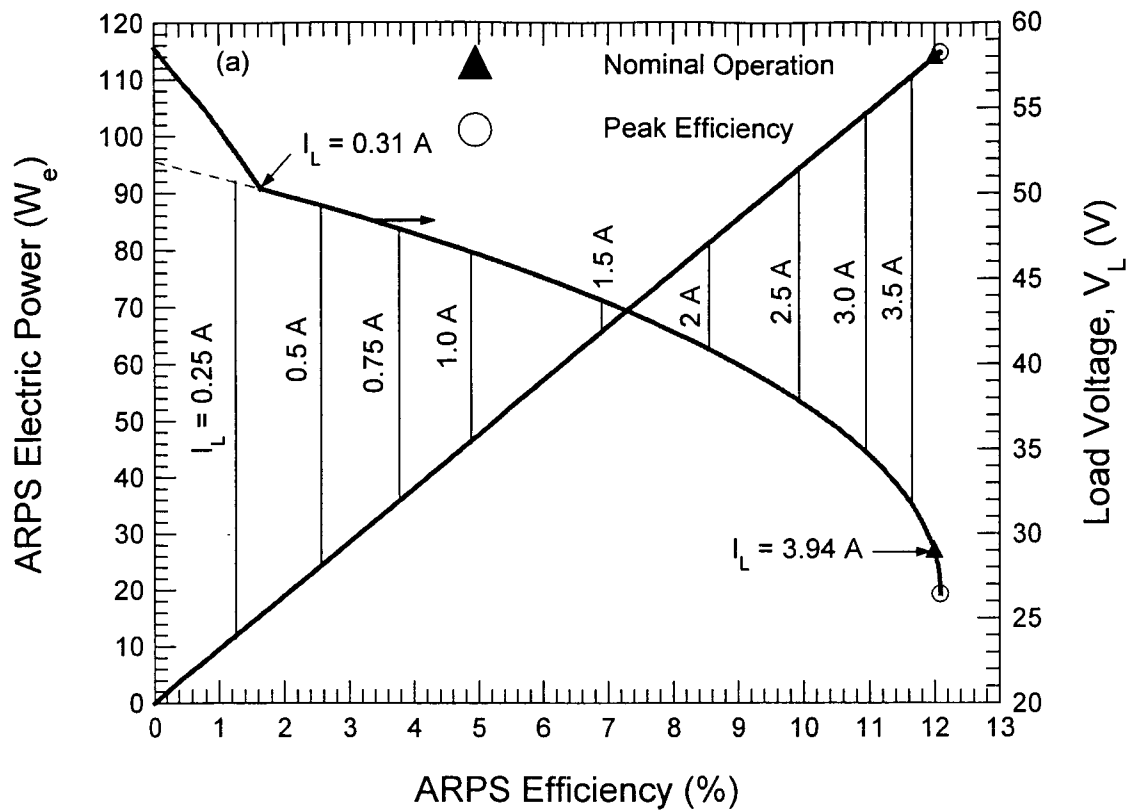


Figure 4-6 Performance Results of the Present CTM-ARPSs.

## 4.5 Performance Results

The performance results in Table 4-1 indicate that the CTM with CTE of the configuration in Figure 4-2c has the highest specific power (212.5 W<sub>e</sub>/kg) and power density (1112 kW<sub>e</sub>/m<sup>3</sup>), followed by that with the CTE of the configurations in Figure 4-2b (176.1 W<sub>e</sub>/kg and 970 kW<sub>e</sub>/m<sup>3</sup>) and in Figure 4-2a (82.4 W<sub>e</sub>/kg and 563 kW<sub>e</sub>/m<sup>3</sup>). However, in terms of the highest heat rejection temperature and hence, the smallest radiator area and mass the best is the CTM with CTE of the configuration in Figure 4-2b (478.5 K), followed by that with CTE of the configurations in Figure 4-2a (461.4 K) and Figure 4-2c (431.5 K). Estimates of the total mass of the ARPSs with each of the three CTE configurations investigated in this work (Figure 4-2) are compared in Table 4-2.

Table 4-2 Mass and Performance Comparisons of CTM-ARPSs with SOA-RTG.

Parameter	SOA-RTG	CTM-ARPSs		
		CTE (Figure 4-2a)	CTE (Figure 4-2b)	CTE (Figure 4-2c)
<b>Operation Parameters:</b>				
GHPS Surface Temperature (K)	1345	1345	1345	1345
Collector Temperature (K)	1306	1305	1305	1305
Hot Junction Temperature (K)	<b>1273</b>	<b>1273</b>	<b>1273</b>	<b>1273</b>
Cold Junction Temperature (K)	560	476.4	493.5	446.5
Heat Rejection Temperature (K)	533	461.4	478.5	431.5
Number of GHPS Bricks	<b>7</b>	<b>4</b>	<b>4</b>	<b>4</b>
BOM Thermal Power (W <sub>th</sub> )	1750	1000	1000	1000
Thermal Efficiency (%)	90	95	95	95
Electrical Losses (%)	10.0	5.0	5.0	5.0
Converter Efficiency (%)	<b>7.41</b>	<b>12.02</b>	<b>11.99</b>	<b>12.02</b>
System Efficiency (%)	<b>6.00</b>	<b>10.85</b>	<b>10.82</b>	<b>10.85</b>
BOM System Power (W <sub>e</sub> )	<b>105.0</b>	<b>108.5</b>	<b>108.2</b>	<b>108.5</b>
<sup>238</sup> PuO <sub>2</sub> Fuel (kg)	<b>4.2</b>	<b>2.4</b>	<b>2.4</b>	<b>2.4</b>
<b>ESTIMATES:</b>				
Radiator Aluminum Fins (kg)	0.712	0.597	0.406	1.022
GHPS with <sup>238</sup> PuO <sub>2</sub> Fuel (kg)	10.11	5.78	5.78	5.78
Aluminum Housing (kg)	2.75	0.975	0.975	0.975
Thermoelectric Materials (kg)	0.485	1.385	0.647	0.537
Converters w/o TE Material (kg)	5.87	3.436	3.436	3.436
Other Structure (kg)	2.0	1.080	1.080	1.080
<b>Total ARPS Mass (kg)</b>	<b>21.936</b>	<b>13.253</b>	<b>12.324</b>	<b>12.83</b>
<b>ARPS Sp. Power (W<sub>e</sub>/kg)</b>	<b><u>4.786</u></b>	<b><u>8.19</u></b>	<b><u>8.78</u></b>	<b><u>8.46</u></b>
<b>Normalized Sp. Power</b>	<b><u>1.0</u></b>	<b><u>1.71</u></b>	<b><u>1.83</u></b>	<b><u>1.77</u></b>

## 4.6 Nominal Electric Power and Efficiency

Figure 4-6a plots the electric power and the load voltage,  $V_L$ , of the CTM-ARPS with CTMs composed CTEs of the configuration in Figure 4-2b versus the ARPS's efficiency. Also indicated in this figure are the load currents,  $I_L$ . The peak and nominal efficiency are indicated by the open circle and closed triangle symbols. The CTM-ARPS whose performance results are presented in Figure 4-6a is favored for having the highest heat rejection temperature (478.5 K), hence the smallest radiator fins and mass. In fact, the dimensions of the aluminum fins are the smallest of all three CTM-ARPSs and are significantly smaller than those of the SOA-RTG, for almost the same BOL nominal electrical power of (Table 4-2 and Figure 4-8). As indicated in Figure 4-6a, nominal efficiency and load voltage the of CTM-ARPS's are slightly lower than their peak values in order to satisfy the conditions of having four parallel strings with a nominal load voltage  $\geq 28$  VDC and nominal EOL electric power of  $\geq 105$   $W_e$ . The latter is necessary to ensure a nominal electric power of at least 100  $W_e$  at the end of a 7-8 year mission.

The nominal load current of the CTM-ARPS with the CTCs comprised of CTEs in Figure 4-6a is 3.94 A; however, decreasing the load current causes the load voltage to increase and both the efficiency and the system's electric power to decrease. As indicated earlier, the load voltage and current depend on those of the uncouple in the top and bottom arrays in CTMs (Figure 4-4). For these converters, the Voltage-Current (V-I) characteristic decrease linearly from the open circuit voltage, at zero current, to zero load voltage, at the short circuit current. The CTMs are load-following up to the peak electric power, which happens to occur at almost the same load current as the peak efficiency, meaning that an increase in the load current would result in an increase in the ARPS's electric power. When the load current reaches 0.31 A, the bottom arrays (Figure 4-4) reaches its open circuit voltage, thus at a lower load current the load voltage of the ARPS is the same as that of the top arrays, which reaches 58.5 VDC at open circuit conditions (or zero load current) (Figure 4-6a). This figure also shows that as the load current increases, the electrical power of the CTM-ARPS increases linearly with its conversion efficiency up to the peak efficiency. Increasing the load current beyond that at peak efficiency would cause both the electric power and efficiency of the ARPS to decrease. Therefore, operating CTM-ARPS at a current beyond that at the peak efficiency should be avoided as ARPS becomes non-load following.

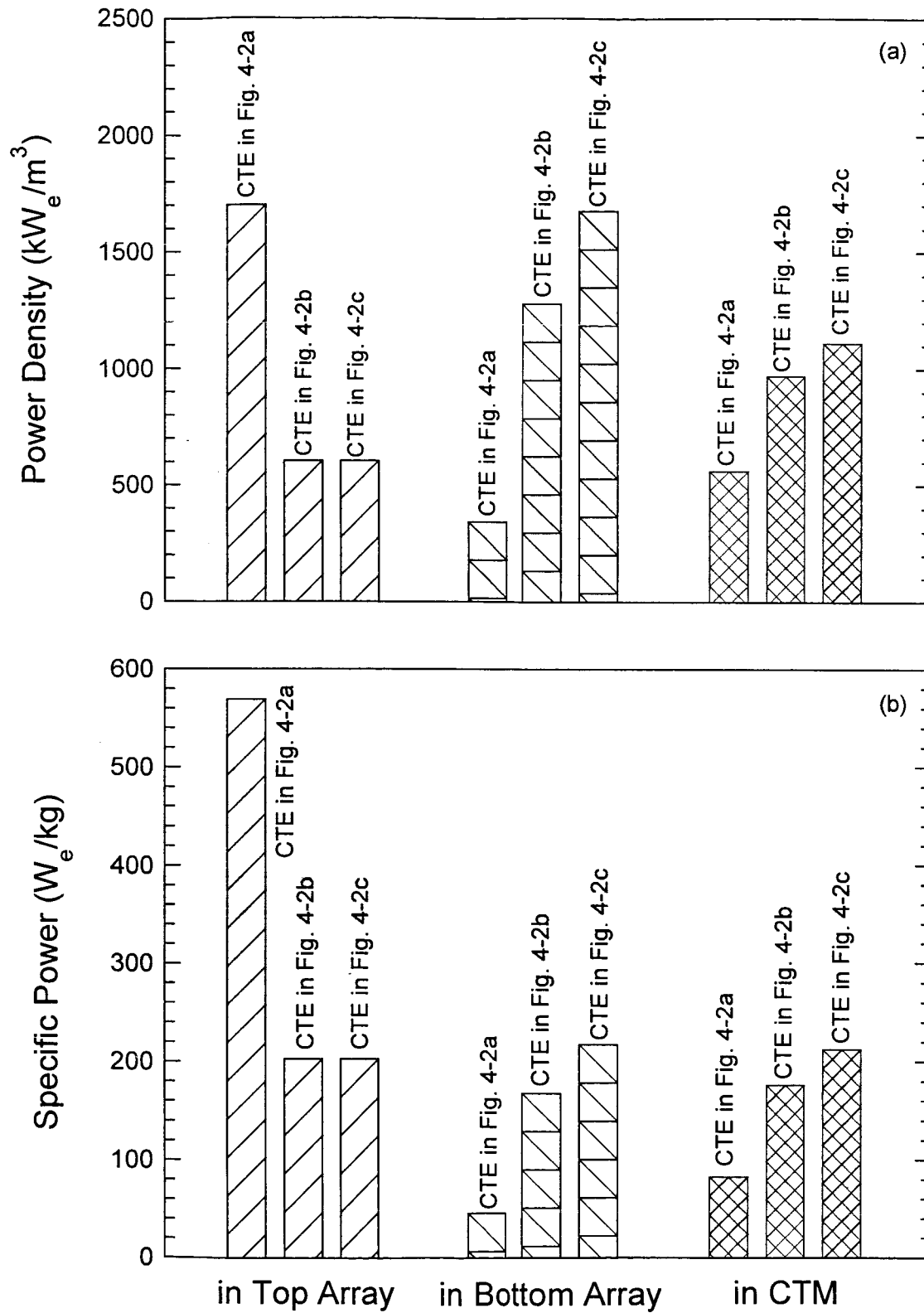


Figure 4-7 Comparisons of Power Density and Specific Power of Thermoelectric Materials.

Figure 4-6b compares the contributions of the top and the bottom arrays in CTMs to the nominal electric power and efficiency of ARPSs. With the CTE configuration in Figure 4-2a, the nominal load current of CTM-ARPS is 3.69 A, which is the sum of those of the top and bottom arrays in CTMs,  $I_T = 1.81$  A and  $I_B = 1.88$  A, respectively. For this CTM-ARPS, the contributions of the top and the bottom arrays to either the nominal electric power or peak efficiency are 49% and 51%, respectively. The nominal load current and the contributions of the top and the bottom arrays in CTM-ARPSs, with the configurations in Figure 4-2b and Figure 4-2c being identical;  $I_L = 3.94$  A,  $I_T = 1.13$  and  $I_B = 2.81$  A, and their contributions to nominal electric power and conversion efficiency are 29% and 71%, respectively (Figure 4-6b).

#### 4.7 Specific Power and Power Density Comparisons

Figure 4-7a and Figure 4-7b compare the power density and the specific power of the present CTM-ARPSs and of the top and bottom uncouples of the various configurations in Figure 4-2; the values given in these Figures are only for the thermoelectric materials of the uncouples in the top and bottom arrays, excluding any structures. As indicated earlier, the density of the materials of the uncouples in the bottom array of the CTMs (Figure 4-2) is typically 2-3 times that of SiGe in the top uncouples. Because the temperature drop across the top SiGe uncouples in the configuration in Figure 4-2a is highest (493 K, Table 4-1), the contribution to the electrical power generation is higher and so are the specific power and power density of 569.2 W<sub>e</sub>/kg and 1702 kW<sub>e</sub>/m<sup>3</sup>, respectively (Figure 4-7a and Figure 4-7b). With the CTE configurations in Figure 4-2b and Figure 4-2c, the temperature difference across the top SiGe uncouples is only 293 K, decreasing their power density and specific power to 605 kW<sub>e</sub>/m<sup>3</sup> and 202.3 W<sub>e</sub>/kg, respectively. Similarly, as the temperature difference across the uncouples in the bottom array of the CTMs increases, their TE materials power density and specific power increase (Figure 4-7a and Figure 4-7b and Table 4-1). Figure 4-7a and Figure 4-7b also show that the uncouples in the bottom array with the configuration in Figure 4-2c have the highest power density and specific power (1112 kW<sub>e</sub>/m<sup>3</sup> and 212.5 W<sub>e</sub>/kg) followed by those with the configuration in Figure 4-2b (970 kW<sub>e</sub>/m<sup>3</sup> and 176.1 W<sub>e</sub>/kg), then those with the configuration in Figure 4-2a (563 kW<sub>e</sub>/m<sup>3</sup> and 82.4 W<sub>e</sub>/kg).

## 4.8 Mass and Specific Power Estimates for CTM-ARPSs

Table 4-2 compares the estimates of the total mass, nominal peak efficiency, and specific power of the present CTM-ARPSs with CTMs comprised of top and bottom arrays of the CTE configurations in Figure 4-2a, Figure 4-2b, and Figure 4-2c, with those of SOA-RTG for almost the same nominal BOL electric power. This comparison is based on using GPHS bricks with fresh  $^{238}\text{PuO}_2$  fuel, however, in actuality, the GPHS bricks may be stored for a period of time before being integrated into the ARPSs or the RTG at launch. Depending on the length of the storage time, the nominal EOM electric power would be  $< 100 \text{ W}_e$ . In this case, the relative comparison in Table 4-2 is still valid. Because the storage time of the GPHS modules could be as much as several years, it is not taken into account in the present comparisons, but when specified it could be easily accounted for in the design and optimization of CTMs for CTM-ARPSs.

The current CTM-ARPSs are designed to provide at least  $100 \text{ W}_e$  nominal at the end of 6-7 year mission. As indicated in Table 4-2, for the nominal EOM electric power of  $100 \text{ W}_e$ , the number of GPHS bricks needed by CTM-ARPSs is only 4, compared to 7 bricks for SOA-RTG. The BOL electric power for the former is  $108 \text{ W}_e$  and for the latter is only  $105 \text{ W}_e$ . Therefore, with 7 bricks, the SOA-RTG is capable of providing an EOM nominal power of  $100 \text{ W}_e$  but for shorter 4-5 year missions. The fewer GPHS bricks in CTM-ARPSs represent a net saving of  $\sim 43\%$  in the amount of the  $^{238}\text{PuO}_2$  fuel needed. As indicated in Figure 4-8 the total height of CTM-ARPSs with only 4 GPHS bricks is 63% and the length of the aluminum fins for heat rejection is 57% of those of SOA-RTG with 7 GPHS bricks ( $L_1 = 433.54 \text{ mm}$  and  $L_2 = 371.6 \text{ mm}$ , respectively). The outer diameter of all three ARPS in Figure 4-8 is the same as SOA-RTG (217.93 mm). The width of the aluminum fins of CTM-ARPS in Figure 4-8c is the smallest; it is 21% larger than the SOA-RTG ( $L_3 = 101.6 \text{ mm}$ ). CTM-ARPS in Figure 8d has the widest aluminum fins, which are 2.72 times those of the SOA-RTG.

Because of the lower specific power of CTMs and their lower heat rejection temperatures (Table 4-1), the mass of both the thermoelectric materials and aluminum fins of the radiator are higher than for SOA-RTG. Such increase in mass is more than compensated for by the lower mass of  $^{238}\text{PuO}_2$  fuel in CTM-ARPSs. As a result, estimates of the specific power for CTM-ARPSs are higher than SOA-RTG. CTM-ARPS with the CTMs, in which the unicouples are of the configuration in Figure 4-2b, has the highest specific power of  $8.8 \text{ W}_e/\text{kg}$ ; 83% increase over

that for SOA-RTG (4.786 W<sub>e</sub>/kg). The second best is CTM-ARPS with CTMs in which the unicouples are of the configuration in Figure 4-2c, whose specific power (8.46 W<sub>e</sub>/kg) is 77% higher than that of SOA-RTG. CTM-ARPS with CTMs in which the unicouples are of the configuration in Figure 4-2a has the lowest specific power of ~8.2 W<sub>e</sub>/kg; nonetheless it is 71% higher than that of SOA-RTG.

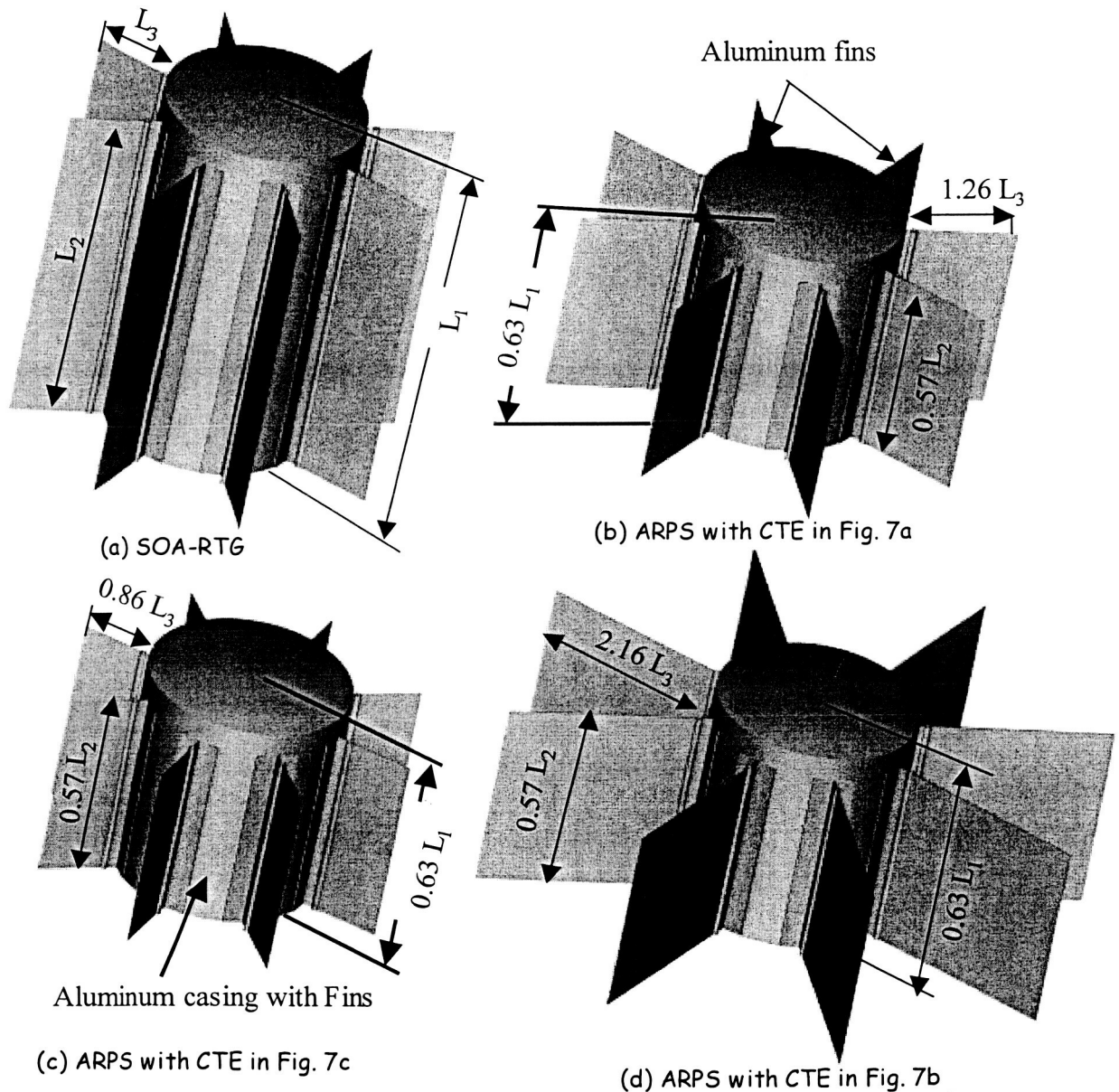


Figure 4-8 Pictorial Views of the Present CTM-ARPSs and a SOA-RTG.

Based on the estimates in Table 4-2, the advantage of employing CTMs in ARPSs is that they provide significant reduction in the amount of the <sup>238</sup>PuO<sub>2</sub> fuel and increase in the system's



specific power for lower mission cost. The net saving in the former is 42.9%, while the increase in the latter could be as much as 83%, in comparison to SOA-RTG. In addition, scaling the current CTM-ARPS to higher power levels is simply a matter of staking additional GPHS bricks/CTMs units. Based on the current CTM-ARPS design, each unit consisting of a GPHS brick and eight CTMs (Figure 4-1) generates a nominal EOM power of 25  $W_e$ . Therefore, for a nominal EOM power of 450  $W_e$ , a total of 18 GPHS bricks/CTMs units are needed. This electric power is  $\sim 50\%$  higher than that of the SOA-RTG with the same number of GPHS bricks (270 – 290  $W_e$ ).

Another advantage of the present CTM-ARPS is their small volume (Figure 4-8) for reduced mission cost and better integration into the spacecraft. Owing to the relatively moderate rejection temperature of these CTM-ARPSs, some of the rejected thermal power could be used for thermal management of instrumentation and science payloads aboard the spacecraft, thus increasing the energy utilization of CTM-ARPSs beyond their conversion efficiency. Figure 4-8 presents pictorial comparison of the dimensions of CTM-ARPSs and SOA-RTG for nominal EOM power of 100  $W_e$ .

Although the saving in the  $^{238}\text{PuO}_2$  fuel in the present CTM-ARPS is not as much as it would be with dynamic Free-Piston Stirling Engines (FPSEs), which have a rated efficiency currently of 22%, the specific power of the CTM-ARPSs is about twice that of an ARPS with two, 55  $W_e$  FPSEs (4.2  $W_e/\text{kg}$ ) (Thieme and Schreiber 2004). In addition, using CTEs of materials with known properties and very successful past performance and flight experience, such SiGe, TAGS-85, and 2N-PbTe, which cause no electromagnetic interference with the spacecraft are added advantages to the CTMs for ensuring the success and minimizing technology risk in future missions with CTM-ARPSs. The skutterudites in the bottom uncouples in the CTE with the configurations in Figure 4-2b and Figure 4-2c are very promising, currently at TRL-3 and being advanced to TRL-5 that is expected to be achieved in the next 2-3 years. These materials have demonstrated performance and well-documented properties up to 973 K and the technology of making segmented n- and p-legs with minimal interfacial resistances has been demonstrated (Caillat, Fleurial and Borshchevsky 1997, Caillat et al. 1999 and 2000, and El-Genk, Saber and Caillat 2002). Remaining issues include the development and application of sublimation suppression coating of Antimony in the n- and p-legs near the hot junction, demonstrating the

manufacturing capability of the CTMs, verifying lifetime performance, and identifying potential integration issues.

## 4.9 Summary

Cascaded thermoelectric modules (CTMs) with three configurations and different arrangements have been developed, optimized for maximum efficiency, and integrated into ARPSs with 4-GPHS bricks loaded with fresh  $^{238}\text{PuO}_2$  fuel. All CTMs use SiGe unicouples in the top arrays, but different thermoelectric materials for the unicouples in the bottom arrays. For the latter, three options have been investigated, using off-the-shelf thermoelectric materials and high FOM skutterudites, namely: (a) p-legs of TAGS-85 and n-legs of 2N-PbTe; (b) p-legs of  $\text{CeFe}_{3.5}\text{Co}_{0.5}\text{Sb}_{12}$  and n-legs of  $\text{CoSb}_3$ ; and (c) segmented p-legs of  $\text{CeFe}_{3.5}\text{Co}_{0.5}\text{Sb}_{12}$  and  $\text{Zn}_4\text{Sb}_3$  and n-legs of  $\text{CoSb}_3$ . The lengths of the top SiGe and bottom unicouples is the same (10 mm), but the cross-sectional areas of the n- and p-legs are optimized for maximum efficiency for constant input power from the GPHS bricks, a SiGe nominal hot junction temperature of 1273 K, and ARPS thermal efficiency of 95% and electrical losses of 5%. The unicouples in the top and bottom arrays of CTMs are thermally, but not electrically, coupled. Thus, the thermal power rejected by the top SiGe array is the same as the input thermal power to the bottom array of the CTM. The hot junction temperature for the latter is kept constant at 15 K lower than the cold junction of the SiGe unicouples in the top array. The heat rejection temperature of the aluminum casing of CTM-ARPS is also taken 15 K lower than the cold junction temperature of the bottom unicouples. The dimensions of the aluminum fins for rejecting the thermal load are calculated and their masses included in the mass estimates of CTM-ARPSs.

The estimate of the nominal efficiency of CTEs with the different configurations is  $\sim 12\%$  and that of CTM-ARPSs is 10.85%, compared to 9.1% to 9.5% for the SiGe unicouples when operating at the same hot junction and rejection temperatures, and  $\sim 7.4\%$  for the SOA-RTG. The high efficiency of CTM-ARPSs requires only 4 GPHS bricks for nominal BOM and EOM electrical power of 108  $W_e$  and 100  $W_e$ , respectively, versus 7 GPHS bricks for SOA-RTG for almost the same nominal powers. The specific power of the SiGe material is higher than those of the thermoelectric materials of the unicouples in the bottom array of the CTMs. Also, the lower heat rejection for CTMs, compared to that of SOA-RTG, increases the mass of the radiator. However, the fewer number of the GPHS bricks needed by CTM-ARPSs more than compensates

for such mass increases. As a result, the estimated specific powers of the present CTM-ARPSs are 71% to 83% higher than SOA-RTG.

In summary, the advantages of employing CTM-ARPSs are the significant reduction in the amount of the  $^{238}\text{PuO}_2$  fuel and the higher specific power for lower mission cost. In addition, using CTMs of materials with known properties and very successful past performance and flight experience, such SiGe, TAGS-85, and 2N-PbTe, and the absence of any electromagnetic interference with the spacecraft are major advantages for ensuring the success and minimizing risk of future missions. The skutterudites materials of the unicouples employed in two of the three CTE configurations investigated are very promising, currently at TRL-3 and being advanced to TRL-5 that could be achieved with the next 2-3 years. These materials have well-documented properties and demonstrated performance up to 973 K and the technology of making segmented n- and p-legs with minimal interfacial resistances is well at hand. Remaining issues, however, include the development and application of sublimation suppression coating of the Antimony from the n- and p-legs near the hot junction, demonstrating the capability for manufacturing CTMs, and verifying the lifetime performance and integration issues. In conclusion, CTM-ARPSs have a very promising potential for enabling future missions at a significant reduction in cost and in the amount of  $^{238}\text{PuO}_2$  fuel.

## 5 PERFORMANCE TESTS OF SKUTTERUDITES-BASED SEGMENTED AND NON-SEGMENTED THERMOELECTRIC UNICOUPLES (UNM-ISNPS)

This chapter presents results of three performance tests of skutterudites-based Segmented Thermoelectric (STE) and non-segmented unicouples performed at average hot and cold junction temperatures of  $\sim 973$  K and 300 K, respectively, to verify theoretical predictions. The first two tests (MAR-03 and JUN-03) involved non-segmented unicouples of slightly different dimension but same materials for the n- ( $\text{CoSb}_3$ ) and p- ( $\text{CeFe}_{3.5}\text{Co}_{0.5}\text{Sb}_{12}$ ) legs. The test duration for MAR-03 is 450 hours and 1200 hours for JUN-03. The third test (JUL-03) is of a skutterudites-based Segmented uncouple, in which the p-leg has two segments of  $\text{CeFe}_{3.5}\text{Co}_{0.5}\text{Sb}_{12}$  and  $\text{Bi}_{0.4}\text{Sb}_{1.6}\text{Te}_3$  and the n-leg has two segments of  $\text{CoSb}_3$  and  $\text{Bi}_2\text{Te}_{2.95}\text{Se}_{0.05}$ . The segments in the n- and p-legs have different lengths and cross-sectional areas. The test duration for JUL-03 is 645 hours. All tested unicouples are fabricated at JPL and assembled and tested in the vacuum facility at the University of New Mexico in argon gas at  $\sim 0.051$  to  $0.068$  MPa to suppress the sublimation of antimony from the legs near the hot junction. Detailed measurements of the open circuit voltage, voltage across the n- and p-legs, the voltage-current (V-I) characteristics, and the hot and cold junction temperatures are performed in all tests. In JUL-03, additional measurements of the interfacial temperatures and the voltage across the segments in the n- and p-legs are obtained as functions of test duration. Estimates of beginning-of-life (BOL) conversion efficiencies of 10.7% for skutterudites-based non-segmented and 13.5% for STE unicouples are within 10% of theoretical predictions assuming zero side heat losses. Estimates of side heat losses in the tests are  $2.3 W_{\text{th}}$  in MAR-03 to  $9.3 W_{\text{th}}$  in JUL-03, causing the actual efficiencies in the tests to be  $\sim 40$ -50% lower. Because cross sectional areas of the legs in JUL-03 are much larger than in both MAR-03 and JUN-03, the measured BOL peak electrical power is  $1.295 W_e$  versus  $0.671 W_e$  for the latter.

### 5.1 Introduction

State-Of-The-Art (SOA) Radioisotope Thermoelectric Generators (RTGs) with SiGe thermoelectric converters had successfully served the U.S. space exploration program for more than three decades (Carpenter 1970, Schock 1980, and Bennett, Lombardo and Rick 1987).

However, in order to reduce the cost of future deep space missions and the amount of  $^{238}\text{PuO}_2$  fuel needed, the current emphases for developing Advanced Radioisotope Power Systems (ARPSs) are to increase the system's conversion efficiency and decrease the total mass. A desired goal is that for a given electric power, reduce the amount of  $^{238}\text{PuO}_2$  needed by at least 40% and achieve a system specific power that is 50% more or higher than that of SOA RTGs (4.6 W<sub>e</sub>/kg). Realizing these performance goals is possible with the replacement of the SiGe converters in RTGs with more efficient ones, with no or minimal changes in the current RTGs design.

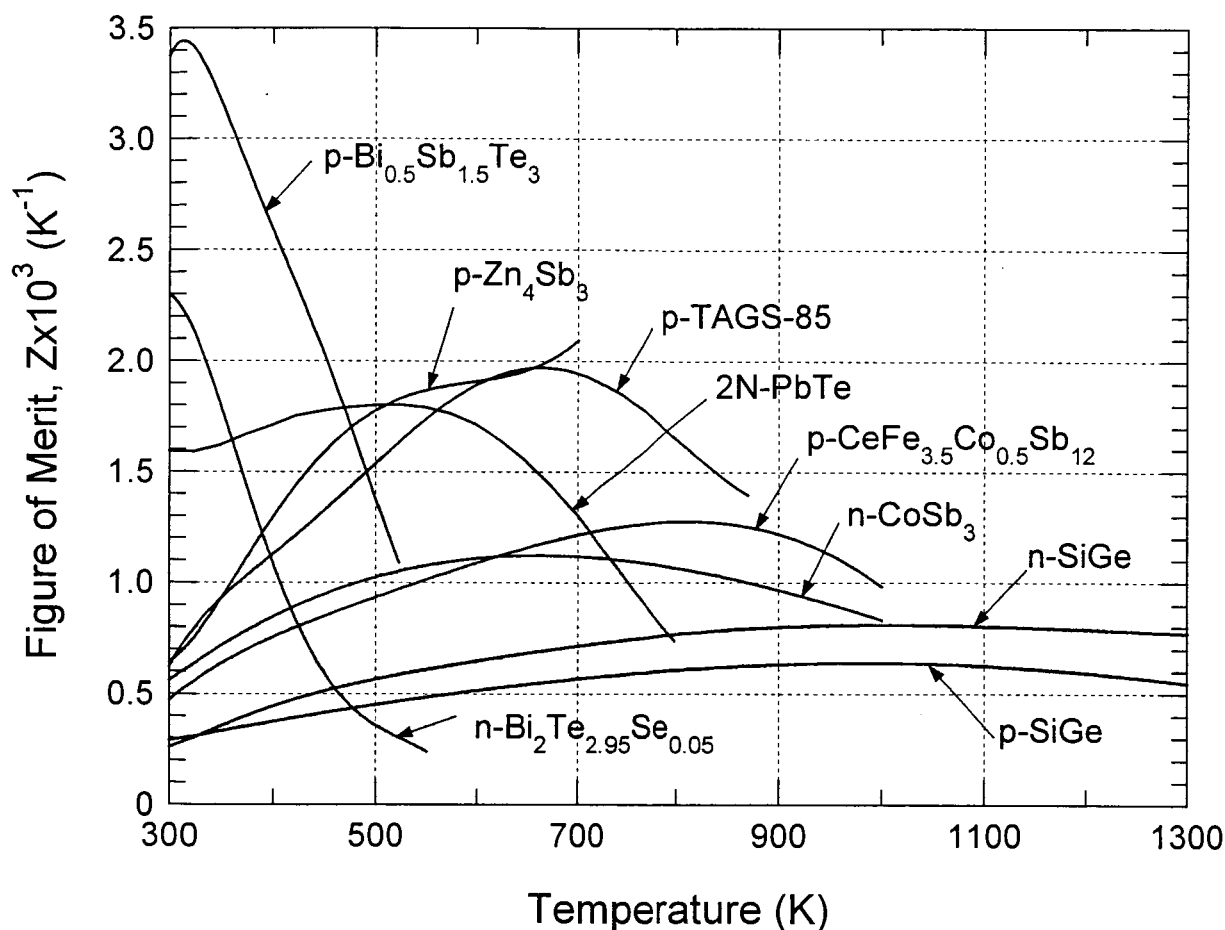


Figure 5-1 FOM for Different TE Materials.

Developing and demonstrating more efficient thermoelectric converters to enable ARPS's conversion efficiency of  $\geq 8\%$  would halve the amount of  $^{238}\text{PuO}_2$  fuel needed, almost doubling the specific power of the ARPS (El-Genk 2002 and 2003). Such system conversion efficiencies are possible using segmented or non-segmented skutterudites-based thermoelectric converters

(Figure 5-1 and Figure 5-2). Figure 5-1 shows that the skutterudites  $p\text{-Zn}_4\text{Sb}_3$ , and  $p\text{-CeFe}_{3.5}\text{Co}_{0.5}\text{Sb}_{12}$ , with  $n\text{-CoSb}_3$  offer high Figure-Of-Merits (FOMs) in the intermediate temperature range from 500 K to 973 K (Caillat et al. 1997, 1999 and 2000, Fleurial et al. 1996 and 1997). At these temperatures, the conversion efficiency of skutterudites-based segmented thermoelectric uncouples could be  $\sim 9.5\%$ , but when used with segments of  $n\text{-Bi}_2\text{Te}_{2.95}\text{Se}_{0.05}$  and  $p\text{-Bi}_{0.4}\text{Sb}_{1.6}\text{Te}_3$  and operated at hot and cold junction temperatures of 973 K and 300 K, respectively (Figure 5-2), the conversion efficiency could be as much as 14.8%, assuming zero side heat losses (El-Genk, Saber and Caillat 2002 and 2003, El-Genk and Saber 2003, El-Genk 2002 and 2003). In an optimized STE uncouple, the  $\text{Bi}_2\text{Te}_{2.95}\text{Se}_{0.05}$  and  $\text{Bi}_{0.4}\text{Sb}_{1.6}\text{Te}_3$  segments at the cold junction in the n- and p-legs, respectively, operate between  $\sim 450$  and  $\sim 300$  K. The intermediate segments near the hot junction in the p-leg are  $\text{Zn}_4\text{Sb}_3$  and  $\text{CeFe}_{3.5}\text{Co}_{0.5}\text{Sb}_{12}$ , respectively, while the n-leg has only one segment of  $\text{CoSb}_3$  (Figure 5-2).

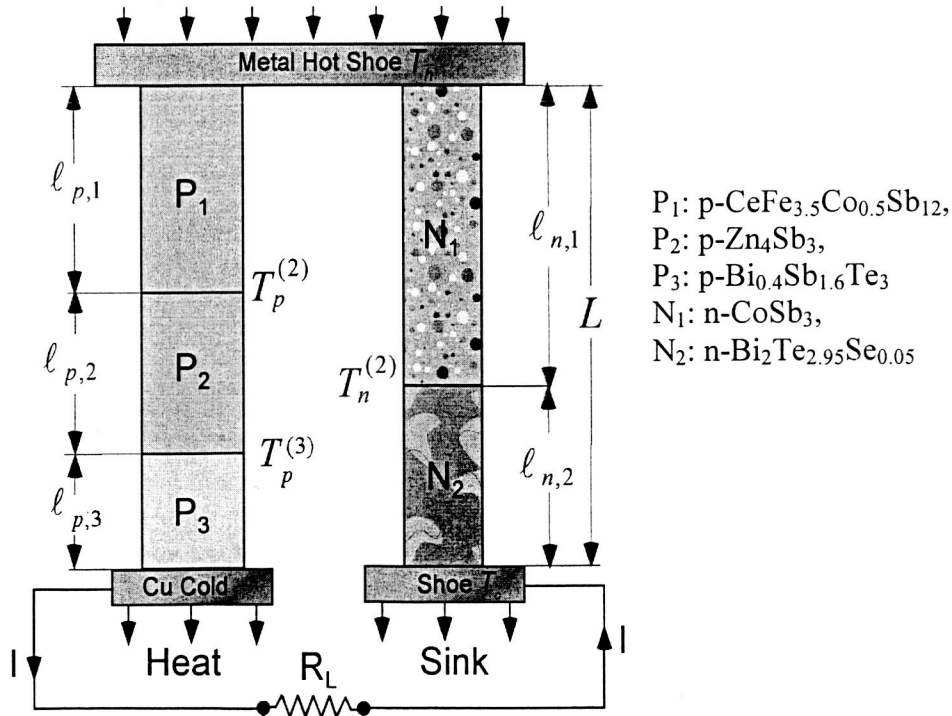


Figure 5-2 STE Converter for  $T_c = 300$  K.

In order to maximize the performance of a STE uncouple the segments in the n- and p-legs (Figure 5-2), each is designed to operate in the temperature ranges in which the material of the segment has the highest FOM (Figure 5-1). The segments in the n- and p-legs should have minimal interfacial thermal and electrical resistances and material diffusion across the interfaces. In addition, it is preferable that the segments have similar coefficients of thermal expansion to

minimize thermal stresses in the legs during operation. The appropriate materials of the segments in the n- and p-legs are easily identified in Figure 5-1. The dimensions (cross sectional area and length) and number of the segments in each leg and the interfacial temperatures could be optimized either for maximizing efficiency or electrical power density of the STE converter (El-Genk, Saber and Caillat 2002 and 2003, and El-Genk and Saber 2003).

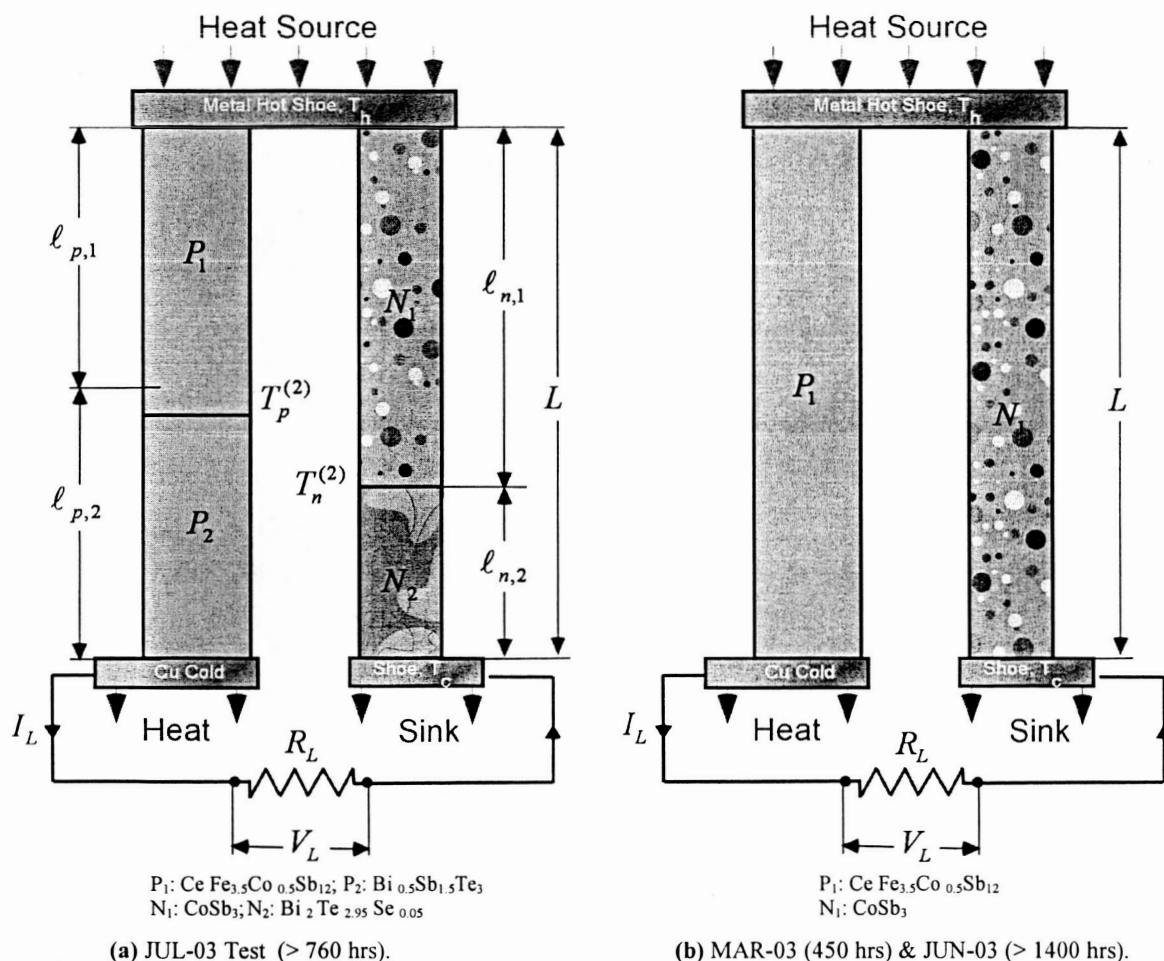


Figure 5-3 Segmented and Non-segmented Skutterudites-Based Unicouples in Performance Tests Performed at the University of New Mexico.

In a joint program with Jet Propulsion Laboratory (JPL), California Institute of Technology in Pasadena, California, performance tests of segmented and non-segmented skutterudites-based unicouples (Figure 5-3a and Figure 5-3b) are carried out at both organizations to verify Beginning-of-Life (BOL) theoretical predictions. The tests are conducted both in vacuum and in argon cover gas (0.051 - 0.068 MPa) at average hot and cold junction temperatures of 973 K and 300 K, respectively. A number of unicouples with p-legs made of  $\text{CeFe}_{3.5}\text{Co}_{0.5}\text{Sb}_{12}$  and n-legs of  $\text{CoSb}_3$  have been tested for 10's to 100's of hours (Figure 5-3b). In addition, performance

tests of a number of unicouples, in which the p-leg has two segments of  $\text{CeFe}_{3.5}\text{Co}_{0.5}\text{Sb}_{12}$  and  $\text{Bi}_{0.4}\text{Sb}_{1.6}\text{Te}_3$  and the n-leg has two segments of  $\text{CoSb}_3$  and  $\text{Bi}_2\text{Te}_{2.95}\text{Se}_{0.05}$  (Figure 5-3a) are performed at same average temperatures both in vacuum and in argon gas.

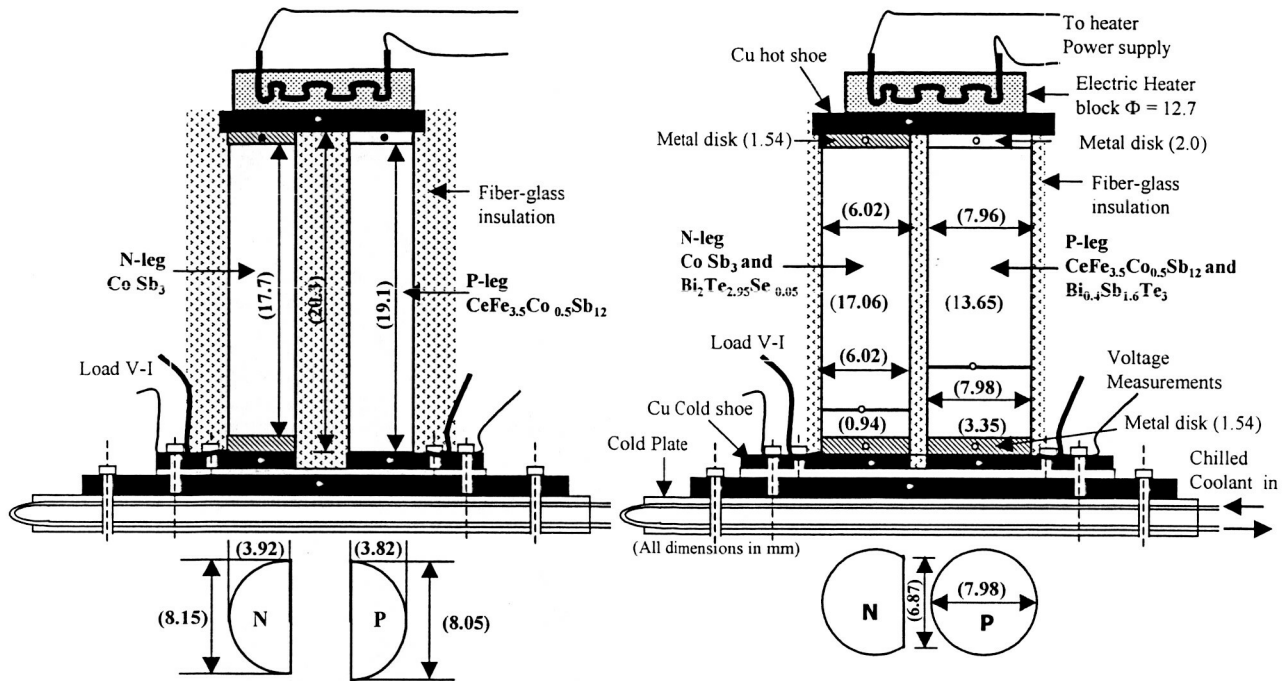
This chapter reports the results of the three performance tests conducted recently in UNM's Institute for Space and Nuclear Power Studies (ISNPS) facility to verify BOL theoretical predictions. Two tests (MAR-03 and JUN-03) involved non-segmented unicouples (Figure 5-3b) and the third test (JUL-03) involved a segmented uncouple (Figure 5-3a). The tests are performed at average hot and cold junction temperatures of 973 K and 300 K, respectively. The following section describes the experimental setup and presents schematics of the unicouples tested.

## 5.2 Experiment Setup

The performance tests of MAR-03, JUN-03 and JUL-03 are performed in argon cover gas at 0.051-0.068 MPa in order to suppress sublimation of antimony (Sb) from the n- and p-legs near the hot shoe. Earlier tests performed in vacuum ( $\sim 10^{-5}$  Pa) showed extensive sublimation of Sb above 600 - 700 K. In MAR-03 (Figure 5-3b and Figure 5-4a), the 17.7 mm long n-leg is made of  $\text{CoSb}_3$  and the 19.1 mm long p-leg is made of  $\text{CeFe}_{3.5}\text{Co}_{0.5}\text{Sb}_{12}$ . The n-leg has 1.2 mm and 1.4 mm thick metal disks at the hot and cold ends, respectively, to facilitate good thermal and electrical contacts with the hot and cold copper (Cu) shoes (Figure 5-4a). The p-leg has 1.2 mm metal disk at the hot end for the same purpose, but none at the cold end. The total length of the legs in MAR-03 is 20.3 mm, and both legs are soldered to the Cu cold shoe (Figure 5-4a); the hot shoe is a Cu disk, 12.2 mm in diameter and 2.86 mm thick. Good solid-solid contact is maintained between the hot shoe and both n- and p-legs in the tests using four compression springs (Figure 5-4a and Figure 5-5a). These springs also accommodate the expansion of the legs during testing at hot junction temperatures up to 973 K. The hot shoe is heated using an electric heater to which the input power is continuously regulated to maintain a constant hot junction temperature. The fully assembled test section is surrounded with fiberglass insulation to reduce side heat losses in the tests (Figure 5-4a and Figure 5-5a). The rejected thermal power by the uncouple to the cold shoe is removed using a chilled coolant (50% Ethylene Glycol and 50% distilled water) circulating through an underlying aluminum cold plate (Figure 5-4a). The experimental set up for JUN-03 is identical to that of MAR-03, the n- and p-leg materials (Figure



5-3b) are the same, but the dimensions of the legs are slightly different. The experimental setup for JUL-03 is slightly different, but designed to maintain the same test conditions.



(a) A Schematic of MAR-03 Skutterudites Unicouple.

(b) A Schematic of JUL-03 Segmented Unicouple.

Figure 5-4 Schematics of MAR-03 and JUL-03 Unicouples Tested at the UNM-ISNPS Facility.

Figure 5-4b shows a schematic of JUL-03 unicouple tested. The materials in the top segments in the n- and p-legs are the same as in the n- and p-legs of MAR-03 and JUN-03. The lower segments in the legs of JUL-03 are bismuth telluride alloys (Figure 5-3a and Figure 5-4b) and have different lengths in order to maximize the efficiency of the STE unicouple. The legs in JUL-03 have larger cross-sectional areas than both MAR-03 and JUN-03 (Figure 5-4a), to increase the electrical power and the load current; both legs in JUL-03 have thin metal disks at the hot and cold shoes to establish good solid-solid contact with the hot and cold shoes. In this unicouple, the temperature measurements recorded not only of the hot and cold shoes but also of the interfaces of the segments in the legs. The K-type thermocouples used for temperature measurements are indicated in Figure 5-4a and Figure 5-4b with white and black dots. In addition, the voltages across the individual segments, legs, and the JUL-03 unicouple are measured in open circuit and while sweeping the V-I characteristics. Tests are conducted at an average hot and cold junction temperatures of  $\sim 973$  K and  $\sim 300$  K respectively, which are maintained almost constant using a control program based on the LabView software. Other

measurement in the tests is the power to the electrical heater for the unicouple. The tests are conducted in vacuum-tight bell jars, which are evacuated to  $10^{-5}$ - $10^{-6}$  Pa, before it is backfilled with argon (99.99% pure) to 0.065 MPa to suppress antimony (Sb) sublimation from the legs.

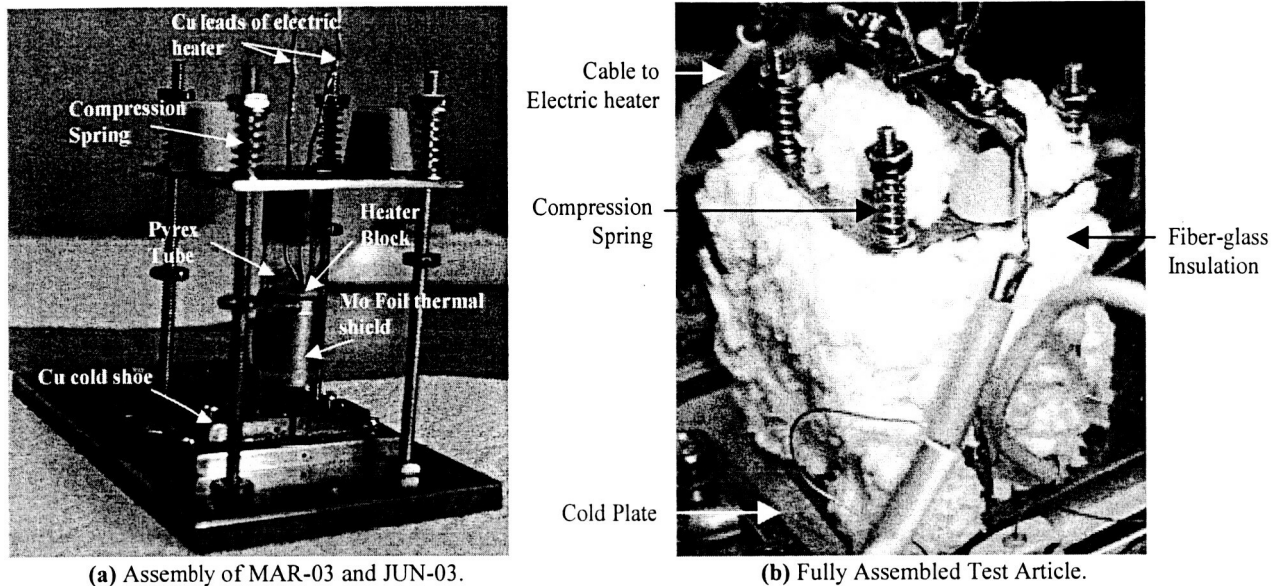


Figure 5-5 Detailed of the Assembled Unicouples in the Tests Performed in the UNM-ISNPS Test Facility.

### 5.3 Tests Histories

Figure 5-6 presents the test histories for MAR-03 and JUL-03 unicouples. The MAR-03 test lasted for 450 hours, of which the cumulative test time at hot and cold junction temperatures of  $973.3 \pm 0.8$  K and  $300.7 \pm 0.4$  K, respectively, is 261 hours (Figure 5-6a). In the test, MAR-03 unicouple is subjected to three startup and two shutdown transients from and to 300 K. The first test period lasted for  $\sim 7$  hours, during which the cold junction is kept at  $\sim 273$  K while increasing the hot junction temperature gradually to 562 K. The test is then terminated for  $\sim 14$  hours due to a disruption in the electric power supply. The second test phase of MAR-03 test lasted for  $\sim 62$  hours, during which the cold junction temperature varied from 273 K - 290 K, while the hot junction temperature is increased gradually to 823 K and kept constant for  $\sim 40$  hours. The hot junction temperature is then decreased to 640 K and held constant for 24 hours before it is increased again to  $\sim 973$  K. At this temperature and an average cold junction temperature of 300 K, additional testing of MAR-03 lasted for 45 hours before being terminated for the second time. After MAR-03 unicouple is cooling down to  $\sim 300$  K, the hot junction

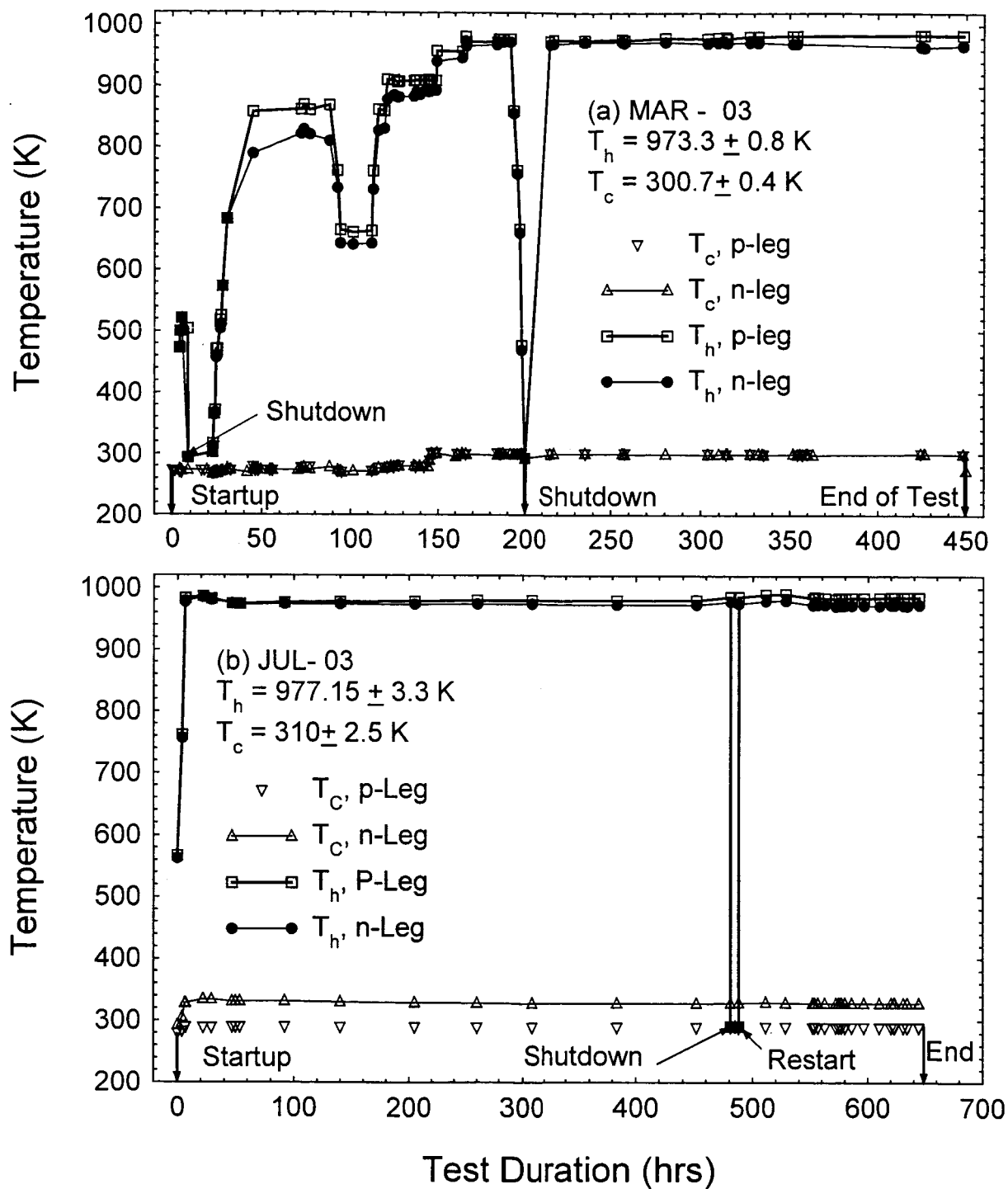


Figure 5-6 Testing Histories for MAR-03 and JUL-03 Uncouples.

temperature is increased faster than in previous startup transients to  $973 \pm 0.8 \text{ K}$  and held constant for the remainder of the test period.

The cumulative test duration for JUN-03 at average hot and cold junction temperatures of 973 K and 300 K, respectively, is 1200 hours; the longest of all three tests performed in this work. The test history for JUL-03, delineated in Figure 5-6b, includes only one, relatively rapid cool down for a brief period ( $\sim 15$  hours) to add more fiberglass insulation, particularly to the sides of the n-leg, followed by a rapid restart to constant hot and cold junction temperatures of  $977.15 \text{ K} \pm 3.3 \text{ K}$  and  $310 \pm 2.25 \text{ K}$ , respectively, through the end of the testing period. At these temperatures, the cumulative test time of JUL-03 uncouple is 645 hours. As indicated earlier, and shown in the next section, the measured peak electrical power and the corresponding load current for JUL-03 are more than double those for MAR-03 and JUN-03, because of the much large cross-section area of the legs in the former.

## 5.4 Results and Discussion

The measured open circuit voltage ( $V_{oc}$ ) and V-I characteristics of the three uncouples tested in this work are used to obtain best estimates BOL effective resistance of the thermoelectric materials and the contact resistances of the legs, side heat losses in the tests, and conversion efficiency and load electric power. The estimates of the conversion efficiencies are based on the measured resistances of the legs, but assume zero side heat losses in order to compare with theoretical predictions. These estimates should be close to those of the uncouple in an actual space power system, in which thermal insulation is quite effective, thus should be considered as upper bound estimates. On the other hand, the actual efficiency and electrical power output in the tests are lower because of the side heat losses, which is setup dependent, thus should be considered as lower bound estimates. The estimates of the side heat losses in the tests are based on the difference between the estimated assuming zero side heat losses, and measured values of the open circuit voltage; more details are presented later in the chapter.

In MAR-03, the load voltage is measured, but not that of the n- and p-leg separately. Although the BOL contact resistances for the n- and p-legs may be different, they are assumed the same and equal half the estimated total contact resistance in the uncouple ( $350 \mu\Omega\text{-cm}^2$  per leg). In JUN-03 and JUL-03, the measured I-V characteristics of the individual legs are used to obtain estimates of the BOL contact resistance and of the total resistances of the n- and p-legs. Estimates of the contact resistances are reported only at BOL where the changes in the thermoelectric properties of the materials in the n- and p-legs are expected to be minimal.

For JUL-03, the estimates of the contact resistances for the n- and p-legs is  $450.6 \mu\Omega\text{-cm}^2$  and  $110.4 \mu\Omega\text{-cm}^2$ , respectively. At other times in the tests, the estimates of the changes in the total resistance of the legs include those occurring in the contact resistances and in the resistivities of the thermoelectric materials. Contact resistances, particularly at the hot shoe could have increased with test duration and so are those of the thermoelectric properties, which are measured directly in the present tests. The tests are not designed to separately quantify the changes in these resistances with test duration, but rather to generate BOL performance data to compare with theoretical predictions of the peak conversion efficiency and peak electrical power at average hot and cold junction temperatures of 973 K and 300 K, respectively.

## 5.5 V-I Characteristics

Figure 5-7a and Figure 5-7b present the measured V-I characteristics for MAR-03 and JUL-03 uncouples, respectively, at different test times. As indicated in these figures, although there are slight variations in the exact values of the hot and cold junction temperatures in the tests, these temperatures averaged  $973.2 \text{ K} \pm 0.8 \text{ K}$  and  $300.7 \pm 0.4 \text{ K}$  and  $977.15 \pm 3.3 \text{ K}$  and  $310 \pm 2.25 \text{ K}$  for MAR-03 and JUL-03, respectively. The hot and the cold junction temperatures in JUN-03 averaged  $973 \text{ K} \pm 3.4 \text{ K}$  and  $300 \pm 3.2 \text{ K}$ , respectively. The cumulative test time at these temperatures is 258 hrs, 1200 hrs, and 645 hrs for MAR-03, JUN-03 and JUL-03 uncouples, respectively, the longest ever reported for skutterudites-based segmented and non-segmented uncouples. The experimental data presented in Figure 5-7a and Figure 5-7b clearly show that not only the open circuit voltage ( $V_{oc}$ ), but also the slope of the V-I characteristics decreased and increased, respectively, with test duration. Although BOL  $V_{oc}$  and the measured decreases in the value of  $V_{oc}$  for MAR-03 and JUL-03 after the same test duration (237 hrs and 238 hrs, respectively) are almost the same, the change in the slope of V-I characteristics of the latter with test duration is much higher than for the former (Figure 5-7a and Figure 5-7b). Such increase in the slope of the V-I characteristics with test duration is indicative of the increase in the contact resistance or the resistivity of the thermoelectric materials in the n- and p-legs or both.

Similarly, an increase in side heat losses, a decrease in the Seebeck coefficient of the n- and p-leg materials, or both, in the tests could have caused the measured decrease in the open circuit voltage  $V_{oc}$ . Figure 5-7a, shows that despite the decrease in the open circuit voltage for MAR-03

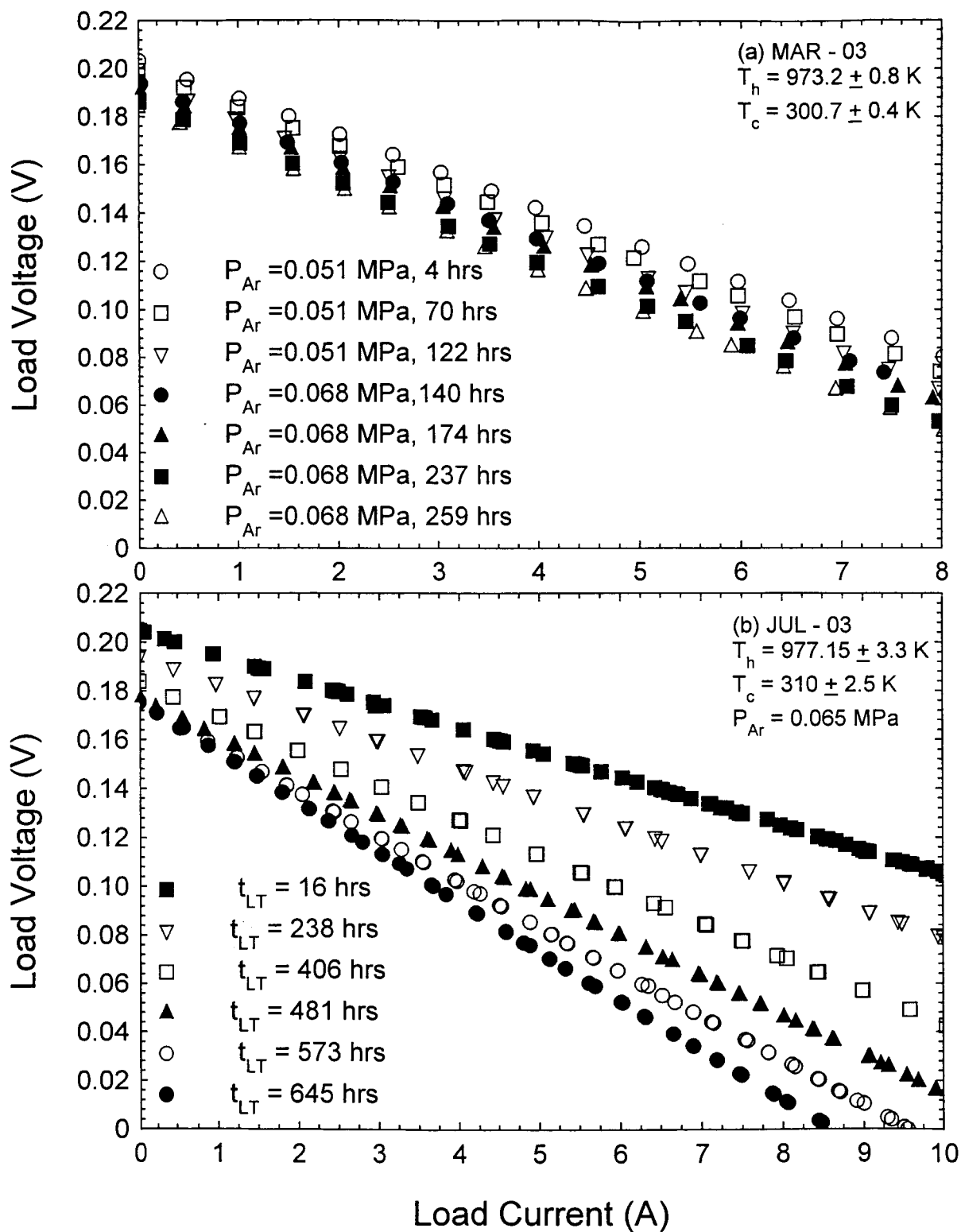


Figure 5-7 Measured V-I Characteristics for Skutterudites (MAR-03) and STE (JUL-03) Uncouples.

with test duration, there is very little increase in the slope of the measured V-I characteristics with cumulative test duration. These results suggest that both the contact resistances in the n- and p-legs and the electric resistivities of the thermoelectric materials in the legs of MAR-03 could have experienced little changes with cumulative test duration (259 hrs). Conversely, the continue decreases that are measured in the slope of the V-I characteristics for JUL-03 are indicative of the increase in the contact resistances and in the electrical resistivities of the thermoelectric materials of the segments in the n- and p-legs (Figure 5-7b). *However, since the skutterudites used in the hot segments in the n- and p-legs of JUL-03 (Figure 5-3a) are the same as those of the n- and p-legs in MAR-03, it may be argued that the measured increase in the slope of the V-I for JUL-03 with test duration could be mostly due to the increase in the contact resistances both at the hot shoe and at the interfaces between the segments (Figure 5-3a and Figure 5-4b).*

Quantifying the changes in the thermoelectric properties of the materials in the n- and p-legs with cumulative test duration in the current tests, although important for determining the actual cause (s) of the measured performance degradation of skutterudites (MAR-03 and JUN-03) and STE (JUL-03) unicouples, it is outside the scope of the present work. The results of the current tests are invaluable to future planning and design of life tests to quantify the performance degradation mechanisms and develop the technology to minimize such degradation for the expected operation life of 7 – 10 years in space nuclear power systems. The primary focus of the present tests is not to quantify the degradation mechanisms and their individual effects, but rather to generate BOL data to compare to theoretical predictions for segmented and non-segmented skutterudites-based unicouples and to provide preliminary input to the planning of subsequent performance tests.

## 5.6 Open Circuit Voltage

Figure 5-8a compares the measured decreases in the open circuit voltage of the three unicouples tested in this work as function of test duration, at almost the same average hot and cold junction temperatures of 973 K and 300 K, respectively. This figure clearly shows the results for all three tests to be very consistent, indicating that  $V_{oc}$  decreased linearly with test duration up to ~450-550 hrs. Beyond that, the decrease in the open circuit voltage became progressively smaller, approaching an asymptote of 84% to 86% of BOL value for JUN-03 and

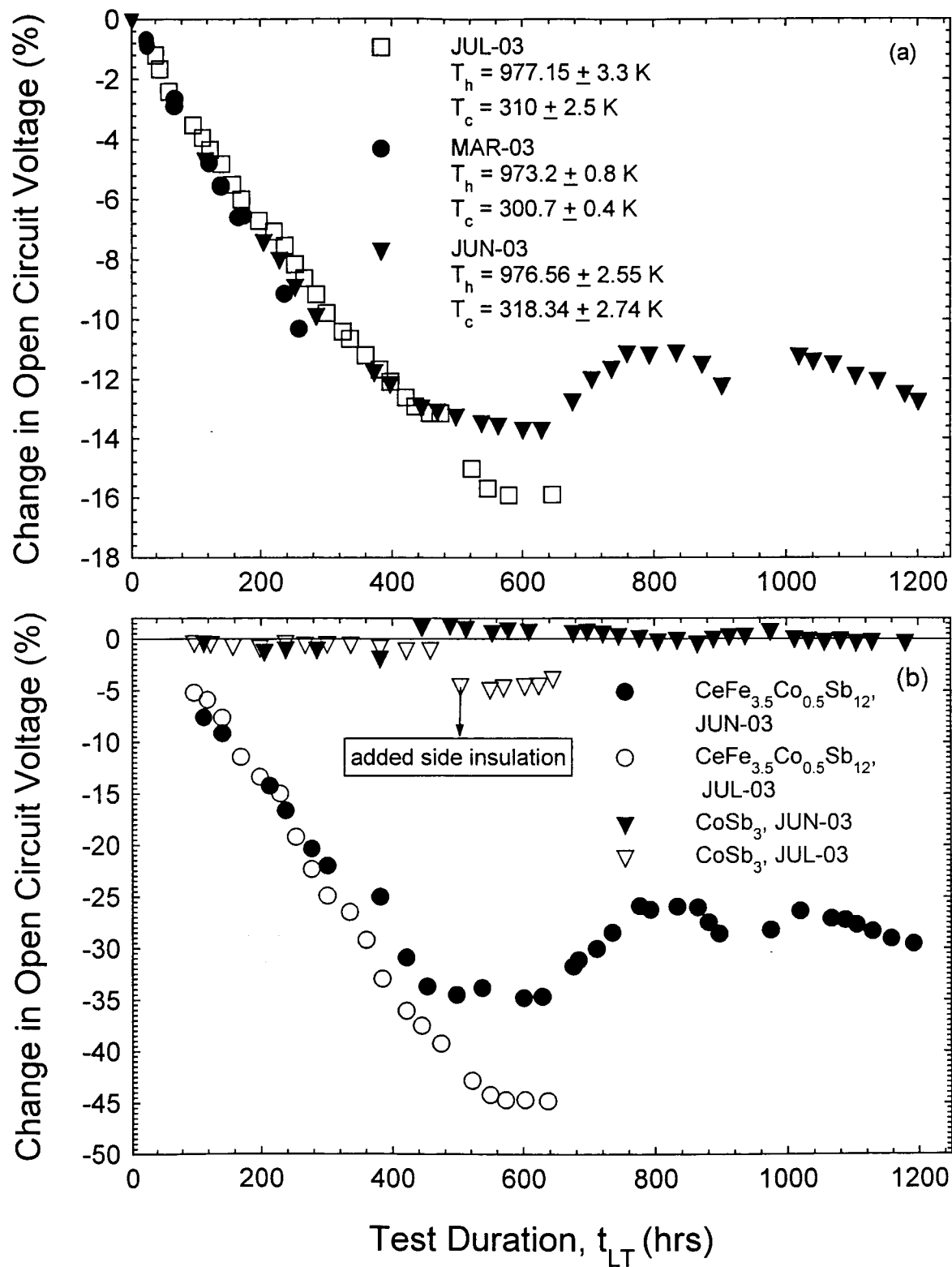


Figure 5-8 Measured Changes in Open Circuit Voltages for MAR-03 and JUN-03 Skutterudites and JUL-03 STE Unicouples.



JUL-03, respectively, after ~ 550-600 hrs (Figure 5-8a). Since the hot junction temperatures in the tests are kept almost constant, therefore, the measured decreases in  $V_{oc}$  with test duration are directly proportional to the decreases in the Seebeck coefficient of the thermoelectric materials in the n- and p-legs.

The data delineated in Figure 5-8b show that the measured decrease in  $V_{oc}$  with test duration is mostly due to the decrease in the Seebeck coefficient of the  $CeFe_{3.5}Co_{0.5}Sb_{12}$  in the p-legs. the change in the measured open circuit voltage for  $CoSb_3$  in the n-legs is negligible. In Figure 5-8b, the indicated drop in  $V_{oc}$  for the  $CoSb_3$  segment in the n-leg of JUL-03 at the 500-hour occurred following an increase in the fiberglass insulation in the test (Figure 5-5b and Figure 5-6b). The additional insulation decreased the temperature differential across the  $CoSb_3$  segment in JUL-03 uncouple (Figure 5-3a); however, the actual value of the Seebeck coefficient is unchanged ( $V_{oc} = |\alpha| \times \Delta T$ , where  $\alpha$  is the Seebeck coefficient and  $\Delta T$  is the temperature difference across the  $CoSb_3$  segment) from that before the addition of the insulation. Because most of the added insulation was near the n-leg, the resulting change in the open circuit voltage in the p-leg is negligible.

## 5.7 Analysis of Performance Data

The analysis of the test data is carried out using 1-D and 3-D models of the uncouples (El-Genk and Saber 2002 and 2003, Saber and El-Genk 2002) to provide best estimates of the BOL side heat losses in the tests, conversion efficiencies of the uncouples, contact resistances for the n- and p-legs, and the total resistances of the n- and p-legs, including those of the contacts, as function of test duration. The 1-D and the 3-D models are also used in the thermal and performance analyses of the segmented thermoelectric converters and presented in chapters 2 and 3 of the report. The 1-D model is fully analytical, assumes no side heat losses and constant hot and cold junction temperatures, and fully accounts for the changes in the properties of the thermoelectric materials in the n- and p-legs with temperature (El-Genk and Saber 2002 and 2003). This model is capable of handling up to five segments of different materials in each leg; thus its accuracy is solely dependent on the uncertainties in the thermoelectric properties and the validity of the assumption of neglecting side heat losses.

In actual space power systems such as those using  $^{238}\text{PuO}_2$  General Purpose Heat Source (GPHS) (Carpenter 1970, Schock 1980, and Bennet, Lombardo and Rick 1987), the input power

to the unicouples is constant and both the hot and cold junction temperatures change with the load electric current. At the selected nominal operation design point, however, which is typically near the peak efficiency of the unicouples, the hot and cold junction temperatures are almost constant, since the heat input from the radioactive decay of the  $^{238}\text{Pu}$  in the GPHS (half-life  $\sim 87$  years) decreases very slowly with time ( $\sim 6\%$  after 7 years). In addition, the side insulation of the thermoelectric unicouples in these power systems significantly reduce side heat losses to  $\sim 5\%$  of the input thermal power from the GPHS. *Therefore, the BOL efficiency estimates obtained using the 1-D model, based on the measured BOL contact resistances, and the constant hot and cold junction temperatures in the tests, and assuming zero side heat losses, are expected to be on the high side, but within 5%-10% of the actual values for the space power system.*

The 3-D model for STE unicouples utilizes the comprehensive finite element computation and the numerical grid meshing capabilities in the ANSYS commercial software (chapter 3), thus is capable of calculating detailed 3-D temperature fields in the p- and n-legs, handling unlimited number of segments in the legs, and using various boundary conditions at the hot and cold junctions and along the side surfaces of the n- and p-legs. The 3-D model is used in conjunction with test measurements to estimate the BOL side heat losses. It is also used to estimate the side heat losses at different time during the tests, assuming no changes in the surface properties of the n- and p-legs, which may not necessary true. Because of the extensive meshing requirements in the 3-D model, particularly near the interfaces between various segments and at the hot and cold junctions, the time for setting and solving a typical problem is significantly larger than with the 1-D model. A typical CPU required for setting and solving a problem using the 1-D model is  $\sim 2$  seconds versus more than 20 minutes for the 3-D model on a desktop computer. The 3-D model is used in the analysis of the preset test data to obtain estimates of the side heat losses and the actual peak electrical power in the various tests (Figure 5-9 and Figure 5-10). The procedures used to analyze the test data in conjunction with using the 1-D and 3-D models of the unicouples are discussed next.

## **5.8 Estimates of Contact and Thermoelectric Resistances**

First, calculations of the unicouples' V-I characteristics are performed using the 1-D model, assuming zero side heat losses, but for the same hot and cold junction temperatures, thermoelectric materials properties, and the dimensions of the p- and n-legs in the unicouples in

the tests. The BOL slope of the V-I characteristics (Figure 5-7a and Figure 5-7b) depend on the contact resistances for the n- and p-legs. The values of these resistances, which result in the same slopes of the calculated as of the measured I-V characteristics at BOL, are taken as best estimates for the n- and p-legs in the subsequent analysis using the 3-D model to obtain best estimates of BOL side heat losses in the tests (Figure 5-9a and Figure 5-10a). The BOL analysis of the data is based on the available database of the thermoelectric material properties. However, the measured increases in the slope of the V-I characteristics, particularly those for JUL-03 (Figure 5-10a), with test duration (Figure 5-7b) may not solely be due to an increase in the contact resistances in the n- and p-leg, but include increases in the electrical resistivities of the thermoelectric materials in the n- and p-legs. Therefore, the measured increase in the total resistances of the n- and p-legs in Figure 5-9a and Figure 5-10a as functions of test duration include those of the contacts and of the thermoelectric materials in the legs.

The total contact resistance for the n-leg includes those of the solid-solid contact with the Cu hot shoe, between the metal segments at hot and cold junctions, between the metal segment and Cu cold shoe (Figure 5-4). The p-leg contact resistance includes those of solid-solid contact with the Cu hot shoe, between  $\text{CeFe}_{3.5}\text{Co}_{0.5}\text{Sb}_{12}$  and metal segments at hot junction and the Cu cold shoe (Figure 5-4). The increase in the contact resistances in the tests could be caused by chemical reactions at the hot junctions of the n- and p-legs, respectively. The chemical reaction of antimony with the Cu hot shoe (Figure 5-4) could have also contributed to the increases in the contact resistances. Visual observation using an SEM revealed extensive surface deposits, however, the nature and extent of the reactions is outside the scope of these tests and would be the subject of a further investigation. The thermoelectric resistances of the n- and p-legs, do not affect the open circuit voltage, however, the differences between calculated BOL resistances using 1-D model and measured, are indicative of the side heat losses in the tests. At later times in the tests, these differences are indicative of both the side heat losses and the decrease in the Seebeck coefficients of the thermoelectric materials. The calculated  $V_{oc}$  using the 1-D model at BOL is higher than measured and the difference is indicative of BOL side heat losses. Estimates of these losses are listed in Table 5-1 and discussed next.

## 5.9 Estimates of BOL Side Heat Losses

The 3-D model estimates of the side heat losses in the tests are based on the measured values of the BOL open circuit voltages. The estimated BOL side heat losses are  $2.3 W_{th}$  and  $9.238 W_{th}$  in MAR-03 and JUL-03, respectively (Table 5-1). The estimates of the side heat losses at later times in the tests assume that the Seebeck coefficients of the thermoelectric materials did not change from their BOL value, which may not be true, thus could be higher than present estimates, excluding BOL, by those corresponding to the actual decreases in the Seebeck coefficients of the thermoelectric materials in the n- and p-legs.

Table 5-1 Estimates of BOL Performance Parameters for MAR-03 Sutterudites JUL-03 STE Unicouples Tested.

PERFORMANCE PARAMETER	MAR - 03 ( $t_{LT} = 24$ hrs)	JUL - 03 ( $t_{LT} = 16$ hrs)
Contact resistance of P-Leg ( $\mu\Omega\text{-cm}^2$ )	380.0	110.4
Contact resistance of N-Leg ( $\mu\Omega\text{-cm}^2$ )	380.0	450.6
Estimate of side heat losses in tests ( $W_{th}$ )	2.30	9.238
$\eta_{peak}$ estimate in tests (%)	7.287	6.264
$\eta_{peak}$ estimate, based on measured leg resistances and zero-side heat losses (%)	10.703	13.454
Measured peak electric power ( $W_e$ )	671.11	1295.0
Peak power estimate for zero-side heat losses ( $W_e$ )	743.43	1423.7

## 5.10 Peak Conversion Efficiency and Load Electric Power

Figure 5-9a and Figure 5-10a present estimates of the peak conversion efficiency for MAR-03 and JUL-03, respectively, that are calculated using the 1-D model at different test durations. These estimates are based on the measured resistances of the n- and p-legs in the tests, but assume zero side heat losses, thus should be  $\sim 5\%$  to  $10\%$  higher than those of the same unicouples in space power systems, which typically has thermal efficiency of  $90\% - 95\%$  (or thermal heat losses of  $5\%$  to  $10\%$ ). The calculated BOL conversion efficiency MAR-03 uncouple is  $10.7\%$  and that of JUL-03 STE is  $13.5\%$ . These estimates of the conversion efficiency are about  $10\%$  lower than theoretical prediction with zero contact resistances and side heat losses. The estimates of the conversion efficiency of MAR-03 decreases linearly with testing time to  $\sim 10\%$  after 261 hrs, while those of JUL-03 decrease also linearly to  $\sim 8\%$  after 575 hrs of testing (Figure 5-9a and Figure 5-9b). Figure 5-9a also shows that the total

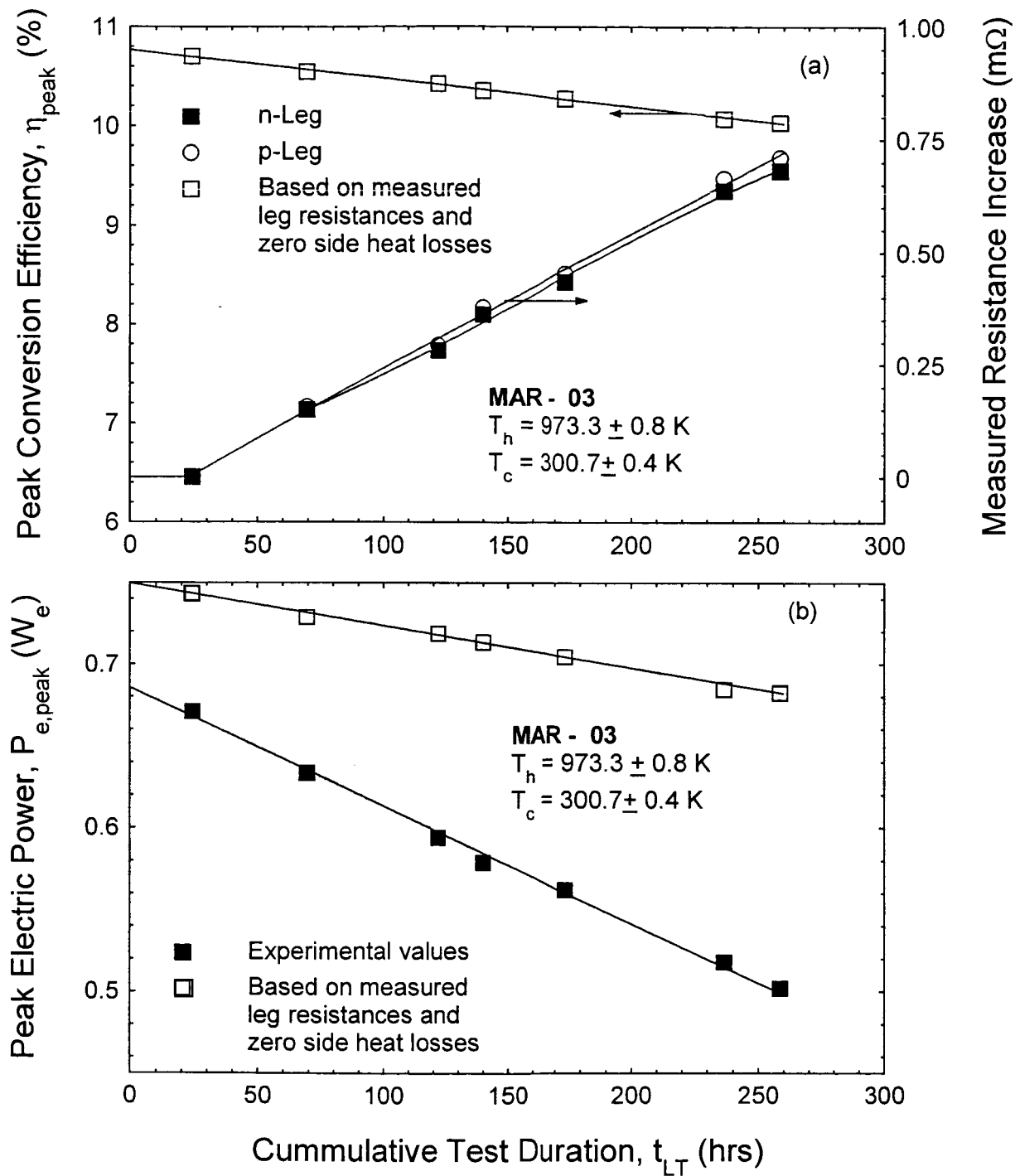


Figure 5-9 MAR-03 Measured and Calculated Performance.

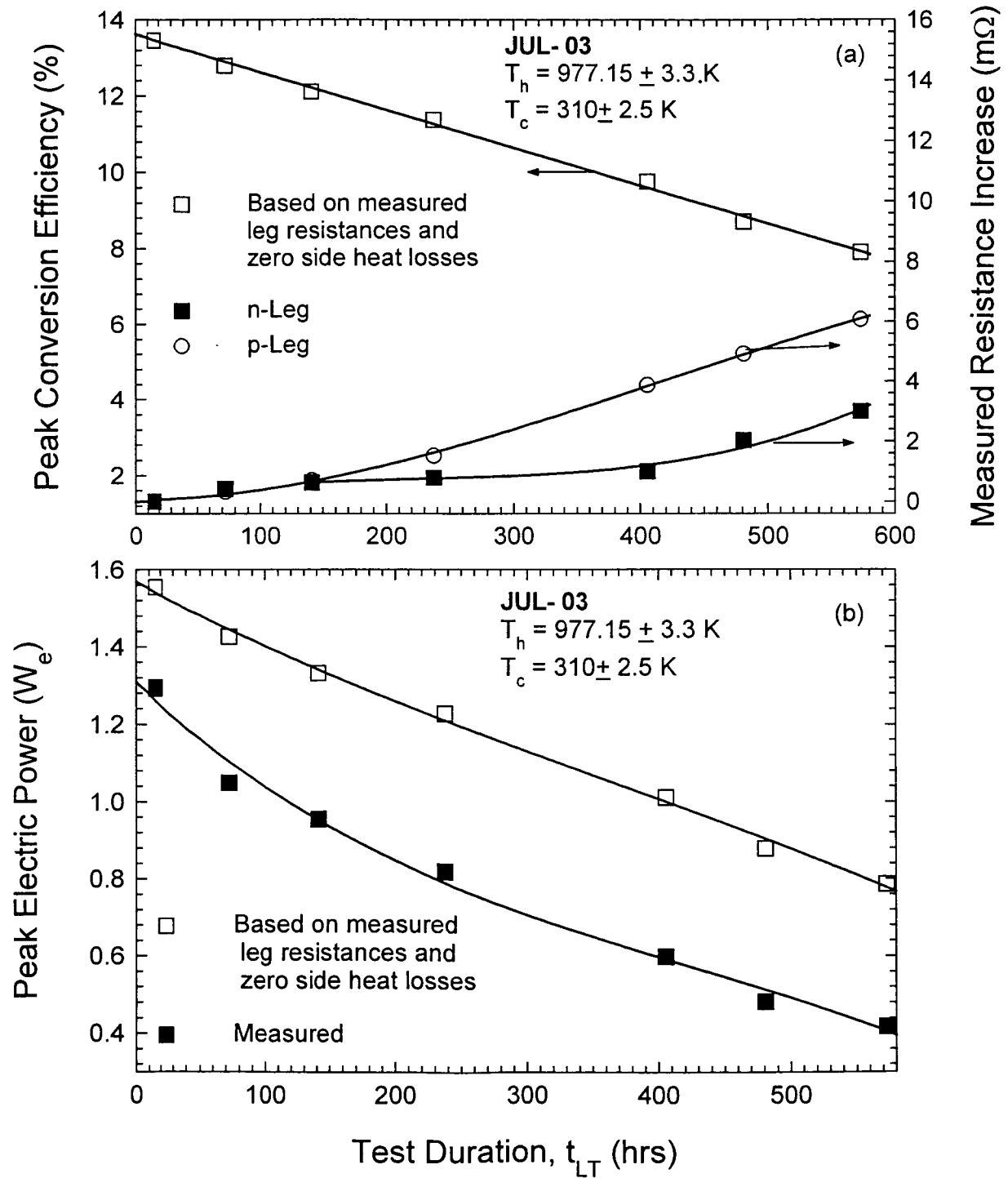


Figure 5-10 JUL-03 Measured and Calculated Performance.

resistances of the n- and p-legs in MAR-03 increased linearly with test duration. As indicated earlier, and based on the small decreases in the slopes of the measured V-I characteristics for this uncouple (Figure 5-7a), the increases in the resistances of the legs in MAR-03 are likely due to increases in the contact resistances. Conversely, owing to the continuous increase in the slopes of the V-I characteristics of JUL-03 STE uncouple with test duration, the measured increases in the resistances of the n- and p-legs in Figure 5-10a are likely the sum of the increases in both contact and thermoelectric material resistances.

Figure 5-9b and Figure 5-10b compare the measured peak electrical powers (solid symbols) for MAR-03 and JUL-03, respectively, at different test durations with those calculated based on the measured resistances of the p- and n-legs and assuming zero side heat losses (open symbols). At BOL, the differences between these values of the peak electrical power is  $\sim 70$  mW for MAR-03 and 180 mW for JUL-03 STE uncouple. The difference between measured and estimated peak electrical power of JUL-03 increases with test duration up to 150 hrs, then remains almost constant at  $\sim 180$  mW. For MAR-03, however, the difference between measured and estimated peak electric powers increased linearly with test duration, reaching  $\sim 180$  mW after only 258 hrs of cumulative testing at almost the same hot and cold junction temperatures as for JUL-03. Note that the peak electrical powers for JUL-03 are typically more than twice those for MAR-03, owing to the much larger cross-sectional areas of the n- and p-legs of the former (Figure 5-4).

Following the termination of the tests of MAR-03 and JUL-03, very little gray deposits are found in the fiberglass insulation. These deposits are indicative of the amount of sublimed Sb from the n- and p-legs near the hot junctions. In previous tests conducted in vacuum at  $\sim 10^{-5}$  Pa in the same test facility at UNM-ISONPS for only a few hours, extensive dark gray Sb deposits occurred when the hot junction temperature reached or exceeded 600 K. The deposited Sb could be seen clearly throughout the fiberglass insulation surrounding the uncouple in the tests. Therefore, using argon overpressure of 0.051 to 0.068 MPa in current tests has been effective in suppressing extensive Sb sublimation.

## 5.11 Summary

Performance tests of skutterudites-based non-segmented uncouples (MAR-03 and JUN-03) with a p-leg of  $\text{CeFe}_{3.5}\text{Co}_{0.5}\text{Sb}_{12}$  and n-leg of  $\text{CoSb}_3$ , and of a segmented uncouple (JUL-03), in which the p-leg has segments of  $\text{CeFe}_{3.5}\text{Co}_{0.5}\text{Sb}_{12}$  and  $\text{Bi}_{0.4}\text{Sb}_{1.6}\text{Te}_3$  and the n-leg has segments of

CoSb<sub>3</sub> and Bi<sub>2</sub>Te<sub>2.95</sub>Se<sub>0.05</sub> (Figure 5-4b) are performed at average hot and cold junction temperatures of 973 K and 300 K, respectively. The objective of these tests was to generate BOL performance data to compare with theoretical predictions for these unicouples. The tests are performed in argon at 0.051 - 0.068 MPa, which effectively suppressed Sb sublimation. The tests duration is 450 hours for MAR-03, 1200 hours for JUN-03, and 645 hours for JUL-03. MAR-03 and JUN-03 unicouples have approximately the same dimensions and the cross-section areas of the n- and p-legs, which are significantly smaller than for JUL-03 uncouple. The measured peak electric power for the later are more than twice those for MAR-03 and JUN-03 at the same average temperatures for the hot and cold shoes.

The measured  $V_{oc}$  and peak electrical power for MAR-03 decreased linearly from 203.6 mV and 671 mW<sub>e</sub> at BOL to 183.9 mV and 502 mW<sub>e</sub>, respectively, after 24 and 259 hours of cumulative testing at above temperatures, respectively. Similarly, the calculated peak efficiency based on the measured resistances of the legs, but assuming zero side heat losses, decreased linearly from 10.7% at BOL to 10% after 258 hours of testing at average hot and cold junction temperatures of ~ 973 K and 300 K, respectively. For JUL-03, BOL  $V_{oc}$  is 0.205 mV and decreased initially linearly to 0.185 mV after 406 hours and the estimate of the peak conversion efficiency based on the measured resistances of the n- and p-legs, and assuming zero side heat losses decreased for 13.5% at BOL to 10.8% after 406 hours of cumulative testing. The measured decreases in the open circuit voltages for all three unicouples with test duration are consistent; they decrease linearly for about 450 – 500 hours then approach asymptote of 84% and 86% of the BOL values for MAR-03 and JUN-03 and for JUL-03, respectively. The measured decreases in the open circuit voltage are mostly due to the decrease in the open circuit voltage of CeFe<sub>3.5</sub>Co<sub>0.5</sub>Sb<sub>12</sub> in the p-leg; the measured open circuit voltage for the CoSb<sub>3</sub> in the n-legs is almost constant during the tests.

The current tests provided the first set of performance data for skutterudites-based unicouples for the longest test duration ever reported to date, at average hot and cold junction temperatures of 973 K and 300 K, respectively. The estimates of the conversion efficiencies based on the measured V-I characteristics and the determined resistances of the n- and p-legs are ~ 10% lower than theoretical predictions assuming zero side heat losses and zero contact resistances. Results show that at BOL conversion efficiencies of 10.7% and 13.5% are possible for non-segmented and segmented skutterudites-based uncouple, when operated at the above temperatures. These



efficiencies are slightly lower than theoretical predications because of the contact resistances in the n- and p-legs. In addition, the side heat losses in the experiments are responsible for the much lower BOL conversion efficiencies in the tests, which are ~ 7.3% and 6.3% for Mar-03 and JUL-03, respectively. The heat losses in the tests, however, are much higher than expected in actual space power systems, in which the total thermal losses are typically 5% to 10%. Therefore, the BOL performance of the unicouples tested, when installed in a space power system are expected to be much higher than in the current tests and closer to theoretical predications.

Test results also suggest that the measured decreases in the unicouples performance with test durations could be partially attributed to the side heat losses in the tests, and possible increases in the contact resistances and the electrical resistivities of the thermoelectric materials in the n- and p-legs with test duration.

## 6 UNICOUPLE DEVELOPMENT (JPL)

### 6.1 Thermoelectric Materials

The segmented unicouple developed under this task is illustrated in Figure 6.1. It utilizes a combination of state-of-the-art p-type  $\text{Bi}_{0.4}\text{Sb}_{1.6}\text{Te}_3$  and n-type  $\text{Bi}_2\text{Te}_{2.9}\text{Se}_{0.1}$  thermoelectric materials at the low temperature ends. For the upper temperature segments, skutterudite materials are used. The p-type is a filled skutterudite with a  $\text{Ce}_{0.85}\text{Fe}_{3.5}\text{Co}_{0.5}\text{Sb}_{12}$  composition while the n-type composition is a Pd and Te doped  $\text{CoSb}_3$  composition.

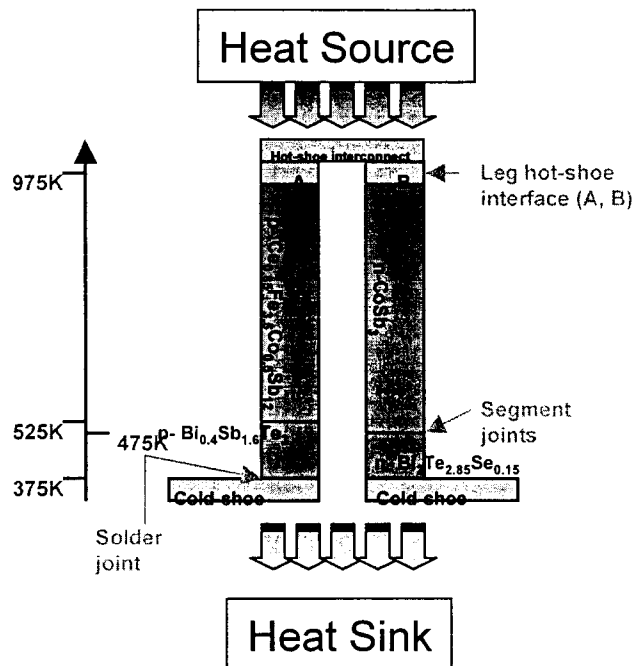


Figure 6-1 Illustration of Segmented Unicouple Utilizing  $\text{Bi}_2\text{Te}_3$ -based Segments at the Low Temperature Ends and Skutterudite Materials for the Upper Temperature Segments.

All materials are prepared as follows. The elements in stoichiometric ratios are placed in BN crucibles. These crucibles are then loaded into quartz ampoules, evacuated and sealed under  $10^{-6}$  Torr vacuum. The ampoules are then heated up to temperatures about 975K for  $\text{Bi}_2\text{Te}_3$  based materials and up to 1475K for skutterudite materials. The ampoules are held at these temperatures for at least 10 hours and subsequently water quenched. The quenched ingots are then removed from the ampoules inside a glove box under Ar atmosphere and loaded into stainless steel vials together with 4 stainless balls. The ingots are milled to reduce them into fine powders. A series of experiments has been conducted to optimize the milling time in order to

achieve optimal density, microstructure and properties after subsequent hot-pressing. It was found that a milling time of 10 minutes gave the best results.

Samples of each thermoelectric was then hot-pressed at temperature between 775K and 975K depending on the material and at a pressure of 22,000 psi. The thermoelectric properties have been measured as a function of temperature on a number of samples to ensure reproducibility and to acquire a reliable database for use in the theoretical performance prediction of the uncouple. ZT values as a function of temperature are shown in Figure 6-2.

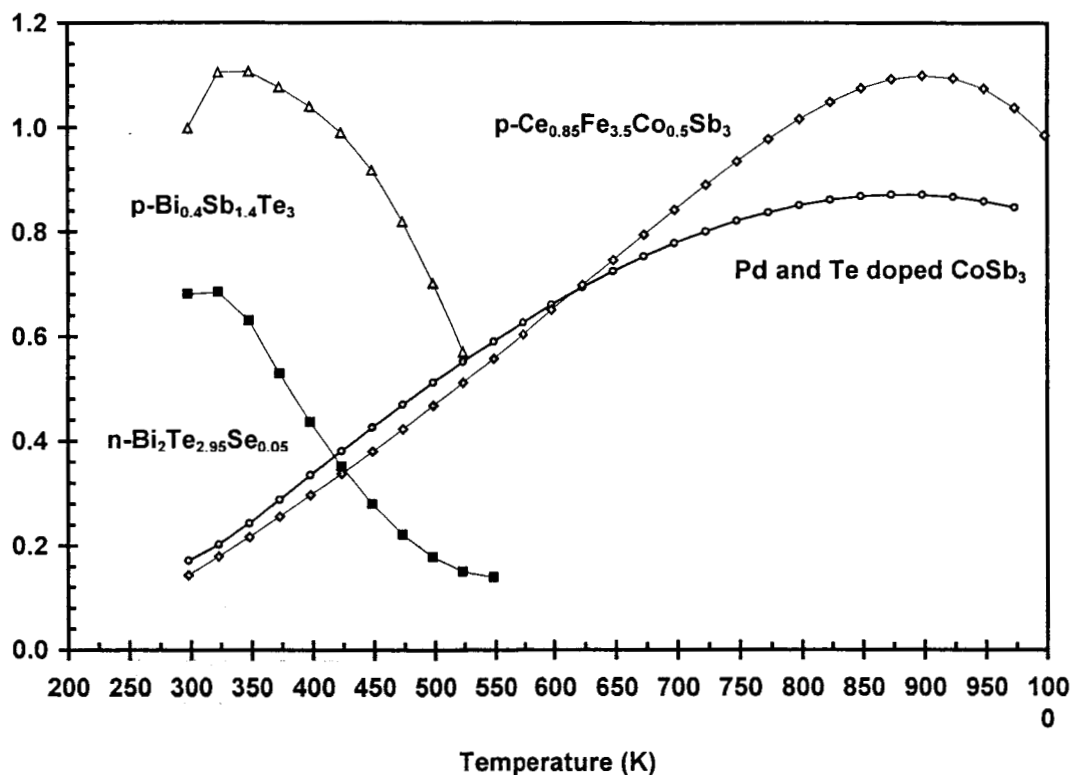


Figure 6-2 ZT Values as a Function of Temperature for Uncouple Thermoelectric Materials.

## 6.2 Segmented Legs Fabrication

As illustrated in Figure 6-1, the challenges are to achieve low electrical contact resistance bonds between the thermoelectric materials segments and between these materials and the metal contacts on both the cold and hot ends of the legs. Using the theoretical performance prediction models described earlier, it was shown that electrical contact resistance value below  $10 \mu\Omega\text{cm}^2$  must be achieved to result in a negligible decrease in the uncouple efficiency. In addition, the interface materials between the thermoelectric materials must be efficient diffusion barriers to

prevent diffusion of elements from one segment to the other that could result in a deterioration of the materials thermoelectric properties.

P- and n-segmented and non-segmented (i.e. skutterudite only) legs are fabricated using a single step hot-pressing technique. Powders of the various metal contacts, thermoelectric, and diffusion barrier materials are successively loaded into a graphite die with a cold-pressing step in between to ensure flatness of the interfaces. A final hot-pressing is performed under argon atmosphere and a pressure of 22,000 psi. A number of metal contact and diffusion barrier materials were originally selected for experimentation. The selection was primarily based on ensuring a close Coefficient of Thermal Expansion (CTE) match between the thermoelectric materials and the metal contacts on the cold and hot-ends. The CTE for skutterudite materials were measured to be  $10.2 \times 10^{-6}/T$  for the p-type material and  $9.1 \times 10^{-6}/T$  for the n-type material. The CTE is between 17 and  $18.5 \times 10^{-6}/T$  for the  $\text{Bi}_2\text{Te}_3$  based segments. The quality of the bonds was assessed through detailed microstructure and electrical contact resistance measurements that will be presented in the following section.

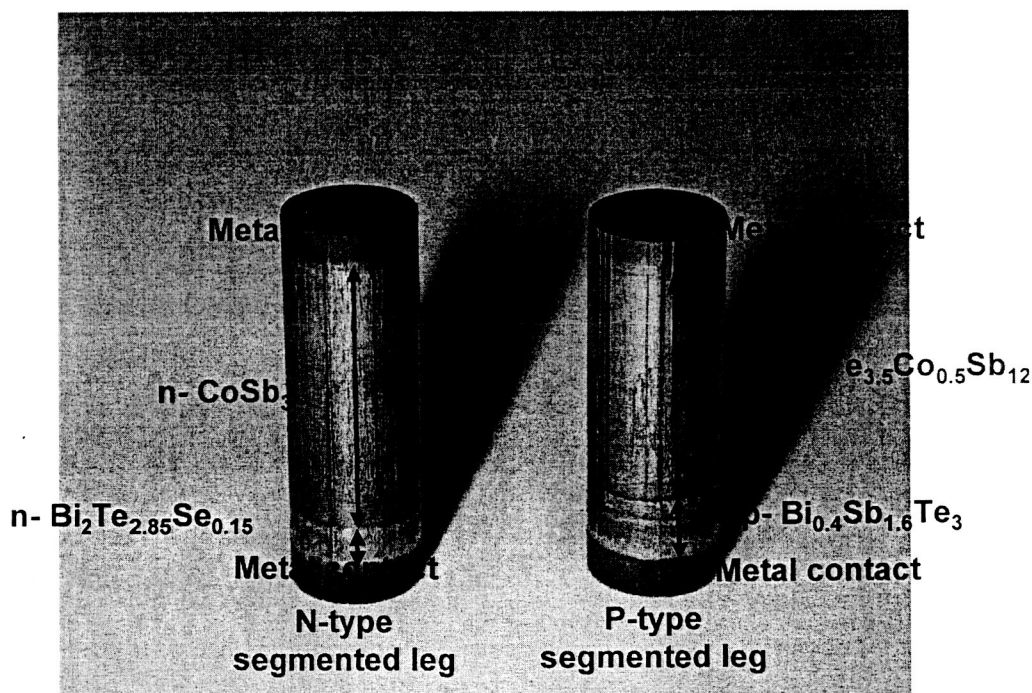


Figure 6-3 N- and p-type Segmented Legs After Hot-Pressing.

The best materials combination for a segmented uncouple is illustrated in Figure 6-3 and is:

P-type:  $\text{Ti}/\text{Pd}/\text{Ce}_{0.85}\text{Fe}_{3.5}\text{Co}_{0.5}\text{Sb}_{12}/\text{Pd}/\text{Ti}/\text{Bi}_{0.4}\text{Sb}_{1.6}\text{Te}_3$

N-type :  $\text{Ti}/\text{CoSb}_3/\text{Ti}/\text{n- Bi}_2\text{Te}_{2.95}\text{Se}_{0.05}$

The diffusion barrier thickness is typically between 25 and 100  $\mu\text{m}$  and the metal contacts between 500  $\mu\text{m}$  and 2 mm.

### 6.3 Segmented Legs Characterization

The first test performed on the legs is an electrical contact resistance test. It consists of measuring the resistance between one end of the leg and a moving probe that travels on the surface of the leg. One can therefore measure the contact resistance across the various interfaces in the leg when the probe crosses those interfaces. Figure 6-4 shows an n-leg instrumented for electrical contact resistance measurement. The test can be performed either at room temperature or in-gradient to simulate the actual operating condition. The test jig is located in a vacuum bell jar and run under vacuum ( $10^{-5}$  Torr)

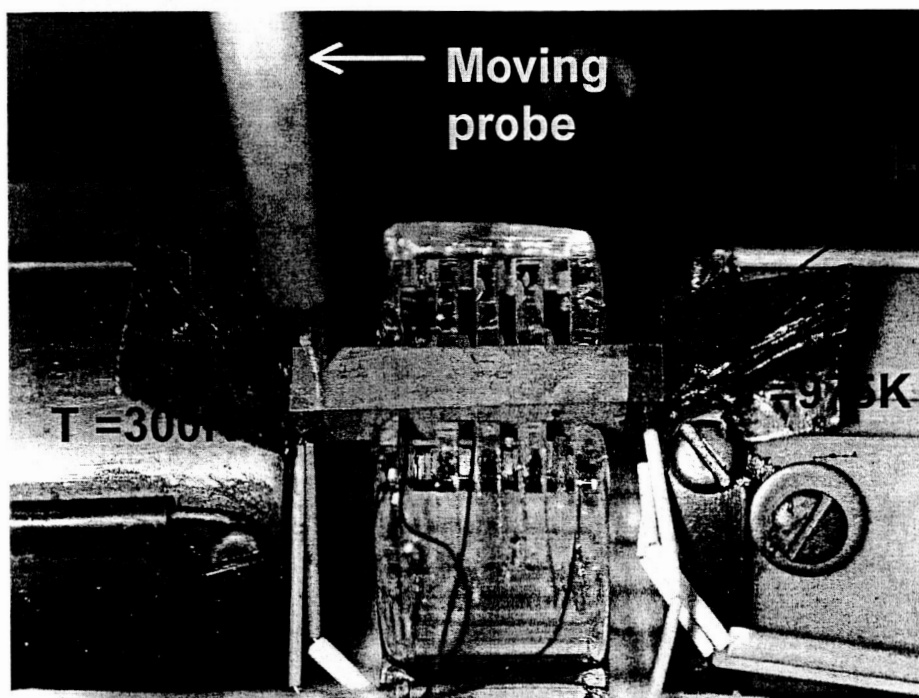


Figure 6-4 Photograph on n-type Skutterudite Leg (with Metal Contact on Both Ends) in the Electrical Contact Resistance Test Jig.

Results of short and extended term testing for segmented and un-segmented legs are presented in Figure 6-5 through Figure 6-7. Those results, for optimized segmentation materials, show that desired low electrical contact resistance can be achieved and maintained over time. Life testing should now be conducted to evaluate the change in electrical contact resistance over extended periods of time. In addition, selected samples were prepared for microstructure analysis to study

bond quality and potential diffusion through interfaces. Results show that Ti is an excellent diffusion barrier between  $\text{Bi}_2\text{Te}_3$  and skutterudite segmented at operating temperatures around 500K. Secondary Electron Microanalysis of interfaces after testing confirms the good bond quality and revealed the thickness and composition of intermetallic materials forming at the bond interfaces. In all cases, the thickness of the reaction layers remains relatively small (on the order of 100  $\mu\text{m}$ ) which is desired to minimize potential brittleness of the bonds inherent to the nature of intermetallic compounds.

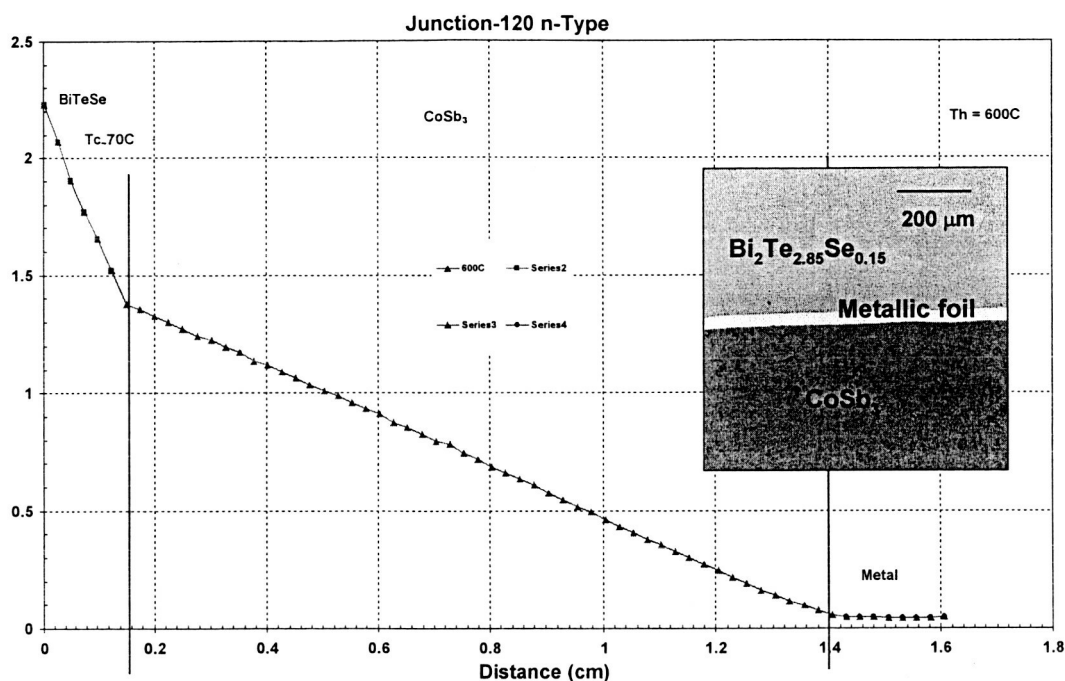


Figure 6-5 Results of In-gradient Contact Resistance Measurement for a Ti/CoSb<sub>3</sub>/Ti/n-Bi<sub>2</sub>Te<sub>2.95</sub>Se<sub>0.05</sub> Segmented Leg. The Electrical Contact Resistance at the Various Interfaces is Below 5  $\mu\Omega\cdot\text{cm}^2$ .

In addition to electrical contact resistance testing, in-gradient open circuit voltage testing was also performed to confirm theoretical prediction. In those tests, legs were sandwiched between a heater and cold heat exchanger to maintain a temperature gradient across the leg. The temperatures were measured on the cold- and hot-sides of the legs by thermocouples inserted into the metal contacts. Results are illustrated in Figure 6-8 that shows results of in-gradient open circuit voltage measurements for n- and p- legs. The experimental results are compared to theoretical predictions based on the measured Seebeck coefficient values of the materials. The agreement between theoretical and experimental data is within 5%.

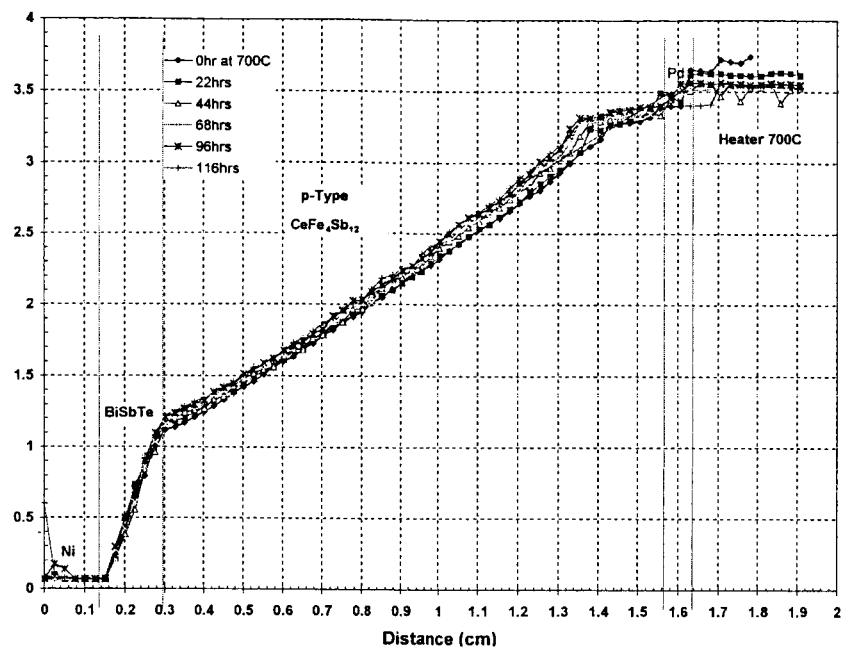


Figure 6-6 Results of In-gradient Contact Resistance Measurement for a Ti/Pd/Ce<sub>0.85</sub>Fe<sub>3.5</sub>Co<sub>0.5</sub>Sb<sub>12</sub>/Pd/Ti/Bi<sub>0.4</sub>Sb<sub>1.6</sub>Te<sub>3</sub> Segmented leg. The Electrical Contact Resistance at the Various Interfaces is Below 5  $\mu\Omega\text{-cm}^2$  and Shows Negligible Changes with time ( 116 Hours of Testing).

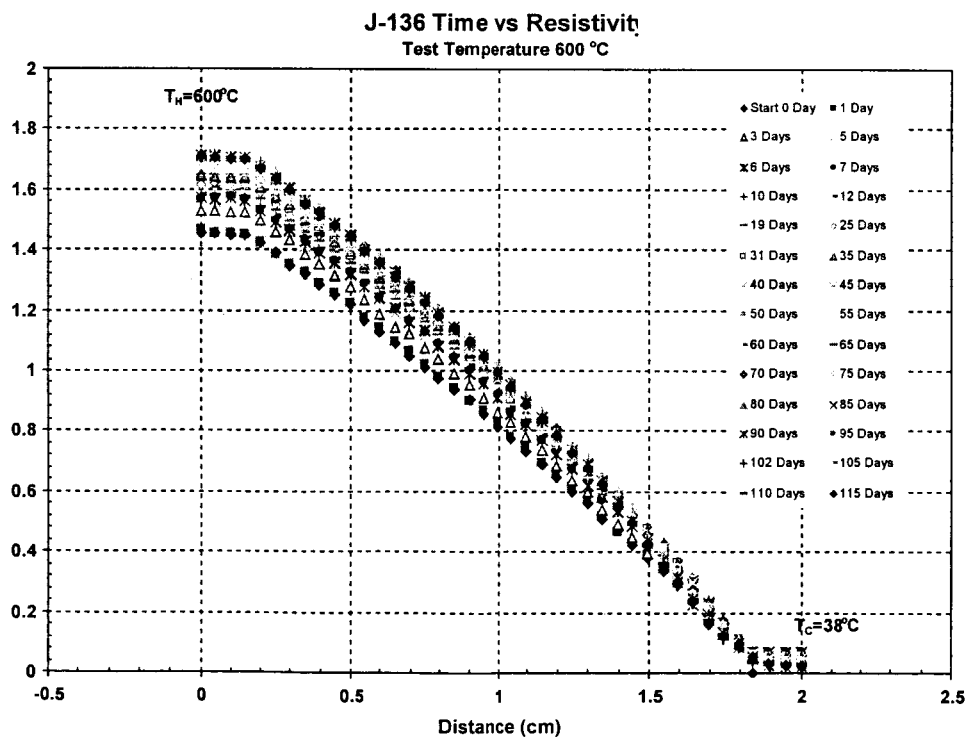


Figure 6-7 Results of In-gradient Contact Resistance Measurement for a Ti/CoSb<sub>3</sub>/Ti Skutterudite Leg. The Electrical Contact Resistance at the Various Interfaces is Below 5  $\mu\Omega\text{-cm}^2$ . The Sample Was Tested for a Maximum of 2760 Hours.

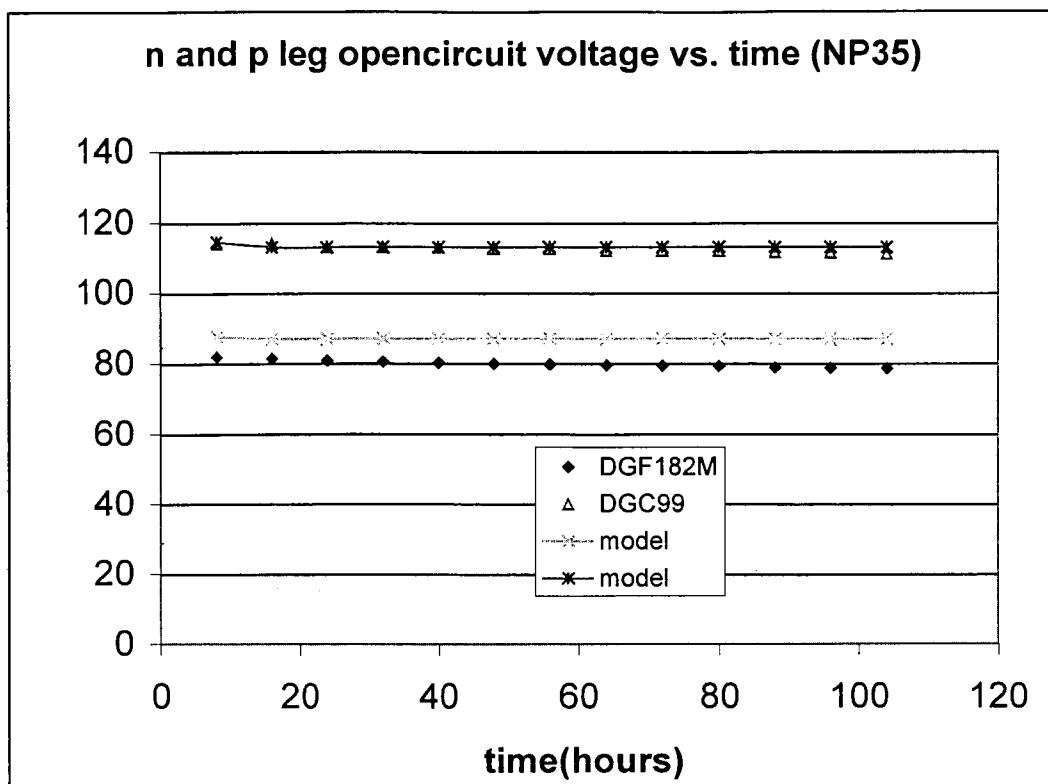


Figure 6-8 Results of In-gradient Open Circuit Voltage Measurements for n- and p- Legs. (p: DGF182 ; n: DGC99). The Experimental Results Are Compared to Theoretical Predictions Based on the Measured Seebeck Coefficient Values of the Materials. The Agreement Between Theoretical and Experimental Data is within 5%.

## 6.4 Sublimation Characterization

A series of p- and n-type samples were tested at temperatures and in dynamic vacuum in an effort to identify the main degradation mechanisms. Results show that the main degradation is through the loss of Sb. In the n-type material, Sb sublimation results into the decomposition of  $\text{CoSb}_3$  into  $\text{CoSb}_2$  and eventually into  $\text{CoSb}$ . The sublimation is illustrated in Figure 6-9 that shows a cross section of an n-leg after 3 months of testing at 975K. The decomposition of  $\text{CoSb}_3$  into lower antimonides is clearly seen. The thickness of the decomposition layers is, as expected, decreasing with the temperature at which the material was exposed along the leg. Bond integrity however seems to be preserved. It is also important to note that although the depth of the sublimation layer is approximately 250  $\mu\text{m}$  at the hottest point, the bond quality seems to be preserved and no cracking is observed. The sublimation will however alter the properties and performance of the leg with time and needs to be controlled. The identification of Sb potential sublimation techniques and materials is presented in the following section. In the case of the p-



type skutterudite material, results have shown that Sb is also the predominant volatile species. At temperatures starting around 875K up to the maximum projected operating temperature of 975K, the compound partially decomposes into  $\text{FeSb}_2$  and  $\text{CeSb}_2$  and Sb.

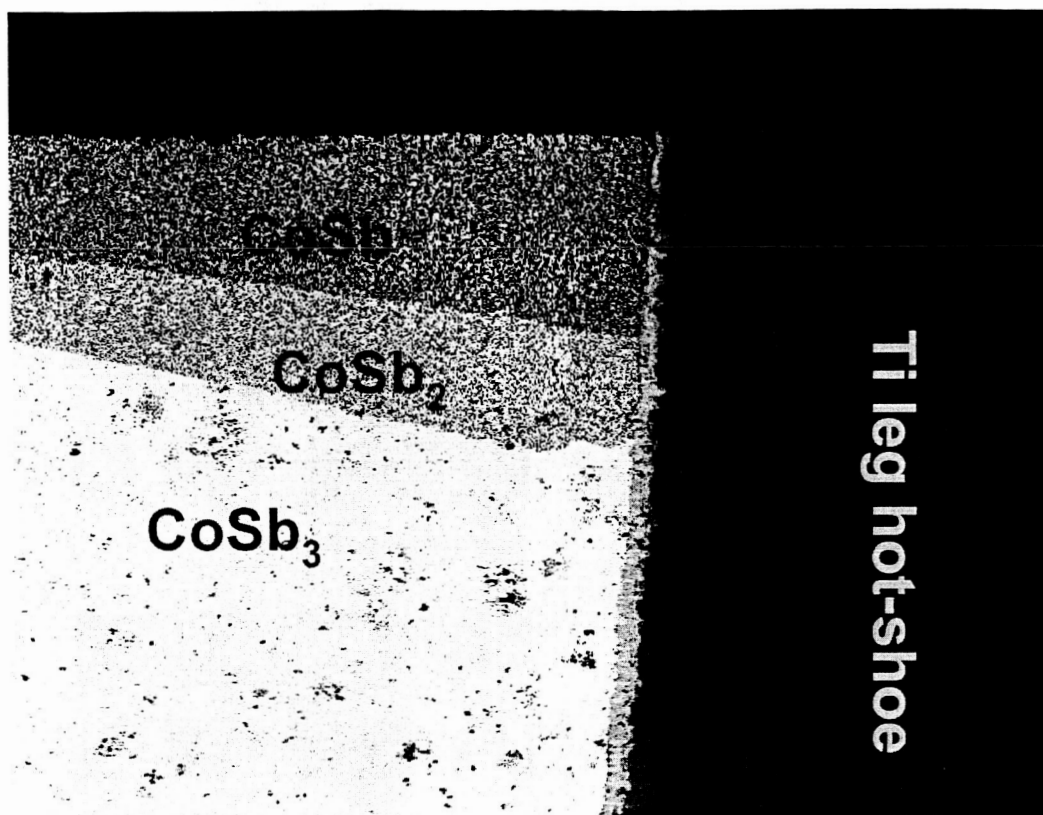


Figure 6-9 SEM Photograph of Section of an n-Leg After 3 Months of Testing at 975K. The “Necking” as a Result of Sb Sublimation Is Seen. Bond Integrity However Seems to be Preserved.

## 6.5 Development of Coatings Materials Techniques Results

The technique developed to control Sb sublimation is the application of thin metallic film (10 to 50  $\mu\text{m}$ ) on the outer surface of the sample. Typically the film is integrated to the leg during the hot-pressing as a sleeve. A number of metals have been tried and to date, the best results have been obtained with Ti and Mo. Figure 6-10 shows the upper section of an n-leg encapsulated with a 10  $\mu\text{m}$  thick Ti film. Figure 6-11 shows the mass loss measurement results as a function of time. The mass loss in the Ti coated sample is substantially reduced compared to uncoated samples. It amounts only about 2% for coated samples after about 250 hours versus about 25% for uncoated samples. While some further improvements in the coating process will be required

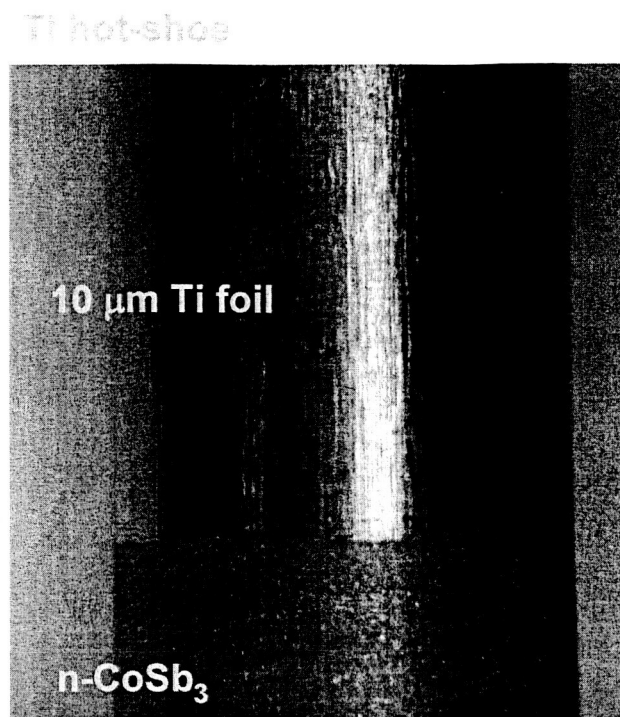


Figure 6-10 Photograph of n-Leg with Upper Section Encapsulated with 10 μm Thick Ti Foil.

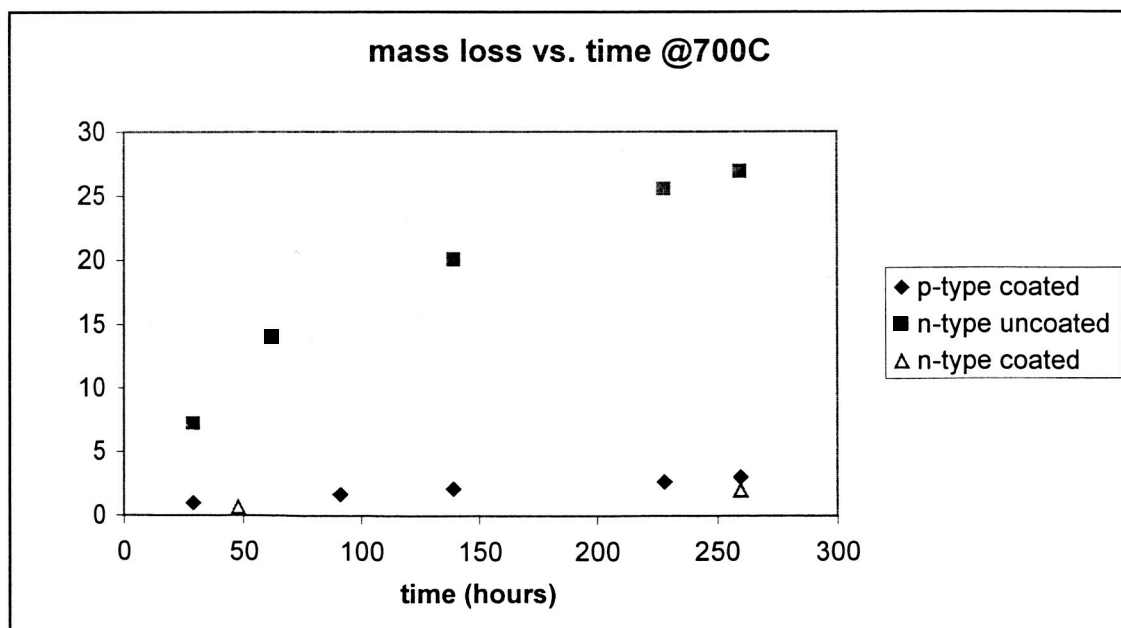


Figure 6-11 Mass Loss as a Function of Time for n- and p- Ti-Coated and Uncoated Samples Annealed at 975K.

to fully implement this technique, these preliminary results clearly indicate its potential. Figure 6-13 shows details images of cross section of a Ti coated n-type leg after anneal at 975K. The images clearly reveal the Sb suppression in the coated region while the sublimation layers are seen past the coated section.

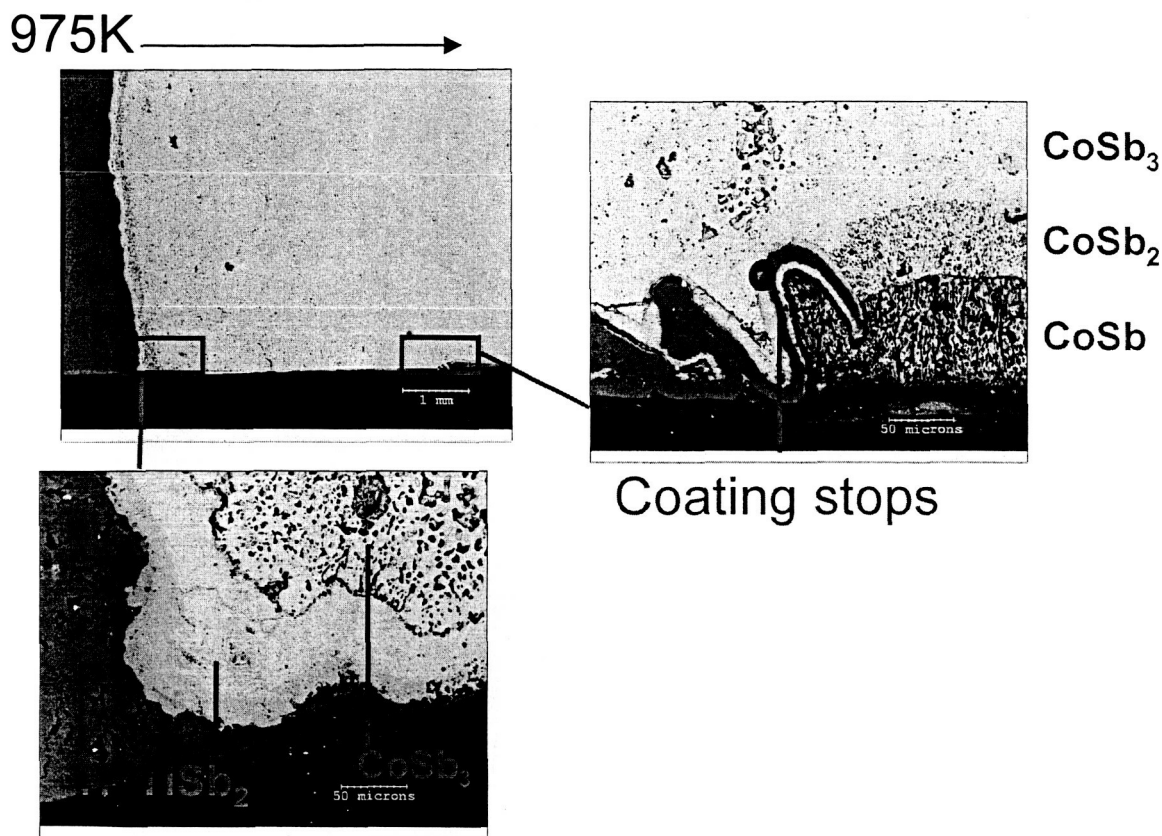


Figure 6-12 Cross-Sectional Views of Ti-Coated n-Leg in the Coated Region That Was Exposed to High Temperatures. The Images Clearly Reveal the Sb Suppression in the Coated Region While the Sublimation Layers Are Seen Past the Coated Section.

Encouraging results were also obtained with Mo coating. Figure 6-13 and Figure 6-14 shows the Thermogravimetric Analysis (TGA) plots from n-type coated and Mo-coated sample. While substantial mass loss is observed on the uncoated sample, no mass loss could be detected on the Mo-coated sample up to 975K.

While further life testing is required to fully assess the potential of these metallic coatings on the long term Sb sublimation suppression and on the overall unicouple performance, these results are very encouraging. Since metallic coatings are used, they constitute both a thermal and electrical short for the leg and eventually reduce the overall efficiency of the unicouple. The



thermal and performance model presented earlier also allows for the precise calculations of the performance penalty as a function of the thickness of the metallic coating layer. It is estimated that for coating layers thickness below 10 mm and with 1/3 of the overall length of the leg long, the decrease in efficiency is 1 to 2% of the overall efficiency in the uncoated case.

## **6.6 Summary**

A process was developed to fabricate segmented legs with low electrical contact resistance at the legs' interfaces. Limited in-gradient life testing has been conducted on coupons and the results showed promising integrity. Sb sublimation has been identified as the main short-term potential degradation mechanism. A thin metallic film coating technique was developed and showed very encouraging results towards suppressing Sb sublimation, at least over the short term testing scope of this task. Life testing is currently being investigated under a Code S task to further study the potential of these uncouples for ARPS applications. A number of skutterudite and segmented legs were fabricated at JPL and delivered to UNM for testing. The results of the tests were presented earlier.

## REFERENCES

- Angelo, J. A., and Buden, B., "Space Nuclear Power," Orbit Book Company Inc., Malabar, FL, Chapter 9; 159-197, 1985.
- Bennett, T., "Space Applications, CRC Handbook of Thermoelectrics", edited by D.M. Rowe, CRC Press, Boca Raton; 515 – 537, 1994.
- Bennett, G., Lombardo, J., and Rick, B., "Power Performance of the General-Purpose Heat Source Radioisotope Thermoelectric Generator," *Space Nuclear Power Systems*, M. El-Genk and M. Hoover, Eds., Orbit Book Co., Malabar, FL, **5**, 437 – 540, 1987.
- Caillat, T., Fleurial, J-P., and Borshchevsky, A., "Preparation and Thermoelectric Properties of Semiconducting  $\text{Zn}_4\text{Sb}_3$ ," *J Phys Chem Solids*, 58: 1119-1125, 1997.
- Caillat, T., Fleurial, J-P., Snyder, J., Zoltan, A., Zoltan, D., and Borshchevsky, A., "Development of a High Efficiency Thermoelectric Unicouples for Power Generation Applications," *Proceedings 18<sup>th</sup> International Conference on Thermoelectrics*, edited by A. Ehrlich, IEEE, Piscataway; 473-476, 1999.
- Caillat, T., Borshchevsky, A., Snyder, J., and Fleurial, J-P., "High Efficiency Segmented Thermoelectric Unicouples," *Proceedings Space Technology and Applications International Forum (STAIF-00)*, edited by M. S. El-Genk, American Institute of Physics, New York, AIP Conference Proceedings No. 504, 1508-1512, 2000.
- Caillat, T., Borshchevsky, A., Snyder, J., and Fleurial, J-P., "High Efficiency Segmented Thermoelectric Unicouples," *Proceedings Space Technology and Applications International Forum (STAIF-01)*, edited by M. S. El-Genk, American Institute of Physics, New York, AIP Conference Proceedings No. 552, 1107-1112, 2001.
- Carpenter, R. T., "Status of U. S. Radioisotope Space Power System," *Isotope and Radiation Technology*, **9**(3), 330 – 344, 1970.
- El-Genk, M. S. (Editor), *A Critical Review of Space Nuclear Power and Propulsion 1984-1993*, American Institute of Physics, New York, 1994.
- El-Genk, M. S., "Energy Conversion Technologies for Advanced Radioisotope and Nuclear Reactor Power Systems for Future Exploration," in *Proceedings, 21<sup>st</sup>*

*International Conference on Thermoelectrics*, IEEE, Piscataway, NJ, 375 – 380, 2002.

El-Genk, M. S., “Energy Conversion Options for Advanced Radioisotope Power Systems,” in *Proceedings of Space Technology and Applications International Forum (STAIF-03)*, edited by M. S. El-Genk, AIP Conference Proceedings No. **654**, American Institute of Physics, Melville, NY, pp. 368 – 375, 2003.

El-Genk, M. S. and Saber, H. H., “Performance Optimization of Segmented Thermoelectric Unicouples,” in *Proceedings of Space Technology and Applications International Forum (STAIF-02)*, edited by M. S. El-Genk, AIP Conference Proceedings No. **608**, American Institute of Physics, NY, pp. 980 -988, 2002.

El-Genk, M. S., and Saber, H. H., “Predictions of Segmented Thermoelectric Unicouples Performance at Hot Temperatures  $\leq 873$  K and Cold Temperature of 298 K,” *Proc. 21<sup>st</sup> Int. Conf. On Thermoelectrics*, Long Beach, CA, August 25-29, 2002.

El-Genk, M. S., Saber, H. H., and Caillat, T., “A Performance Comparison of SiGe and Skutterudite Based Segmented Thermoelectric Devices,” *Proc. Space Technology and Application Forum (STAIF02)*, El-Genk, M. S., Ed., American Institute of Physics, NY, AIP-CP-608, pp.1007-1015, 2002.

El-Genk, M. S. and Saber, H. H., “High Efficiency Segmented Thermoelectric for Operation between 973 K and 300 K,” *J. Energy Conversion and Management*, **44**(7), 1069 – 1088, 2003.

El-Genk, M. S., Saber, H. H., and Caillat, T., “Efficient Segmented Thermoelectric Unicouples for Space Power Applications,” *J. Energy Conversion and Management*, **44**(11), 1755 – 1772, 2003.

El-Genk, M.S., Saber, H. H., Sakamoto, J. and Caillat, T., “Life Tests of a Skutterudite Thermoelectric Unicouple (MAR-03),” in *Proceedings of 22<sup>nd</sup> International Conference of Thermoelectrics*, Herault, France, 17-21 August 2003, IEEE, Piscataway, NJ (in press).

El-Genk, M. S. and Saber, H. H., “Cascaded Thermoelectric Converters for Advanced Radioisotope Power Systems,” *Proceedings Space Technology and Applications*

*International Forum*, AIP Conference Proceedings No. 669, American Institute of Physics, Melville, NY, pp. 529, 2004.

El-Genk, M.S., Saber, H. H., and Caillat, T., "Performance test of Skutterudites and Segmented Thermoelectric Converters," *Proceedings of Space Technology and Applications International Forum (STAIF-04)*, edited by M. S. El-Genk, American Institute of Physics, NY, 2004.

El-Genk, M.S., Saber, H. H., "High efficiency Cascaded Thermoelectric Converters," *Proceedings of Space Technology and Applications International Forum (STAIF-04)*, edited by M. S. El-Genk, American Institute of Physics, NY, 2004.

Fleurial, J-P., Borshchevsky, A., Caillat, T., and Ewell, R., "New materials and Devices for Thermoelectric Applications" *Proceedings 32<sup>nd</sup> Intersociety Energy Conversion Engineering Conference*, American Institute of Chemical Engineers, New York, 1080-1085, 1997.

Fleurial, J.-P., Borshchevsky, A., Caillat, T., Morelli, D., and Meisner, G., "High Figure of Merit in Ce-Filled Skutterudites," *Proceedings of 15<sup>th</sup> International Conference on Thermoelectric*, IEEE catalog 96TH8169, p. 91, 1996.

GE, *General Purpose Heat Source Radioisotope Thermoelectric Generator (GPHS-RTG) Final Design Review*, General Electric Company, Space Systems Division, Advanced Energy Program Department, Valley Forge, PA, October 28-30, 1980.

Goldberg, D., *Genetic Algorithms in Search Optimization and Machine Learning*, Addison-Wesley Publishing Co., Inc., New York, NY, 1989.

Goldsmid, H. J., *Electronic Refrigeration*, Pion Limited, London; 1986. p. 7.

Hawley, J. P. and Johnson, R. A., *SNAP-10A FS-3 Reactor Performance*, Rockwell International Report No. NAA-SR-11397, August 1966.

Hendricks, T. J. and Lustbader, J. A., "Advanced Thermoelectric Power Systems Investigations for Light-Duty and Heavy Duty Applications: Part II," *Proceedings 21<sup>st</sup> International Conference on Thermoelectrics*, IEEE, Inc., Piscataway, NJ, pp. 387, 2002.



- Huber, T. E. , Graf, M. J., and Foss, C. A., "Thermoelectric bismuth wire array composites. Thermoelectric Materials: the Next Generation Materials for Small Scale Refrigeration and Power Generation Applications," *Proceedings of Materials Research Society Symposium*, edited by M. Tritt, H.B. Lyon, G. Mahan, and M. G. Kanatzidis, vol. 545, p. 227-31, 1999.
- Huber, T. E., and Constant, P., "Thermomagnetic Cooler Based on Bi and Bi-Sb Nanocomposites," *Proceedings Space Technology and Applications International Forum (STAIF-01)*, edited by El-Genk, M. S., American Institute of Physics, New York, AIP Conference Proceedings No. 552, 1113-1118, 2001.
- Josloff, A. T., Baily, H. S., and Matteo, D. N., "SP-100 System Design and Technology Progress," *Proc. 9<sup>th</sup> Symposium of Space Nuclear Power Systems*, American Institute of Physics, NY, Vol. 1, 363-371, 1992.
- Kelly, C.E., "The MHW Converter (RTG)", *Proceedings of 10<sup>th</sup> Intersociety Energy Conversion Engineering Conference*, American Institute of Chemical Engineers, New York, p. 880-6, 1975.
- Marriort, A. and Fujita, T., "Evolution of SP-100 System Designs," *Proceedings of Space Nuclear power and Propulsion*, M. S. El-Genk and M. Hoover, eds., Amer. Institute of Physics, New York, NY, AIP CP-301 pp. 157, 1994.
- Pierre, D., and Lowe, M., *Mathematical Programming Via Augmented Lagrangians, An Introduction with Computer Programs*, Addison-Wesley Co., 1975.
- Press, W., et al., *Numerical Recipes in Fortran 77, The Art of Scientific Computing*, volume 1 of Fortran Numerical Recipes, 2<sup>nd</sup> Ed., Cambridge [England]; New York: Cambridge University Press, 423-436, 1996.
- Qiu, S., Augenblick, J. E., White, M. A., Peterson, A. A., Redinger, D. L., and Peterson, S. L., "Developing a Free-Piston Stirling Converter for Advanced Radioisotope Space Power Systems," in *Proceedings of Space Technology and Applications International Forum (STAIF-02)*, edited by M. S. El-Genk, AIP Conference Proceedings **608**, American Institute of Physics, Melville, NY, 912 – 917, 2002.
- Smith, G. E, and Wolfe, R., "Thermoelectric Properties of Bismuth-Antimony Alloys," *J Appl Phys*, 33: 841-4, 1962.

- Schock A., "Design Evolution and Verification of the General Purpose Heat Source," *Proceedings 15<sup>th</sup> Intersociety Energy Conversion Engineering Conference*, American Institute of Aeronautics and Astronautics, 1508-1512, 1980.
- Saber, H. H. and El-Genk, M. S., "A Three-Dimensional Performance Model of Segmented Thermoelectric Converters," in *Proceedings of Space Technology and Applications International Forum (STAIF-02)*, edited by M. S. El-Genk, AIP Conference Proceedings No. **608**, American Institute of Physics, NY, 998 – 1006, 2002.
- Saber, H. H. and El-Genk, M. S., "Optimization of Segmented Thermoelectric for Maximizing Conversion Efficiency and Electric Power Density," *21<sup>st</sup> Int. Conf. On Thermoelectrics*, Long Beach, CA, August 25-29, 2002.
- Schock, A., "Design, Evolution and Verification of the General Purpose Heat Source," *Proceedings of 15<sup>th</sup> Intersociety Energy Conversion Engineering Conference*, AIAA Inc., Paper No. 809203, 1032 – 1043, 1980.
- Skrabek, E. A. and Trimmer, D. S., "Properties of the General TAGS System," *CRC Handbook of Thermoelectrics*, D.M. Rowe, ed., CRC Press, Boca Raton, 26 7-275, 1994.
- Swanson, B. W, Somers, E. V, and Heikes, R. R., "Optimization of a Sandwiched Thermoelectric Device", *J. Heat Transfer*, 77-82, 1961.
- Thieme, L., Schreiber, J., and Mason, L., "Stirling Technology Development at NASA GRC," in *Proceedings of Space Technology and Applications International Forum (STAIF-02)*, edited by M. S. El-Genk, AIP Conference Proceedings **608**, American Institute of Physics, Melville, NY, 872-879, 2002.
- Thieme, L. G. and Schreiber, J.G., "Advanced Technology Development for Stirling Converters," *Proceedings of Space Technology and Applications International Forum (STAIF-04)*, edited by M. S. El-Genk, American Institute of Physics, NY, 2004.